Experimental and Analytical Investigation of Axisymmetric Supersonic Cruise Nozzle Geometry at Mach Numbers From 0.60 to 1.30

George T. Carson, Jr.,
and Edwin E. Lee, Jr.

NASA

Experimental and Analytical Investigation of Axisymmetric Supersonic Cruise Nozzle Geometry at Mach Numbers From 0.60 to 1.30

George T. Carson, Jr.,
and Edwin E. Lee, Jr.
Langley Research Center
Hampton, Virginia

SUMMARY

An experimental investigation has been conducted which provides quantitative pressure and force data for five axisymmetric boattail nozzle configurations. These configurations simulate the variable-geometry feature of a single nozzle design operating over a range of engine operating conditions. This investigation was performed at an angle of attack of 0° in the Langley 16-Foot Transonic Tunnel at Mach numbers from 0.60 to 1.30. The experimental data and theoretical predictions, provided by computational fluid-dynamics programs, were compared and found to be in generally good agreement.

INTRODUCTION

A supersonic cruise aircraft must be capable of operation over a wide altitude-velocity flight envelope, which includes such diversities as subsonic take-off and landing, subsonic cruise, climb and loiter, and supersonic cruise. In addition, maneuver requirements may be added for military aircraft. Obviously, current engine concepts cannot be optimized over such a broad range of requirements. One proposed solution for these diverse requirements is the variable-cycle engine (VCE) which incorporates a variable-engine geometry and combustion arrangement in order to operate as a turbofan, an afterburning turbojet, a duct-burning turbofan, or an intermediate hybrid combination as required by any particular mission segment. Mission requirements, development concepts, and preliminary designs of the VCE may be found in references 1 to 8.

The purpose of the current investigation was to provide quantitative pressure and force data for an axisymmetric variable-geometry nozzle which is applicable for use in the design of the engine for a supersonic cruise aircraft. This was accomplished by testing five nozzles in the Langley 16-Foot Transonic Tunnel, which represent the variable-geometry feature of a single, convergent-divergent nozzle design over a range of engine operating conditions. Tests were conducted at nozzle pressure ratios from jet off to about 10 at free-stream Mach numbers from 0.60 to 1.30. The experimental data were compared with theoretical predictions in order to help verify several existing computational fluid-dynamics programs.

SYMBOLS

A_c increment of model cross-sectional area at metric break station 67.31 cm, m^2

A_e nozzle exit area, m^2

A_m maximum cross-sectional area of model, 182.415 cm^2

A_t nozzle geometric throat area, m^2

A_w surface wetted area, m^2

A_β increment of axially projected boattail area, m^2

$C_{D,f}$ boattail friction-drag coefficient (see section entitled "Data Reduction")

$C_{D,\beta}$ boattail pressure-drag coefficient (see section entitled "Data Reduction")

$C_{F,i}$ aerodynamic ideal thrust coefficient, $F_i/q_\infty A_m$

$C_{p,\beta}$ boattail pressure coefficient, $\dfrac{p_\beta - p_\infty}{q_\infty}$

$D_{f,cyl}$ friction drag on cylindrical portion of model between stations 67.31 cm and 137.16 cm, N

D_n nozzle total drag, N

d_e nozzle-exit diameter, cm

d_m model maximum diameter, 15.240 cm

d_t nozzle geometric throat diameter, cm

F thrust, N

$F_{A,mom}$ axial-momentum tare force, N

F_{bal} axial force measured by balance, positive forward, N

F_i ideal isentropic gross thrust, N

F_j gross thrust, $\dot{m}V_e + (p_e - p_\infty)A_e$, N

ι axial length of boattail, cm

ι_C axial length of nozzle convergent section, cm

ι_D axial length of nozzle divergent section, cm

M_∞ free-stream Mach number

$\dot{m}$ nozzle measured mass-flow rate, kg/sec

$\dot{m}_i$ nozzle ideal mass-flow rate, kg/sec

N_{Re} Reynolds number

p local static pressure, Pa

p_c local static pressure in the metric break, Pa

p_e average static pressure in the nozzle-exit plane, Pa

$p_{t,j}$ jet total pressure, Pa

$(p_{t,j}/p_\infty)_{des}$ design nozzle pressure ratio for ideally expanded exhaust flow

p_β local static pressure on the boattail, Pa

p_∞ free-stream static pressure, Pa

q_∞ free-stream dynamic pressure, Pa

R gas constant for air, 287.3 J/kg-K

r local radial distance from model center line, cm

r_m model maximum radius, 7.62 cm

$T_{t,j}$ jet total temperature, K

V_e average axial velocity in nozzle-exit plane, m/sec

x axial coordinate with origin one model diameter upstream of the nozzle exit (positive downstream), cm

β nozzle boattail angle, deg

γ ratio of specific heats, 1.3997 for air

δ nozzle divergence angle (downstream of throat), deg

θ nozzle convergence angle (upstream of throat), deg

Abbreviations:

A/B   afterburning

J/O   jet-off condition

APPARATUS AND PROCEDURE

Wind Tunnel

The experimental investigation was conducted in the Langley 16-Foot Transonic Tunnel. This facility is a single-return, continuous-flow, exchange-air-cooled, atmospheric wind tunnel with an octagonal slotted-throat test section. It has a continuously variable Mach number range from 0.20 to 1.30. A detailed description of this wind tunnel is given in reference 9.

Models

A set of five nozzle models was used to simulate the range of geometric settings of a variable-geometry axisymmetric nozzle applicable for supersonic cruise aircraft. A photograph of nozzle configuration 5 installed in the test section of the Langley 16-Foot Transonic Tunnel is shown in figure 1. Figure 2 depicts the general arrangement of the isolated nacelle model and support system. The five

nozzle configurations tested are shown in the photograph in figure 3. The simulated flight segment, simulated power setting, design nozzle pressure ratio, and design dimensions are presented in figure 4.

Jet-Exhaust Simulation

For jet-exhaust simulation, an external high-pressure air system provided a continuous flow of clean, dry air at a maximum pressure of 724 kPa and a controlled temperature of nominally 300 K ahead of the nozzle throat. As shown in figure 2, this high-pressure air was brought through the support sting and strut into a high-pressure plenum and was then introduced, through eight sonic nozzles, radially into the metric portion of the model to eliminate incoming axial momentum. Two flexible metal bellows provided an air seal between the metric and nonmetric portions of the nacelle. Finally, the air traveled through flow-smoothing screens into a stagnation chamber and expanded through the nozzle configuration being tested.

Instrumentation

Metric model forces and moments (excluding rolling moment) were measured by a five-component strain-gage balance. Jet total pressure and total temperature were measured by probes mounted in the metric tailpipe as shown in figure 2. Also, there was a row of internal static-pressure orifices from the nozzle entrance to the exit plane, and there was a row of external static-pressure orifices starting just forward of the nozzle boattail to the exit plane. The locations of the internal and external pressure orifices are given in table I. The pressure and temperature of the internal airflow were also measured in the high-pressure plenum located in the model forebody. (See fig. 2.) Static pressures in the gap at the metric break (station 67.31 cm) were obtained from 10 orifices distributed over the model cross-sectional area.

Tests

In accordance with the criteria of references 10 and 11, a boundary-layer transition strip, 0.25 cm wide consisting of No. 100 silicon carbide grit sparsely distributed in a lacquer film, was applied 2.54 cm downstream of the nose. Angle of attack was held at zero for all tests. Each nozzle configuration was tested at Mach numbers of 0.60, 0.80, 0.90, 0.94, 1.20, and nominally 1.30. The average Reynolds number per meter varied from 10.43×10^6 at a Mach number of 0.60 to 13.20×10^6 at a Mach number of 1.30. Nozzle pressure ratio was varied from jet off to approximately 10 depending on the free-stream Mach number.

Data Reduction

All data for both the model and wind-tunnel facility were recorded simultaneously on magnetic tape. The recorded data were used to compute standard force and pressure coefficients. All force coefficients in this report are referenced to the model maximum cross-sectional area.

Nozzle boattail pressure drag was obtained during this test from pressures measured along the top of the boattail (see table I) by assigning an incremental, axially projected area to each orifice and using the stepwise summation equation

$$C_{D,\beta} = \sum_{k=1}^{n} \frac{P_\infty - P_{\beta,k}}{q_\infty} \frac{A_{\beta,k}}{A_m} \tag{1}$$

where n is the number of orifices in the external row. To check these results, a number of continuous distributions of $C_{p,\beta}$ with $(r/r_m)^2$ were manually integrated by planimeter and gave essentially the same drag values as equation (1). Pressure forces on the small base at the nozzle exit are considered negligible and are not included in the boattail drag computation.

Aerodynamic skin-friction drag coefficients were computed from the flat-plate formula for turbulent, compressible boundary layer given in reference 12.

$$C_{D,f} = \left[\frac{0.472}{\left(1 + 0.2M_\infty^2\right)^{0.467} (\log_{10} N_{Re})^{2.58}} \right] \frac{A_w}{A_m} \tag{2}$$

At each test point, $C_{D,f}$ was calculated for Reynolds number N_{Re} and wetted areas A_w corresponding to three different characteristic lengths on the model (fig. 2): (1) nose to exit, (2) nose to the upstream end of the boattail at station 137.16 cm, and (3) nose to metric-break station 67.31 cm. The difference between calculations (1) and (2) provided the estimated skin-friction drag of the boattails; and the difference between calculations (2) and (3) was used to obtain the friction drag force on the cylindrical part of the metric afterbody $D_{f,cyl}$. As shown later, $D_{f,cyl}$ was used to correct the balance data.

Actual mass-flow rates used to compute discharge coefficients $\dot{m}/\dot{m}_i$ and ideal thrust for the test nozzles were measured by the system of eight radial nozzles supplying air to the metric afterbody. This required a pretest calibration of the internal-flow system which will be discussed subsequently. The ideal mass-flow rates for the test configurations were computed from stagnation pressure and temperatures measured in the tailpipe by using the choked-flow equation

$$\dot{m}_i = P_{t,j} A_t \sqrt{\frac{\gamma}{RT_{t,j}} \left(\frac{2}{\gamma + 1}\right)^{\frac{\gamma+1}{\gamma-1}}} \tag{3}$$

Ideal thrust, defined as the product of measured mass flow and the ideal isentropic velocity, was obtained from the relation

$$F_i = \dot{m} \sqrt{\frac{2\gamma}{\gamma - 1} RT_{t,j} \left[1 - \left(\frac{P_\infty}{P_{t,j}}\right)^{\frac{\gamma-1}{\gamma}} \right]} \tag{4}$$

Since the model strain-gage balance (fig. 2) measures the sum of pressure and viscous forces on the entire metric afterbody (model portions aft of station 67.31 cm), a number of corrections must be applied to the raw-balance data in order to isolate the sum of external and internal forces on the nozzle alone. Nozzle gross thrust-minus-drag performance was computed from the relationship

$$F_j - D_n = F_{bal} + \sum_{k=1}^{10} (p_{c,k} - p_\infty)A_{c,k} + D_{f,cyl} - F_{A,mom} \tag{5}$$

In equation (5) the term F_{bal} represents the raw-balance output corrected for interactions and model weight tares. The pressure-area term corrects for the force on the front face of the metric afterbody caused by differences between the cavity pressure p_c in the metric break and free-stream pressure p_∞. Even though experience with this model has shown cavity pressures to be extremely uniform, 10 orifices were used in these tests to determine this balance-correction term. As indicated previously, the term $D_{f,cyl}$ is the friction drag on the cylindrical section of the metric afterbody, which must be restored to the balance reading since this force is not associated with the nozzle. The term $F_{A,mom}$ corrects for axial momentum and bellows tare forces caused by the high-pressure air flowing from the nonmetric high-pressure plenum into the metric tailpipe through the eight small injection nozzles. (See fig. 2.) Although the air is injected radially and the flexible seals (metal bellows) are placed in tandem in an effort to eliminate such tares, small forces do arise in practice and must be taken into account. In the present investigation these forces were generally less than 2 percent of ideal thrust.

Axial-momentum tares were evaluated by statically ($M_\infty = 0$) testing several "standard" exhaust nozzles over the range of supply pressures, mass-flow rates, and throat areas required by the five test nozzles. The "standard" nozzles were internally convergent, with a circular-arc longitudinal profile tangent to the axial direction at the exit, and had a profile arc radius equal to twice the exit diameter. (See ref. 13.) The correct values of F_j/F_i and $\dot{m}/\dot{m}_i$ as functions of nozzle pressure ratio have been well established for these "standard" nozzles from previous tests and were used to predict gross thrust for comparison with the balance measurements. Any force difference, or momentum tare, was computed from equation (5), which for static conditions became simply

$$F_{A,mom} = F_{bal} - F_j \tag{6}$$

Resulting tare forces were correlated as a function of pressure measured in the high-pressure plenum in the model nose, thus providing a calibration from which tares were computed for the test-nozzle data.

Internal-flow measurements taken during the aforementioned tare calibrations were also used to compute discharge coefficients for the system of eight radial nozzles supplying air to the tailpipe. The actual mass-flow rates were those measured by the "standard" nozzles installed at the rear of the model. Since the eight air-supply nozzles were choked at all test conditions, the ideal mass-flow rates were computed from equation (3), by using the total throat area, and from the high-pressure plenum measurements as stagnation conditions. Resulting discharge coefficients were then plotted against plenum pressure, thus providing a calibration

6

of the air-supply system as a sonic flow meter. This calibration, and measurements taken in the high-pressure plenum, were later used to measure airflow when investigating the five test nozzle configurations.

Following the aforementioned calibrations, the five test nozzles were investigated at static ($M_\infty = 0$) conditions, and equation (6) was used to compute gross thrust. Wind-on gross thrust was also computed by using the wind-tunnel data and combining results of equations (1), (2), (4), and (5) in the equation

$$\frac{F_j}{F_i} = \frac{F_j - D_n}{F_i} + \frac{C_{D,\beta} + C_{D,f}}{C_{F,i}} \tag{7}$$

where $C_{F,i}$ is the aerodynamic ideal thrust coefficient, $F_i/q_\infty A_m$.

PRESENTATION OF EXPERIMENTAL AND ANALYTICAL RESULTS

The data from the experimental tests are presented in figures 5 to 18. Measured pressure distributions are shown in figures 5 to 9. Various measured force parameters are presented in figures 10 to 18. Results from computational fluid-dynamics programs are compared with selected experimental data in figures 19 to 25. A data list of the figures is presented as follows:

DISCUSSION OF EXPERIMENTAL RESULTS

Pressure Measurements

The external and internal surface-pressure distributions are given for each of the five nozzle configurations in figures 5 to 9. The nozzle longitudinal cross-section contour has been included in each figure to show the starting point (station 137.16 cm) and angle of the boattail for the external pressure distributions and to show the throat location and divergence angle for the internal pressure distributions. The symbol J/O in the keys of figures 5 to 9 denotes the jet-off condition and pertains to external pressures only.

External pressure distributions.- Jet operation generally had a favorable effect on the external pressure coefficients for the nozzles with low expansion ratios $(A_e/A_t = 1.25$ to $1.50)$ and large boattail angles from $8°$ to $15°$ (configurations 1, 3, and 4). Results for these configurations at $M_\infty = 0.90$ and 0.94 (for example, see fig. 5(c)) also indicate a standing shock wave located between $x/d_m = 0.2$ and 0.3, depending on configuration, M_∞, and $p_{t,j}/p_\infty$. Increasing $p_{t,j}/p_\infty$ tends to push the shock wave upstream, and external-flow separation occurs downstream of the shock wave for these configurations. At supersonic speeds (see fig. 5(e)), a trailing-edge shock occurs on the nozzle near the exit. As $p_{t,j}/p_\infty$ is increased, the trailing-edge shock is pushed upstream and large jet interference effects are observed behind the shock. Jet operation had little or no effect on the forward portion of the boattail pressure distributions at supersonic speeds, because the downstream disturbances can only feed forward through the subsonic boundary layer.

Separation of the external flow is shown to be primarily dependent upon boattail angle, because the data for configurations 2 and 5 with $\beta < 4°$ showed no evidence of shock formation or flow separation at any test condition. With increasing $p_{t,j}/p_\infty$, the boattail surface pressures decrease generally, indicating unfavorable jet effects. This is attributed to strong turbulent mixing and entrainment in the vicinity of the exit resulting from overexpansion and separation of the jet flow internally. Jet-interference effects extended well forward on the boattails of configurations 2 and 5 at subsonic speeds, but they were confined to the last pressure orifice just ahead of the exit at $M_\infty = 1.20$ and 1.28. Thus, the expansion occurring along the rear of the boattail at subsonic speeds gradually concentrates into an expansion fan centered on the nozzle-exit lip at supersonic Mach numbers.

Internal pressure distributions.- The ratio of static pressure to total pressure measured along the inside surface of the nozzles is shown at the bottom of

figures 5 to 9. Corresponding values for uniform, one-dimensional flow were computed from the the gas tables of reference 14 for the internal local-to-sonic area ratios of configuration 1. These results are compared with the experimental data in figure 5(a) and show that the axisymmetric flow overexpands noticeably at the throat $(x/d_m = 0.2)$. This is generally characteristic of nozzles with relatively steep convergent sections and "sharp" throats (small profile radius). Previous analytical studies, such as reference 15, have shown that the flow tends to "overturn" when passing around the throat profile. Therefore, the local flow angles relative to the nozzle axis exceed the wall divergence angle in the region behind the throat near the wall. Compressive turning is then required to match flow and wall angles, thus resulting in the positive pressure gradient behind the throat evident in much of the experimental data. Compression waves from this region coalesce in the vicinity of the nozzle axis and tend to form an internal shock surface that either intersects the wall further downstream or passes through the exit opening, depending on nozzle geometry. Evidence of the disturbance reaching the wall can be seen in figure 5 at $x/d_m = 0.7$ and in figure 7 at $x/d_m = 0.85$ (configurations 1 and 3, respectively). Notice that the small pressure rise at each of these locations appears only when the internal flow is locally attached; it is not, therefore, related to separation from overexpansion.

As the divergence angle increases, thereby increasing the flow area more rapidly behind the throat, the walls are better able to accommodate the "overturning" of the flow. The wall pressure gradient leaving the throat decreases correspondingly, and the tendency of this region to form internal shocks disappears. (For example, compare figs. 5 and 6.)

The internal pressure distributions show shock-induced flow in the divergent section of the nozzle for nozzle pressure ratios significantly less than the design value. Increasing the divergence angle δ of the nozzle not only increases the axially projected area of the divergent section but also moves the separation location forward at a given M_∞ and nozzle pressure ratio. The latter was particularly noticeable as δ varied from 4.8° to 13.2° (configurations 4, 5, and 2), and this effect may be seen by comparing corresponding parts of figures 8, 9, and 6, in that order. Thus, increased divergence and extensive separation combine to expose increasing amounts of internal surface area to local pressures surrounding the exit. This, in turn, causes the external flow to have stronger effects on the pressure forces generated by the divergent section.

The largest effects of M_∞ on internal pressures occurred with configurations 2 and 5, which were the most extensively separated nozzles. Figures 6 and 9 show that increasing M_∞ at fixed nozzle pressure ratio reduced the pressure level in the separated region and tended to move the separation location rearward. Also, the most noticeable pressure reduction in the separated region occurred as M_∞ increased from 0.94 to 1.20 and the external flow began to undergo supersonic expansion at the exit lip. Consequently, increasing M_∞ can be expected to increase the overexpansion and drag associated with the divergent section at low nozzle pressure ratios.

Obviously, as nozzle pressure ratio is increased by increasing the jet stagnation pressure $p_{t,j}$, the separation moves to the exit and disappears. Once the exit flow is fully supersonic, the internal pressure distribution becomes independent of external conditions. For the present configurations, the minimum nozzle pressure ratio required to eliminate separation ranged from approximately 3 to 7 for corresponding design values of 4.25 to 21.23 and for expansion ratios of 1.25 to 3.00, respectively.

External Performance

The variation of jet-off, boattail pressure-drag coefficient with free-stream Mach number is shown in figure 10. Jet-off boattail pressure drag generally increases with increasing nozzle boattail angle. As the Mach number approached unity, the steepest drag rise occurred for nozzles with $\beta = 8°$ to $15°$, starting at $M_\infty \approx 0.80$. As might be expected, the shallow boattails of configurations 2 and 5 exhibit a much smaller drag rise, which started at $M_\infty \approx 0.90$ or slightly greater. In the supersonic-speed range, boattail pressure-drag coefficient is almost directly proportional to nozzle boattail angle.

Figure 11 presents the influence of nozzle pressure ratio on boattail pressure-drag coefficient for all configurations and test Mach numbers. In general, these curves are shaped by two opposing effects: the growth in jet diameter, or pluming effect, which pressurizes the boattail surface and thus reduces drag; and jet entrainment, which tends to accelerate the flow on the boattail, thereby increasing the drag. Therefore, where the slopes of the curves are negative, the pluming effect predominates, and where positive, the influence of jet entrainment predominates. On any given curve, a drag level less than the initial jet-off value ($p_{t,j}/p_\infty \approx 1$) indicates a favorable jet effect. Furthermore, all subsequent comments regarding jet effects on boattail drag refer to the portion of the drag curves between $p_{t,j}/p_\infty = 3$ and the maximum test value, since this is the range of practical interest for the Mach numbers of this test.

Jet operation had a favorable effect on the boattail drag of nozzle configurations 1, 3, and 4 at all test Mach numbers. At subsonic conditions the jet effects on drag are caused by modest increases in pressure which extend over all or most of the boattail length at a given nozzle pressure ratio. Among configurations 1, 3, and 4, the jet effects at $M_\infty = 0.60$ and 0.80 are seen to increase with increasing boattail angle (projected area) such that the drag levels are nearly equal for $\beta = 8°$ to $15°$. As M_∞ becomes supersonic, the influence of the jet on boattail pressures becomes limited to the rear half or less of the boattail length. However, as the nozzle pressure ratio increases, the pluming jet pushes the trailing shock forward, thus substantially increasing the pressure and the area affected behind the shock. Consequently, the effect of the jet on the drag coefficients of configurations 1, 3, and 4 is still strongly favorable at supersonic speeds as reflected in figure 11(c).

The shallow boattails of configurations 2 and 5 exhibit much smaller variations in pressure-drag coefficients with nozzle pressure ratio than the other configurations. At subsonic speeds, jet effects on the drag of configurations 2 and 5 are unfavorable. The increase in boattail drag with jet operation is attributed to the dominance of jet entrainment when the nozzles are operating highly overexpanded ($p_{t,j}/p_\infty \ll$ Design value) and, therefore, produce little, if any, beneficial pluming effect. At supersonic speeds the boattail pressure data for configurations 2 and 5 showed no shock formation or separation, and jet effects were confined to a very small area just ahead of the exit. Figure 11(c) confirms that jet effects on drag at $M_\infty = 1.20$ and 1.28 are negligible.

Internal Performance

Nozzle internal thrust performance F_j/F_i was determined by equation (7). Thrust was obtained by combining the boattail pressure drag of figure 11 and boattail skin-friction drag shown in figure 12 with the thrust-minus-drag measurements

10

from the model balance. The resulting variations of thrust ratio with nozzle pressure ratio are indicated in figure 13, and the discharge coefficients are shown in figure 14. The internal performance of the test configurations may be summarized as follows:

(1) Nozzle configurations 1, 3, 4, and 5 achieved an average peak thrust performance of $F_j/F_i \approx 0.99$ at values of nozzle pressure ratio at or near design value (optimum expansion).

(2) Experimental nozzle pressure ratios for nozzle configuration 2 were substantially lower than the design value; therefore, this configuration suffered overexpansion losses throughout the range of nozzle pressure ratios shown. However, it is noted that $F_j/F_i \approx 0.95$ at 50 percent of design nozzle pressure ratio, which is characteristic of all configurations when free of external-flow effects. (See configurations 1, 3, 4, and 5 at $M_\infty = 0$.) Therefore, the peak performance of configuration 2 would also be expected to reach $F_j/F_i \approx 0.99$ at the design point.

(3) When the internal flow was considerably overexpanded and separated, the presence of external flow tended to reduce the thrust performance of the nozzles relative to the wind-off case ($M_\infty = 0$), particularly at supersonic speeds. At a given nozzle pressure ratio, this additional overexpansion loss increased with increasing divergence angle and free-stream Mach number as indicated by the internal pressure data discussed previously.

(4) At nozzle pressure ratios high enough to eliminate internal separation, the thrust ratios for all Mach numbers converged to one curve. This indicated fully supersonic exit flow with internal performance independent of external conditions. Reference 16 shows similar effects of internal-flow separation for another group of axisymmetric, convergent-divergent nozzles.

(5) Figure 14 shows that the discharge coefficients of all nozzles are essentially independent of nozzle pressure ratio (and throat Reynolds number) when operating choked. Values of $\dot{m}/\dot{m}_i$ ranged from 0.964 (configuration 1) to 0.976 (configuration 5), the average level being rather typical of nozzles with relatively "sharp" throats. The improvement in discharge coefficient between configurations 1 to 5 is attributed to more uniform flow entering the throat as the convergence angle decreased and also to the boundary layer thinning as the pressure gradient behind the throat decreased with increasing divergence angle.

Overall Performance

The ratio of nozzle thrust minus drag to ideal thrust plotted against nozzle pressure ratio for all configurations and test Mach numbers is shown in figure 15. The shape of these curves is determined primarily by thrust characteristics, and the maximum overall force ratio approaches the internal performance F_j/F_i as F_i becomes large relative to drag at high pressure ratios. At subsonic speeds, the relative levels of the data reflect the nearly equal drag characteristics of configurations 1, 3, and 4 (fig. 11(a)) as well as the large overexpansion losses of configurations 2 and 5 (fig. 13), both cited previously. As the free stream becomes supersonic, higher drag losses and the inverse variation of overall performance with boattail angle become increasingly evident.

Aerodynamic ideal-thrust coefficient of all nozzle configurations tested is plotted in figure 16 as a function of nozzle pressure ratio for the various test Mach

numbers. Since configurations 1 and 2 have identical throat areas and their static discharge coefficients are nearly the same (see fig. 14), their ideal thrust coefficients, within the graphical accuracy of figure 16, appear as one plot. (See fig. 16(a).) These graphs provide the means of converting aerodynamic coefficients based on $q_\infty A_m$ to propulsion-force ratios based on F_i. (That is, $F/q_\infty A_m C_{F,i} = F/F_i$.)

Figure 17 presents a representative schedule of nozzle pressure ratio with Mach number for a low bypass-ratio turbofan engine operating at maximum rotational speed (climb and acceleration conditions). This schedule was obtained from unpublished industry sources used in performance studies of advanced supersonic aircraft. Figure 18 shows the overall performance (fig. 16) for the nozzle configurations appropriate to the test speed range at typical operating pressure ratios and Mach numbers of the schedule (fig. 17). For convenient reference, the corresponding value of nozzle pressure ratio from the schedule is repeated with each Mach number at the bottom of figure 18. Also indicated are the optimum expansion ratios obtained from reference 14 for the schedule pressure ratios at each end of the subsonic and supersonic Mach number segments. The solid symbols denote internal performance for configuration 5 and show the rate at which the thrust optimizes for $A_e/A_t = 2.0$ as schedule conditions increase toward the design point ($p_{t,j}/p_\infty = 10.64$) which is reached near $M_\infty = 1.6$. (See fig. 17.) By using figure 18, the overall performance can be summarized for a variable-geometry nozzle operating at optimum expansion ($F_j/F_i = 0.99$) along the assumed flight schedule of figure 17.

At $M_\infty = 0.60$ to 0.80, configuration 1 is operating at optimum internal expansion ($F_j/F_i = 0.99$), which can be seen in figure 13 at schedule pressure ratios. If the exit areas of configurations 3, 4, and 5 were adjusted to provide the same internal conditions, it can be shown that the resulting boattail angles of all configurations then range from approximately 8° to 15°. It was shown previously (fig. 11(a)) that boattails in this angle range have nearly equal drag values at $M_\infty = 0.60$ and 0.80. Therefore, all optimized configurations would be expected to have the same performance loss due to boattail drag as that shown by the data for configuration 1. As a result, the overall force ratio for optimum expansion at all power settings is approximately 0.98 as shown for configuration 1 between $M_\infty = 0.60$ and 0.80.

At Mach numbers between 0.80 and 0.94, test configurations 1, 3, and 4 are all operating at or near optimum expansion. (See fig. 13.) Therefore, the experimental data curves show overall force ratios for this condition directly, as well as the performance loss from boattail drag alone as each configuration enters the drag rise. It can be shown from the nozzle geometry and drag data that optimizing the exit area of configuration 5 for this Mach number segment results in a boattail angle and overall performance very similar to that of configuration 4. The flagged symbol at $M_\infty = 0.90$ denotes a representative subsonic cruise point at reduced power (i.e., not associated with the schedule). The cruise pressure ratio assumed was $p_{t,j}/p_\infty = 4$, which is an average of values generally associated with advanced fighters and transports. At $M_\infty = 0.90$, overall force ratios are shown to range approximately from 0.95 at reduced-power cruise to 0.975 for afterburning conditions.

At supersonic speeds, the overall performance for optimum expansion was estimated from the test data. For each Mach number and throat area, boattail angles were determined from the nozzle geometry for the optimum-expansion ratios of 1.58 and 1.69 required by the schedule. From cross plots of drag against boattail angle, the values of boattail drag for optimum-expansion settings were selected. These values of boattail drag were converted to D_n/F_i by dividing them by the appropriate

12

values of $C_{F,i}$ (fig. 16) and then subtracting the result from $F_j/F_i = 0.99$. The results, labeled "Optimum expansion" in figure 18, are identified by line code with the corresponding throat area of the test configurations with fixed-expansion ratio.

For $A_t/A_m = 0.42$, the experimentally measured overall performance for $A_e/A_t = 2.00$ is seen to equal that estimated for optimum-expansion ratios of the schedule. This indicates that the rates of change of thrust and drag with expansion ratio have equalized at these speeds. Consequently, if the exit area is increased somewhat beyond the optimum value, the resulting internal overexpansion loss is offset by an equal reduction in boattail drag. Moreover, the calculations verify that this is true for all three throat areas. At $M_\infty = 1.3$ it can be seen that the overall force ratio for optimally expanded settings from maximum dry power to maximum afterburning should range from 0.96 to 0.98, respectively. Based on the experimental data at $M_\infty = 1.3$, configuration 5 should provide an overall force ratio of approximately 0.985 when the schedule and design pressure ratios match in the vicinity of $M_\infty = 1.6$. (See fig. 17.) This is verified in reference 16 by performance data for similar convergent-divergent nozzles tested at higher supersonic Mach numbers. In conclusion, figure 18 shows the general importance of maintaining optimum expansion in flight and the high performance that results over a wide range of power settings.

<center>ANALYTICAL INVESTIGATION</center>

The following computer programs were used to provide theoretical comparisons with the experimental data:

DONBOL (Douglas-Neumann/Boundary Layer): This program, described in reference 17, was used to calculate external surface-pressure distributions over the axisymmetric boattail nozzles in the subsonic-speed regime ($M_\infty = 0.60$ and 0.80). The DONBOL program couples a Neumann solution for inviscid external flow, a modified Reshotko-Tucker integral boundary-layer technique, the control-volume method of Presz for calculating flow in the separated region, and an inviscid one-dimensional solution for the jet-exhaust flow. The viscous and inviscid flows are solved iteratively until convergence is obtained. This method is limited to subsonic free-stream Mach numbers below that for which the flow over the body of revolution becomes sonic; also, this method does not include the effects of jet entrainment. Specifying the separation location is not necessary; however, the start and end of the region searched for separation must be specified.

MOC (Method of Characteristics): This program was used to calculate the afterbody surface-pressure distribution in the supersonic-speed regime ($M_\infty = 1.2$ and 1.28). The MOC program performs an axisymmetric method-of-characteristics solution for supersonic flow over boattailed afterbodies and is restricted to axisymmetric, inviscid, irrotational flow. Since a description of this program, which was developed by Lawrence E. Putnam, Bobby L. Berrier, and Richard G. Wilmoth of the Langley Research Center, has not been published, reference 18 is given as a description of the theoretical development of the axisymmetric method of characteristics.

NAP (Nozzle Analysis Program): This program, described in reference 19, was used to calculate the nozzle internal pressure distribution and gross internal thrust. The NAP is capable of calculating time-dependent, perfect gas, inviscid, steady, and unsteady flow in two-dimensional and axisymmetric nozzles by using the nonconservative form of the two-dimensional equations of motion for a geometric computational grid which spans the flow area. Interior mesh points are calculated by using a MacCormack finite-difference method (a two-step predictor-corrector method

described in ref. 20); a characteristics method is used to compute the boundary mesh points; and shock waves are modeled by using a shock-smearing technique which incorporates an explicit artificial viscosity term with numerical smoothing described in reference 21. Gross thrust is obtained by integrating the momentum flux and difference between exit and ambient pressures over the exit area. The NAP becomes increasingly inaccurate below design nozzle pressure ratio since limitations in the code prevent the flow velocity from returning to subsonic levels once it has become supersonic. This investigation is an example of NAP being applied to the analysis of an axisymmetric converging-diverging nozzle. Reference 22 gives an example of NAP being applied to the analysis of a nonaxisymmetric converging-diverging wedge nozzle.

DISCUSSION OF ANALYTICAL RESULTS

External Pressure Distribution

A comparison of experimentally and analytically determined external pressure distributions is given in figures 19 to 23 which present data for nozzle configurations 1 to 5, respectively. For part (a) of each figure which presents free-stream Mach numbers of 0.60 and 0.80, the theoretical prediction was computed by the DONBOL program of reference 17. Reasonable agreement with the experimental data trends was obtained for nozzle configurations with the larger boattail angles ($\beta > 8°$). The DONBOL program generally underpredicted the strength of the nozzle shoulder expansion and the compression near the nozzle exit. Poor agreement between theory and experiment was obtained for the two nozzles with very small boattail angles ($\beta < 4°$). This discrepancy between the predictions of the DONBOL code and experiment for the small boattail-angle nozzles (configurations 2 and 5) is associated primarily with the analytical modeling of the jet-exhaust plume. The simple one-dimensional-solution technique for the jet-exhaust plume used in the DONBOL code is not adequate for the highly overexpanded nozzle cases of the present investigation. Also, the neglect of jet-entrainment effects by the DONBOL code is a factor in the observed discrepancies especially near the nozzle exit. Part (b) of figures 19 to 23 presents a comparison of theory and experiment for free-stream Mach numbers of 1.20 and 1.28 for configurations 1 to 3 (1.20 and 1.27 for configurations 4 and 5).

Good agreement was obtained for configurations with small boattail angles (configurations 2 and 5) except near the nozzle exit. For configurations with large boattail angles (configurations 1, 3, and 4), good agreement of theory and experiment was obtained until a shock wave and/or separated region was encountered on the nozzle external surface. Large discrepancies were noted in these regions. It is noted that the MOC computer code utilized is an isentropic, inviscid method-of-characteristics program. Therefore, although this program can reasonably predict the surface-pressure distribution of configurations with small boattail angles, it cannot predict surface pressures behind shock waves or in separated-flow regions associated with nozzle configurations having large boattail angles.

Internal Pressure Distribution

A comparison of experimentally and analytically determined internal pressure distribution for each nozzle configuration is given in figure 24. The experimental data shown were all taken at a free-stream Mach number of 0.60. However, internal pressure distributions are independent of free-stream Mach number at and above design nozzle pressure ratio. Below design nozzle pressure ratio, the experimental data may show effects of flow separation which cannot be predicted by the inviscid NAP of

reference 19. Good agreement is shown in figure 24 between experiment and theory, except in the converging section just upstream of the throat of each nozzle. In this section of the nozzle, the analytical predictions are consistently low. For configuration 2 which has a design nozzle pressure ratio of 21.23, the agreement between experiment and theory was remarkably better than expected, since the experimental nozzle pressure ratio of 6.97 was significantly lower than the design value. However, the nozzle was flowing full up to approximately $x/d_m = 0.95$, thereby making the effects of separation minimal.

Static Thrust Coefficient

Figure 25 shows a comparison of experimentally and analytically determined variation of static thrust coefficient with nozzle pressure ratio for each nozzle configuration. The solid line shown as theory represents the internal gross thrust computed by the NAP of reference 19. The dashed line depicted as ideal thrust was calculated by the equation for optimum thrust coefficient

$$\frac{F}{A_t P_{t,j}} = \left\{ \frac{2\gamma^2}{\gamma - 1} \left(\frac{2}{\gamma + 1}\right)^{\frac{\gamma+1}{\gamma-1}} \left[1 - \left(\frac{P_\infty}{P_{t,j}}\right)^{\frac{\gamma-1}{\gamma}} \right] \right\}^{1/2} \tag{8}$$

As expected, the experimental and theoretical values were less than the ideal value for all configurations. Excellent agreement between theory and experiment was obtained for nozzle configurations with low expansion ratios (configurations 1, 3, and 4). However, it is noted that for configurations 2 and 5 (high expansion ratios), the experimental values significantly exceeded the theoretical values at the lower nozzle pressure ratios tested. This may appear at first as a data anomaly when considering that the NAP does not consider viscous losses. The anomaly is best understood by considering that the maximum nozzle pressure ratio tested for these configurations is far below the design values of 21.23 and 10.69 for configurations 2 and 5, respectively.

Examination of the experimental internal pressure distribution for these two nozzle configurations (figs. 6 and 9 for configurations 2 and 5, respectively) readily shows the large amount of separation present. Large shock-induced separated-flow regions are indicated for these configurations at nozzle pressure ratios below 7.0 for configuration 2 and below 4.0 for configuration 5. Since the NAP is limited to inviscid flow, and flow velocities cannot return to subsonic levels once supersonic, NAP obviously cannot provide accurate results when large separated regions exist. However, the trends shown in figure 25 do indicate that NAP is capable of providing accurate results for these nozzle configurations at higher nozzle pressure ratios. Also, reasonable predictions far below design nozzle pressure ratio are possible. This justifies using the code over a wide range of nozzle pressure ratios during preliminary design and development of new nozzles.

CONCLUSIONS

An experimental investigation has been conducted which provides quantitative pressure and force data for five axisymmetric convergent-divergent nozzles with dif-

ferent internal and external geometry. These nozzles simulate the variable-geometry nozzle operating over a range of engine operating conditions. This investigation was conducted at an angle of attack of 0° in the Langley 16-Foot Transonic Tunnel at free-stream Mach numbers M_∞ from 0.60 to 1.30. Nozzle pressure ratio was varied from jet off to 10, depending on configuration and Mach number. The experimental data were also compared with computational theoretical predictions for internal pressure distribution, gross internal thrust, and external pressure distribution at subsonic and supersonic free-stream Mach numbers.

The results of this experimental and analytical investigation indicated the following conclusions:

1. Jet-off, boattail pressure-drag coefficient was generally proportional to the nozzle boattail angle.

2. The amount in external-flow separation on the nozzle generally increased with increasing boattail angle, free-stream Mach number, and nozzle pressure ratio.

3. Configurations which have very low boattail angles show only minor variation of pressure drag with nozzle pressure ratio, especially at supersonic speeds.

4. Separation of internal flow was directly proportional to divergence angle and inversely proportional to nozzle pressure ratio.

5. The ratio of thrust minus drag to ideal thrust for optimum expansion at $M_\infty = 0.90$ was 0.95 for subsonic cruise and 0.975 for afterburning throat settings. At $M_\infty = 1.3$, the overall force ratio for optimum expansion varied from 0.96 to 0.98 for throat areas from maximum dry power to maximum afterburning, respectively.

6. At subsonic speeds, theoretical external pressure distributions predicted by the DONBOL (Douglas-Neumann/Boundary Layer) program were in reasonable agreement with the experimental data for configurations which had boattail angles greater than 8° but were in poor agreement with experimental data for highly overexpanded nozzle configurations with boattail angles less than 4°.

7. At supersonic speeds, theoretical external pressure distributions predicted by the MOC (Method of Characteristics) program were in good agreement with the experimental data until a shock wave and/or separated region was encountered on the nozzle external surface.

8. Theoretical internal pressure distributions predicted by the NAP (Nozzle Analysis Program) were in good agreement with the experimental data except in the converging section (upstream of throat) of each nozzle. In this section of the nozzle, the analytical predictions are consistently low.

9. The theoretical static thrust coefficient, predicted by the NAP, was in excellent agreement with the experimental data except at nozzle pressure ratios which produce large internal-flow-separation regions. The nozzle pressure ratios which produce internal-flow separation were found to be well below the design nozzle pressure ratio.

Langley Research Center
National Aeronautics and Space Administration
Hampton, VA 23665
October 28, 1981

16

REFERENCES

1. Willis, Edward: Variable-Cycle Engines for Supersonic Cruise Aircraft. NASA
   TM X-73463, 1976.

2. Howlett, Robert A.: Variable Stream Control Engine Concept for Advanced
   Supersonic Aircraft - Features and Benefits. Proceedings of the SCAR
   Conference - Part 1, NASA CP-001, [1977], pp. 341-352.

3. Krebs, J. N.: Advanced Supersonic Technology Study - Engine Program Summary:
   Supersonic Propulsion - 1971 to 1976. Proceedings of the SCAR Conference -
   Part 1, NASA CP-001, [1977], pp. 353-370.

4. Powers, Albert G.; Whitlow, John B.; and Stitt, Leonard E.: Component Test
   Program for Variable-Cycle Engines. Proceedings of the SCAR Conference -
   Part 1, NASA CP-001, [1977], pp. 371-385.

5. Allan, R. D.; and Johnson, J. E.: Supersonic Cruise Research Propulsion System
   Studies - Slide Presentation. Supersonic Cruise Research '79 - Part 1,
   NASA CP-2108, 1980, pp. 339-345.

6. Vdoviak, J. W.; and Ebacher, J. A.: VCE Test Bed Engine for Supersonic Cruise
   Research. Supersonic Cruise Research '79 - Part 1, NASA CP-2108, 1980,
   pp. 347-356.

7. Hunt, Richard B.; and Howlett, Robert A.: Variable Stream Control Engine for
   Advanced Supersonic Aircraft Design Update. Supersonic Cruise Research
   '79 - Part 1, NASA CP-2108, 1980, pp. 357-370.

8. Westmoreland, John S.: Progress With Variable Cycle Engines. Supersonic Cruise
   Research '79 - Part 1, NASA CP-2108, 1980, pp. 371-390.

9. Corson, Blake W., Jr.; Runckel, Jack F.; and Igoe, William B.: Calibration of
   the Langley 16-Foot Transonic Tunnel With Test Section Air Removal. NASA
   TR R-423, 1974.

10. Braslow, Albert L.; and Knox, Eugene C.: Simplified Method for Determination
    of Critical Height of Distributed Roughness Particles for Boundary-Layer
    Transition at Mach Numbers From 0 to 5. NACA TN 4363, 1958.

11. Braslow, Albert L.; Hicks, Raymond M.; and Harris, Roy V., Jr.: Use of Grit-Type
    Boundary-Layer-Transition Trips on Wind-Tunnel Models. NASA TN D-3579, 1966.

12. Shapiro, Ascher H.: The Dynamics and Thermodynamics of Compressible Fluid
    Flow. Vol. II. Ronald Press Co., c.1954, p. 1110.

13. Stratford, B. S.: The Calculation of the Discharge Coefficient of Profiled
    Choked Nozzles and the Optimum Profile for Absolute Air Flow Measurement.
    J. R. Aeronaut. Soc., vol. 68, no. 640, Apr. 1964, pp. 237-245.

14. Ames Research Staff: Equations, Tables, and Charts for Compressible Flow. NACA
    Rep. 1135, 1953. (Supersedes NACA TN 1428.)

15. Migdal, D.; and Kosson, R.: Shock Predictions in Conical Nozzles. AIAA J.
    (Tech. Notes), vol. 3, no. 8, Aug. 1965, pp. 1554-1556.

16. Berrier, Bobby L.; and Re, Richard J.: Investigation of Convergent-Divergent Nozzles Applicable to Reduced-Power Supersonic Cruise Aircraft. NASA TP-1766, 1980.

17. Putnam, Lawrence E.: DONBOL: A Computer Program for Predicting Axisymmetric Nozzle Afterbody Pressure Distributions and Drag at Subsonic Speeds. NASA TM-78779, 1979.

18. Liepmann, H. W.; and Roshko, A.: Elements of Gasdynamics. John Wiley & Sons, Inc., c.1957.

19. Cline, Michael C.: NAP: A Computer Program for the Computation of Two-Dimensional, Time-Dependent, Inviscid Nozzle Flow. LA-5984 (Contract W-7405-ENG. 36), Los Alamos Sci. Lab., Univ. of California, Jan. 1977.

20. MacCormack, Robert W.: The Effect of Viscosity in Hypervelocity Impact Cratering. AIAA Paper No. 69-354, Apr.-May 1969.

21. Richtmyer, Robert D.; and Morton, K. W.: Difference Methods for Initial-Value Problems, Second ed. Interscience Publ., c.1967, Chapters 12 and 13.

22. Carson, George T., Jr.; and Mason, Mary L.: Experimental and Analtical Investigation of a Nonaxisymmetric Wedge Nozzle at Static Conditions. NASA TP-1188, 1978.

TABLE I.- NOZZLE PRESSURE-ORIFICE LOCATIONS[a]

Configuration 1		Configuration 2		Configuration 3		Configuration 4		Configuration 5	
External	Internal	External	Internal	External	Internal	External	Internal	External	Internal
x/d_m	x/d_m	x/d_m	x/d_m	x/d_m	x/d_m	x/d_m	x/d_m	x/d_m	x/d_m
-0.150	-0.100	-0.180	-0.313	-0.110	-0.210	-0.120	-0,270	-0.120	-0.270
-.050	.028	-.080	-.180	-.060	-.093	-.070	-.153	-.070	-.153
.000	.077	-.030	-.080	b-.010	.020	b-.020	-.063	b-.020	-.063
.050	.118	b.020	-.023	.040	.072	.030	.007	.030	-.005
.100	.160	.070	.052	.090	.122	.080	.062	.080	.045
.150	.187	.120	.095	.140	.155	.130	.112	.130	.095
.200	.200	.170	.128	.190	.188	.180	.145	.180	.128
.250	.232	.220	.162	.240	.195	.230	.178	.255	.162
.300	.273	.270	.195	.290	.220	.280	.200	.330	.195
.400	.357	.420	.210	.390	.253	.363	.208	.580	.213
.433	.398	.520	.220	.440	.287	.438	.242	.730	.240
.483	.448	.620	.242	.507	.322	.530	.275	.880	.273
.533	.500	.720	.275	.590	.388	.630	.342	.980	.340
.600	.548	.820	.360	.690	.422	.730	.375		.390
.667	.600	.920	.410	.790	.455	.830	.427		.442
.750	.658	.995	.460	.890	.505	.930	.477		.492
.833	.715		.510	.990	.605	.980	.527		.542
.900	.782		.562		.655		.577		.592
.980	.850		.613		.722		.643		.643
	.917		.680		.788		.712		.713
	.983		.748		.857		.778		.772
			.815		.923		.847		.840
			.883		.990		.913		.907
			.953				.980		.980
			1.000						

[a]Single external-orifice row is located along top center line of nozzle afterbody. Single internal-orifice row is located 45° clockwise from top of nozzle, looking upstream.
[b]Subtract these values from external and internal coordinates to locate orifice from start of boattail (station 137.16 cm).
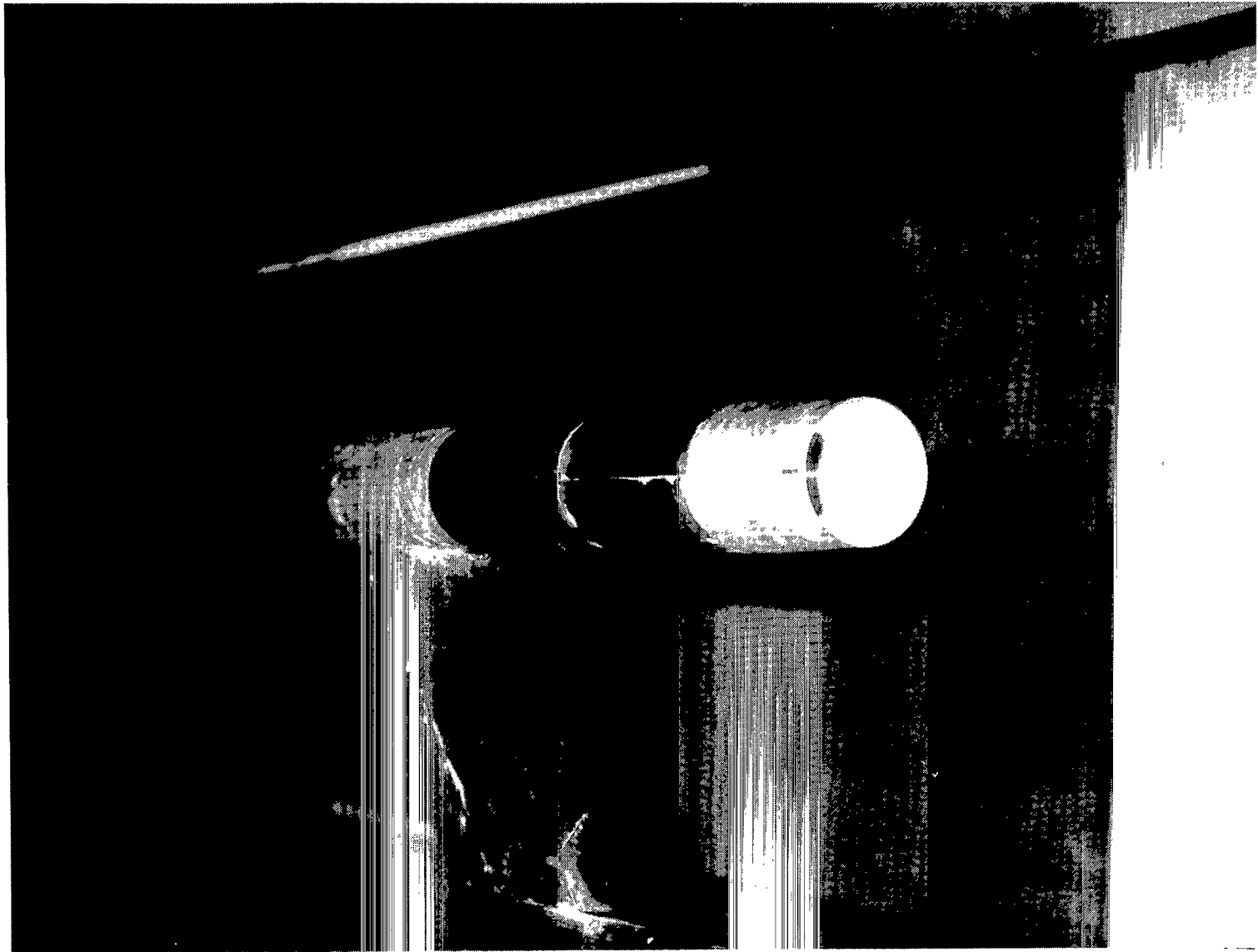
L-78-5575

Figure 1.- Photograph showing installation of nozzle configuration 5 in test section of
the Langley 16-Foot Transonic Tunnel.
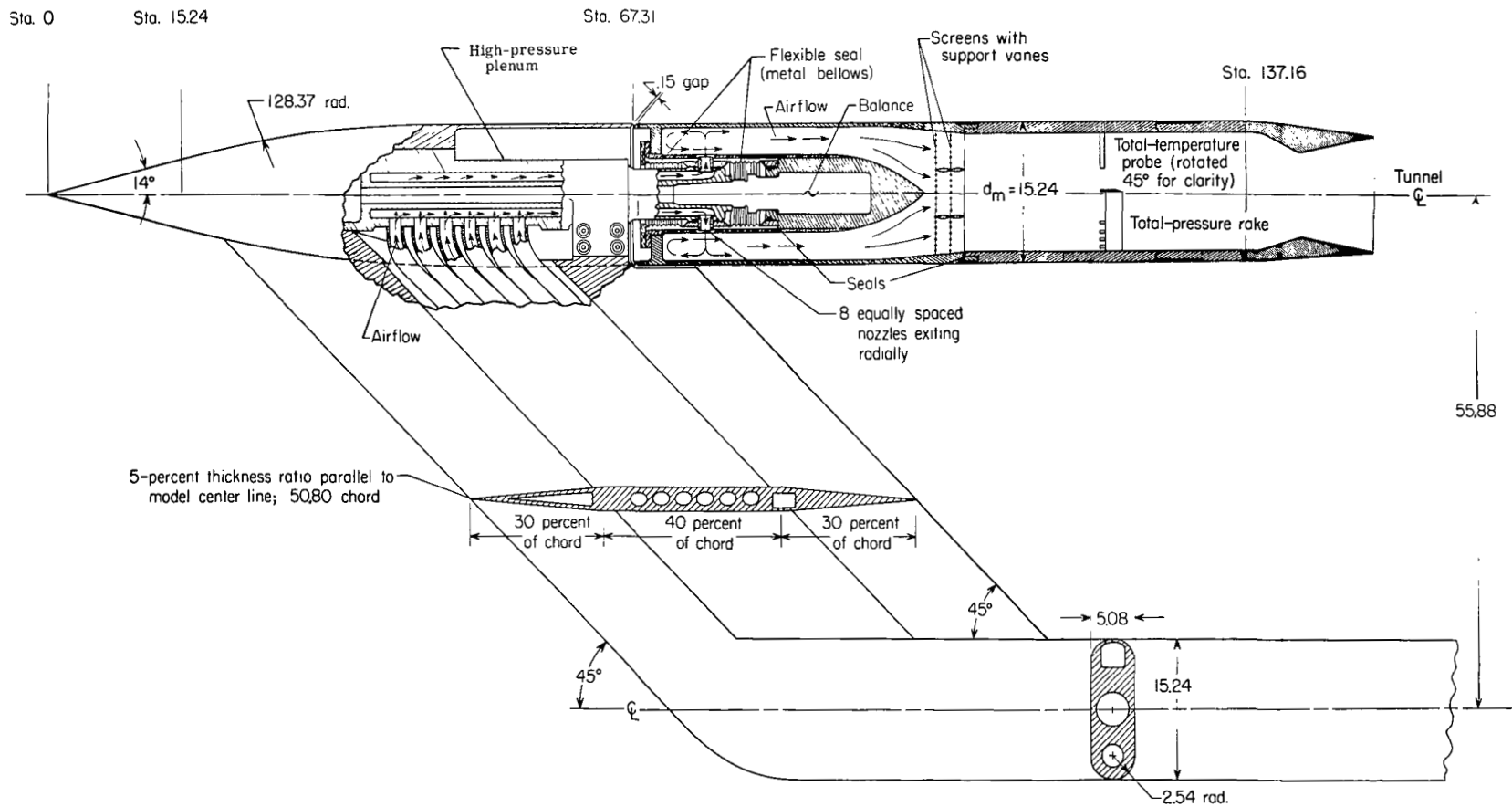
Figure 2.- General arrangement of the nacelle model and support system. All linear dimensions are in centimeters.
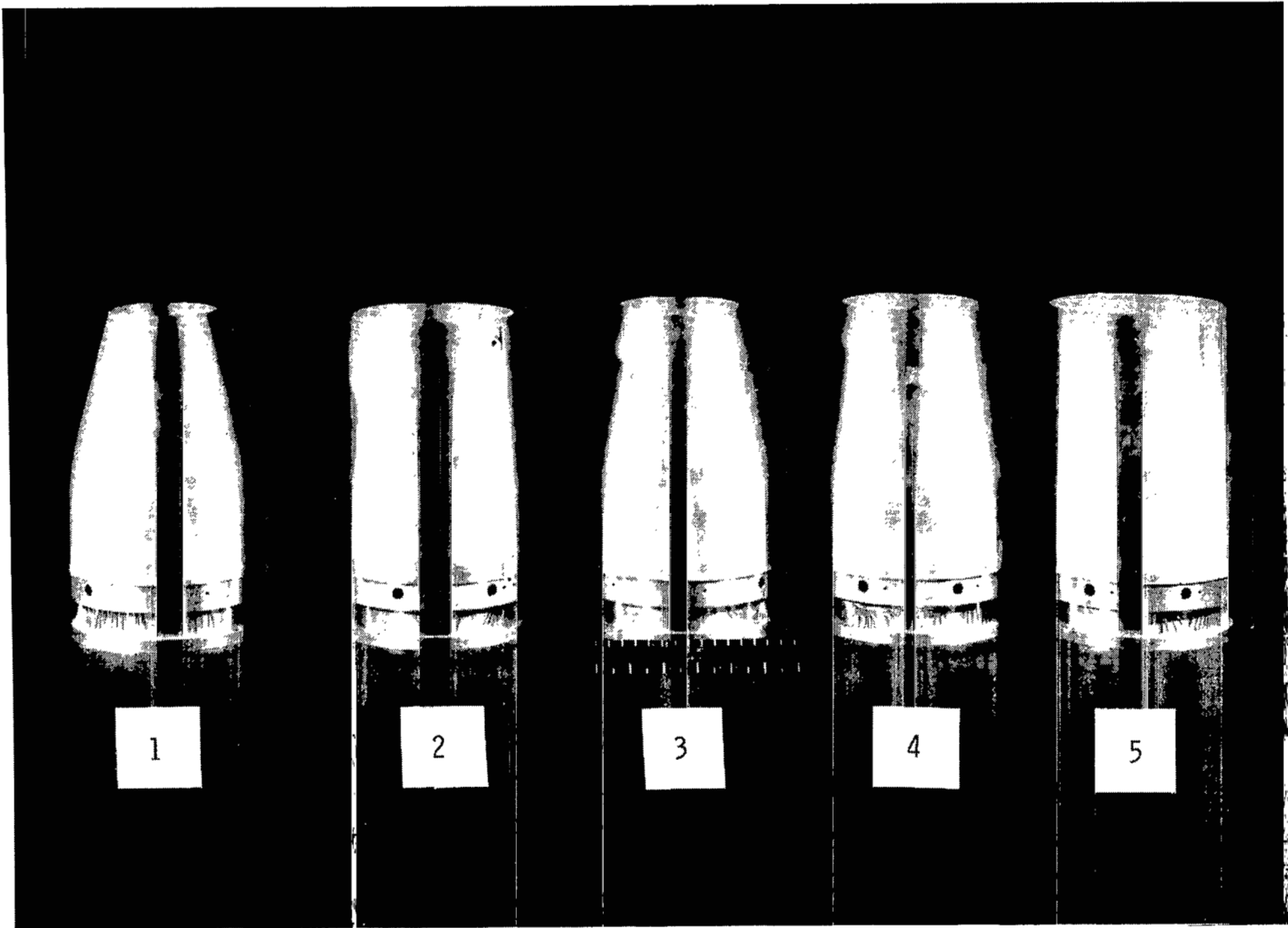
L-78-5750.1

Figure 3.- Photograph showing the five nozzle configurations tested.
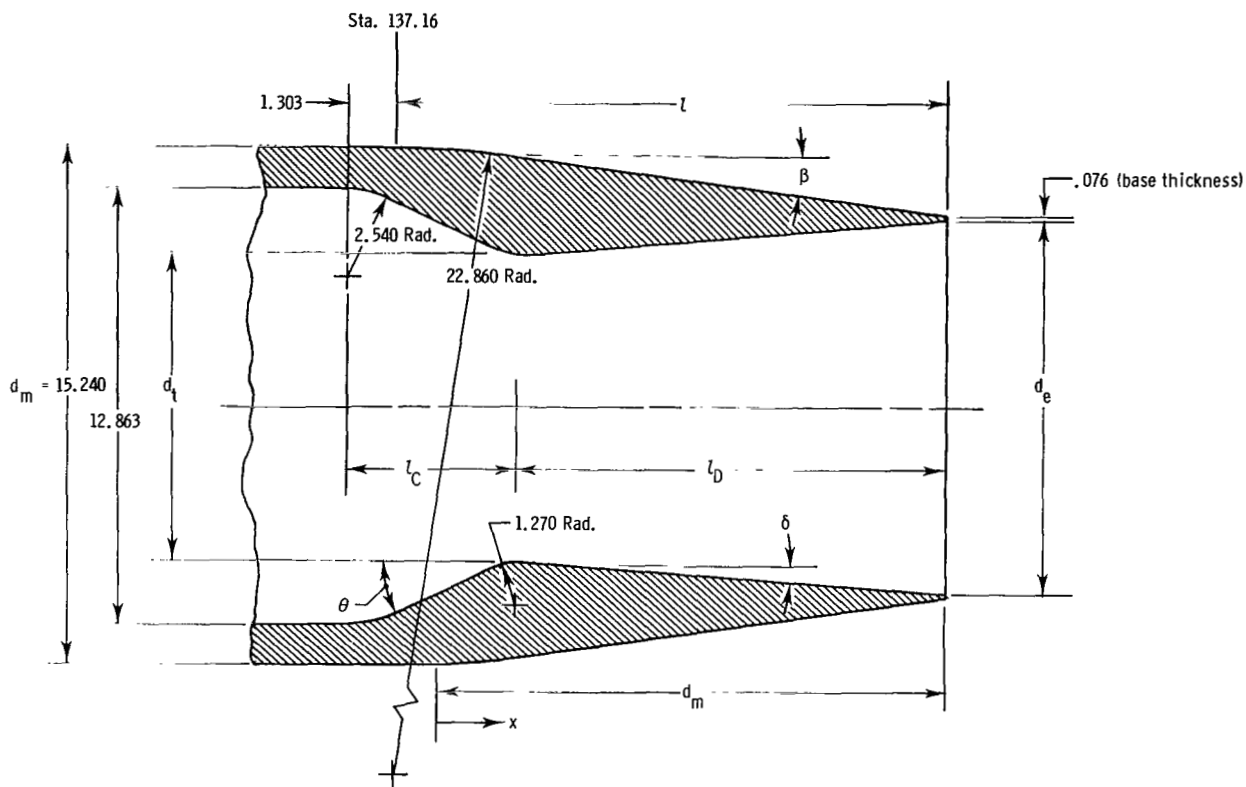
Configuration	Flight segment	Power setting	$(p_{t,j}/p_\infty)_{des}$	Design dimensions										
				A_e/A_t	A_t/A_m	A_e/A_m	d_t/d_m	l_C/d_m	l_D/d_m	θ, deg	δ, deg	l/d_m	d_e/d_m	β, deg
1	Subsonic cruise	Dry	4.25	1.250	0.250	0.312	0.500	0.286	0.800	42.35	2.12	1.000	0.559	15.05
2	Supersonic cruise	Dry	21.23	3.000	.250	.750	.500	.286	.779	42.35	13.18	.979	.866	3.82
3	Subsonic accel.	Max. dry	5.03	1.350	.300	.405	.548	.299	.799	33.58	3.18	1.012	.636	11.63
4	Transonic accel.	Partial A/B	6.23	1.500	.350	.525	.592	.309	.797	26.90	4.78	1.020	.725	8.28
5	Supersonic accel.	Max. A/B	10.64	2.000	.420	.840	.648	.319	.789	19.58	9.70	1.022	.917	2.12

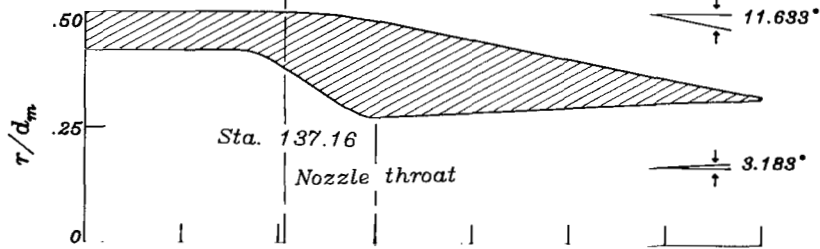Figure 4.- Geometric details of the test nozzle configurations. Absolute linear dimensions are in centimeters.

23

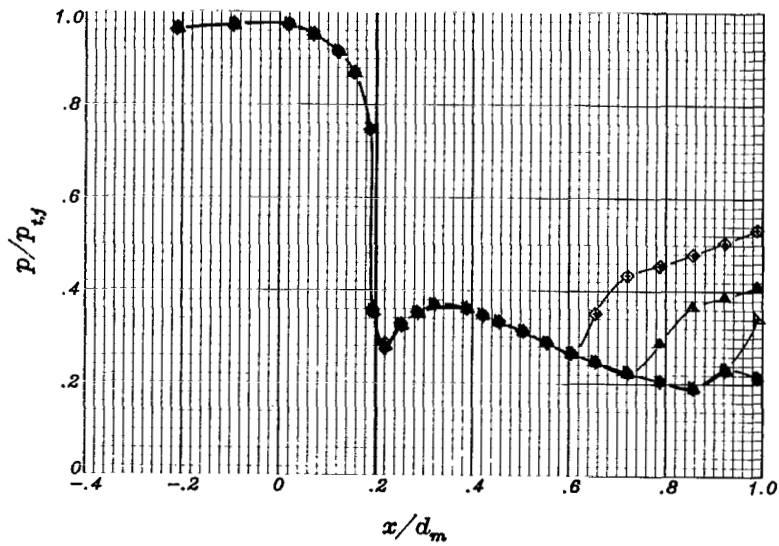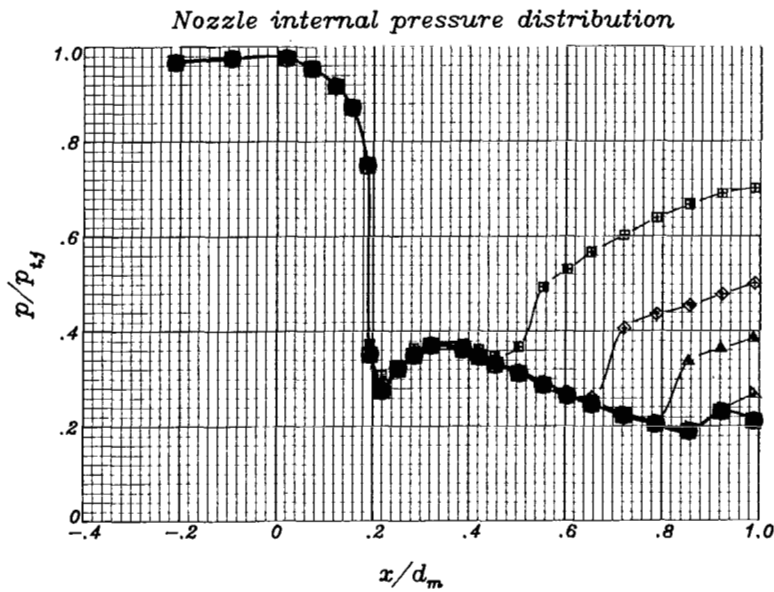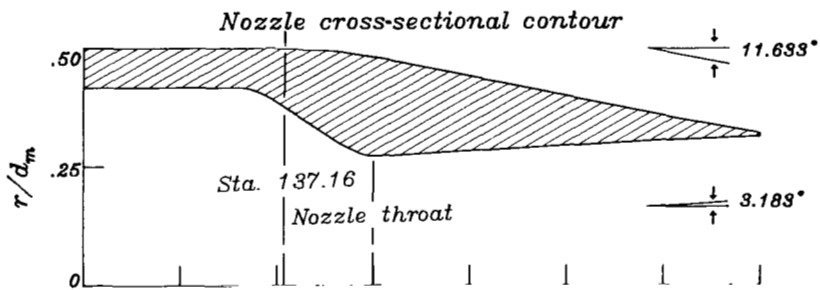*Nozzle external pressure distribution*
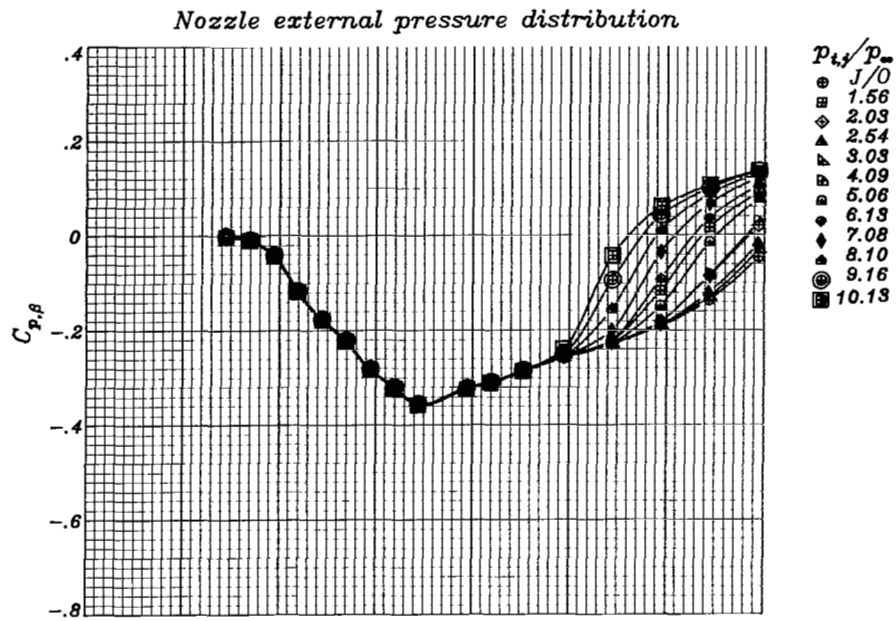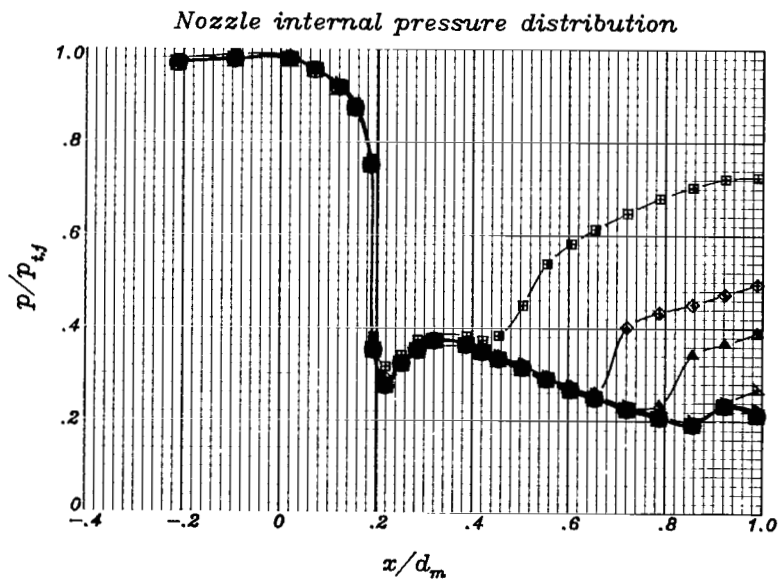
Nozzle cross-sectional contour

Nozzle internal pressure distribution

(a) $M_\infty = 0.60.$
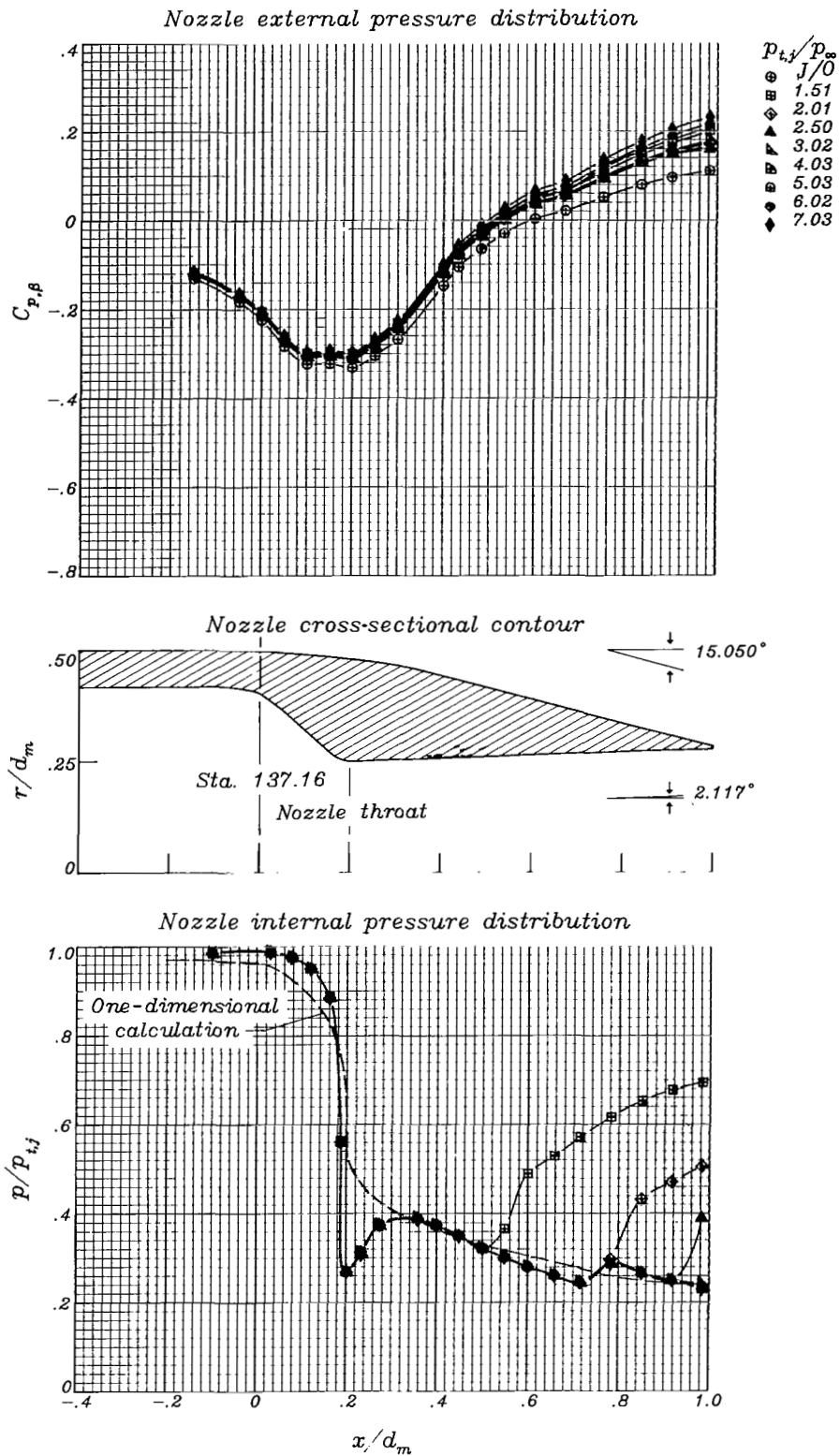
Figure 5.- External and internal surface-pressure distributions
of nozzle configuration 1. Origin is at start of boattail;
location of throat is denoted by vertical line in nozzle cross-
section contour; design nozzle pressure ratio is 4.25.

Nozzle external pressure distribution

$p_{t,j}/p_\infty$
- ⊕ $J/0$
- ⊞ 1.50
- ◈ 2.01
- ▲ 2.51
- ◤ 3.09
- ◩ 4.02
- ▣ 5.05
- ● 6.05
- ◆ 7.05

Nozzle cross-sectional contour

Sta. 137.16
Nozzle throat

15.050°

2.117°
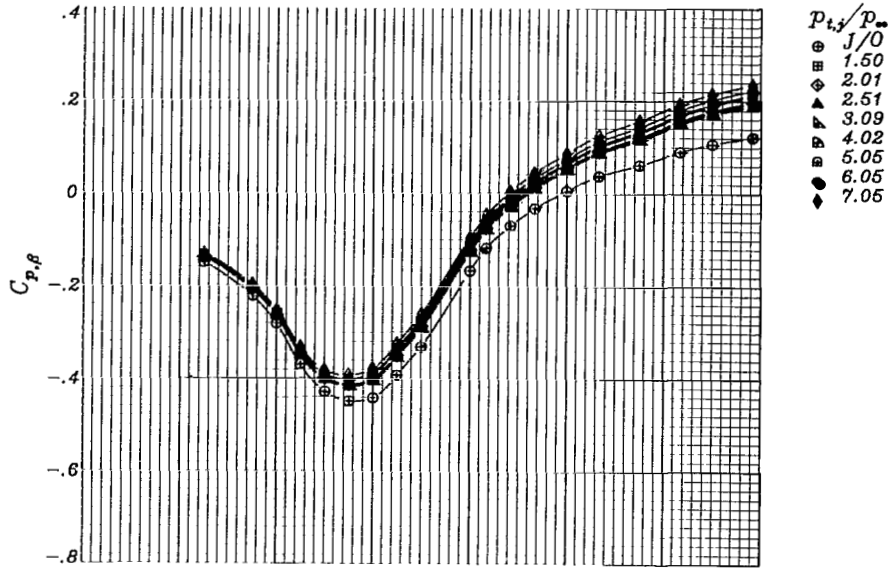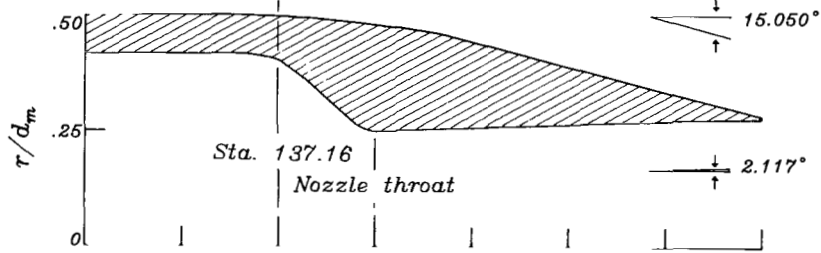
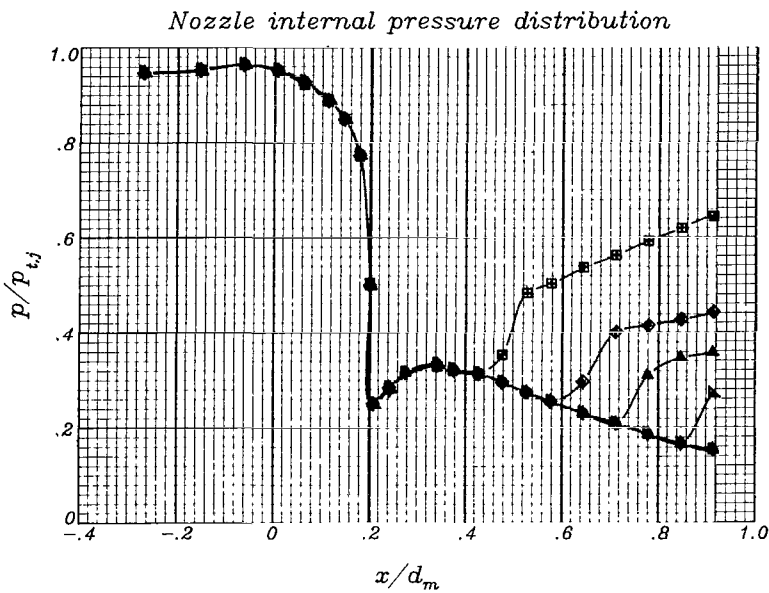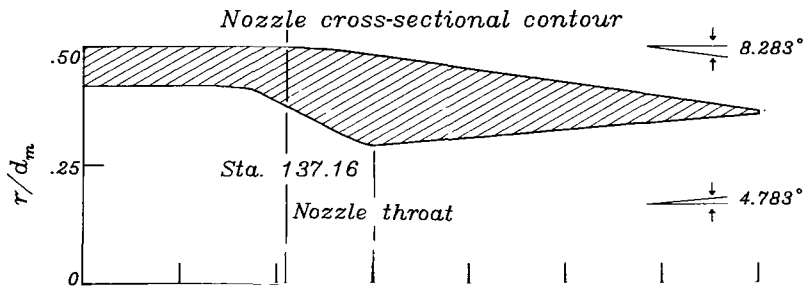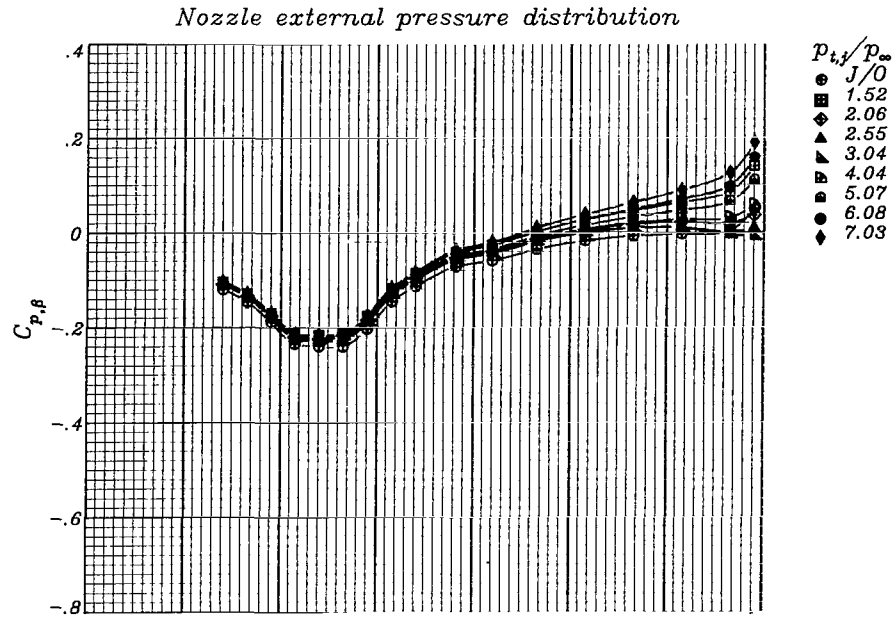## Nozzle internal pressure distribution

(b) $M_\infty = 0.80$.

Figure 5.- Continued.

Nozzle external pressure distribution

$p_{t,j}/p_\infty$

⊕	J/0
⊞	1.53
◇	2.03
▲	2.55
◣	3.03
▶	4.05
⊠	5.09
●	6.05
◆	7.05

Nozzle cross-sectional contour

15.050°

Sta. 137.16

Nozzle throat

2.117°
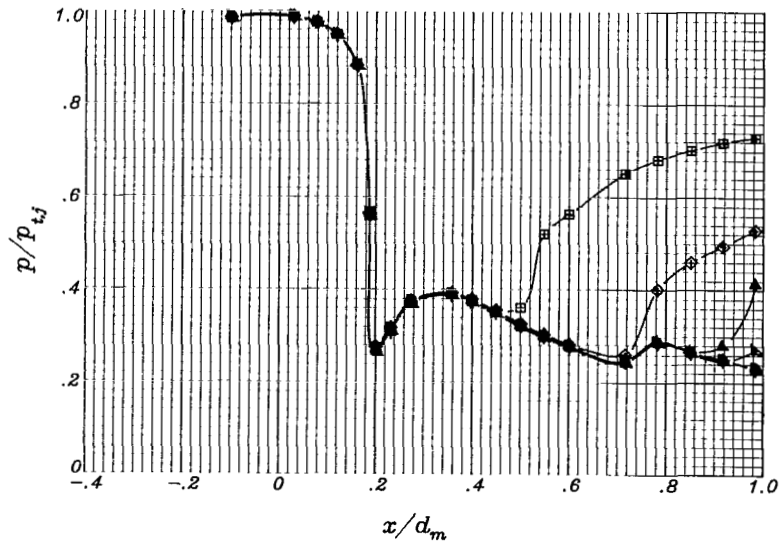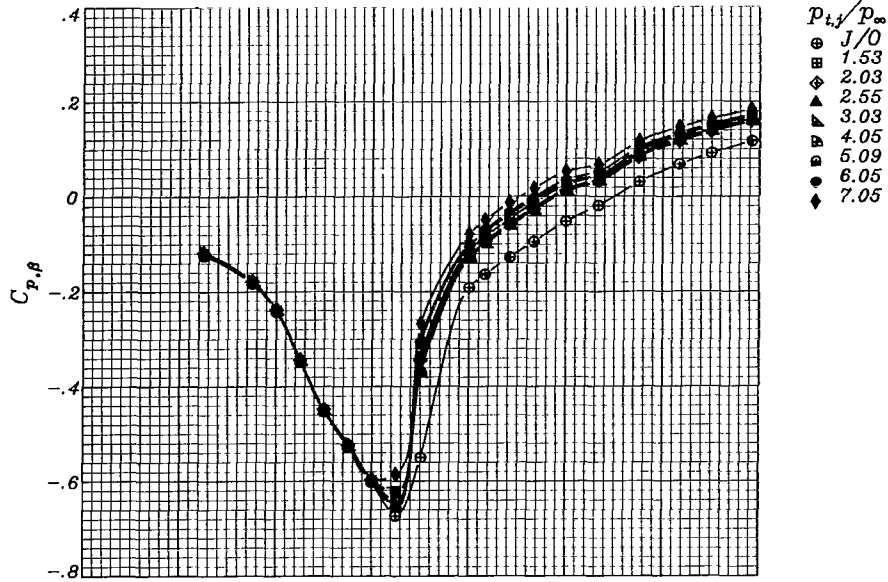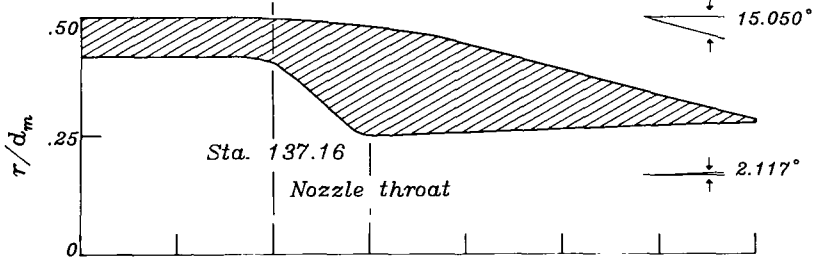
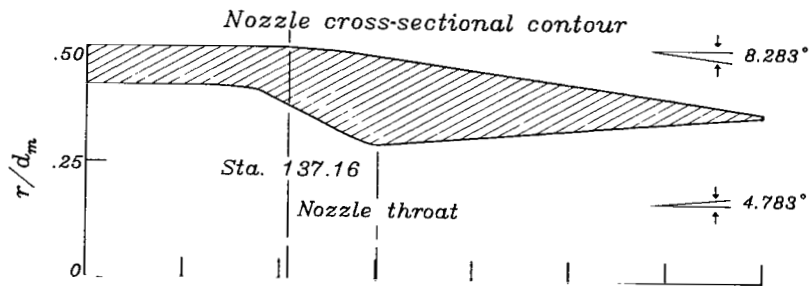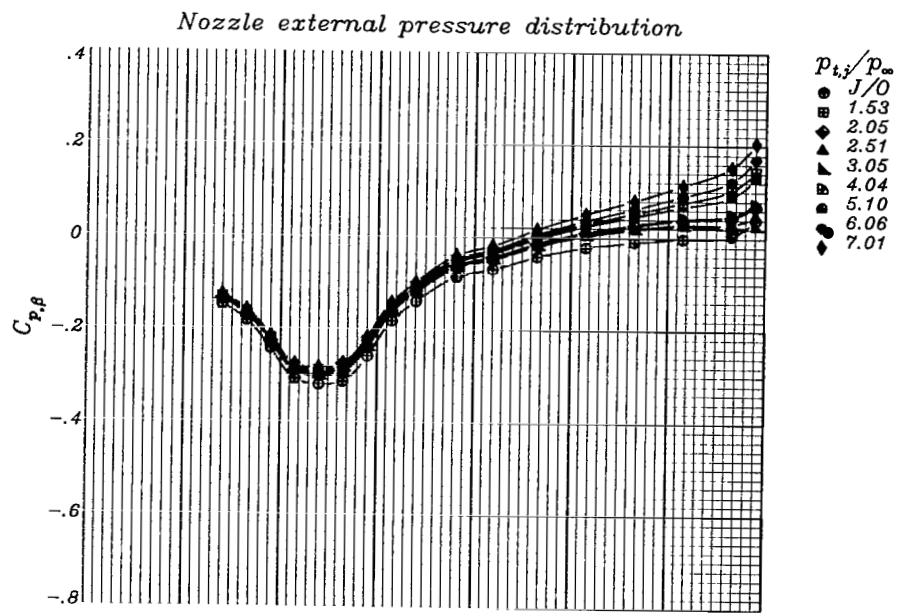## Nozzle internal pressure distribution

(c) $M_\infty = 0.90$.

Figure 5.- Continued.
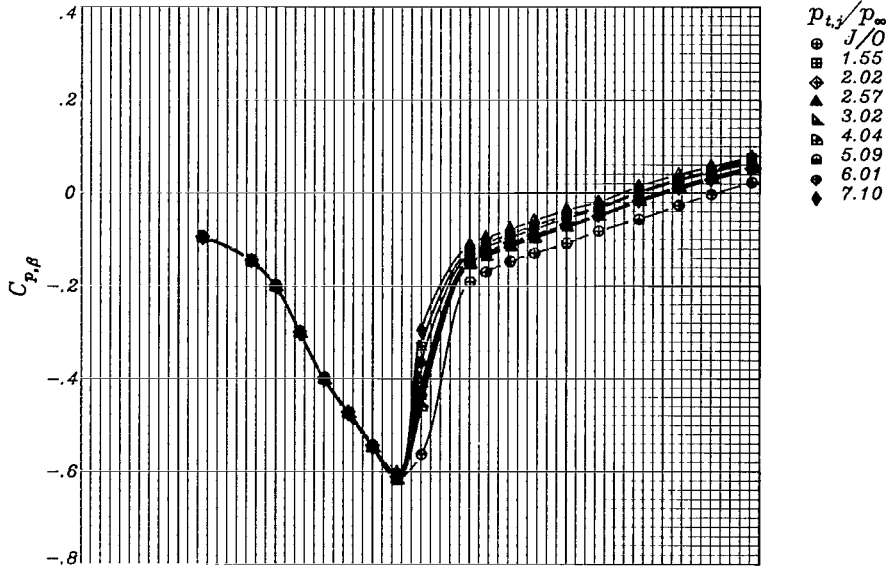
Nozzle external pressure distribution

$p_{t,j}/p_\infty$
- ⊕ *J/O*
- ⊞ *1.55*
- ◈ *2.02*
- ▲ *2.57*
- ◣ *3.02*
- ◪ *4.04*
- ◓ *5.09*
- ◉ *6.01*
- ◆ *7.10*

Nozzle cross-sectional contour

15.050°

Sta. 137.16

Nozzle throat

2.117°

Nozzle internal pressure distribution

x/d_m

(d) M_∞ = 0.94.

Figure 5.- Continued.

Nozzle external pressure distribution

	$p_{t,j}/p_\infty$
⊕	J/0
⊞	1.50
◈	2.04
▲	2.57
◤	3.04
◭	4.09
⬠	5.12
⬥	6.13
◆	7.13
▲	8.12
⊛	9.17
▣	10.10

Nozzle cross-sectional contour

15.050°

2.117°

Sta. 137.16

Nozzle throat
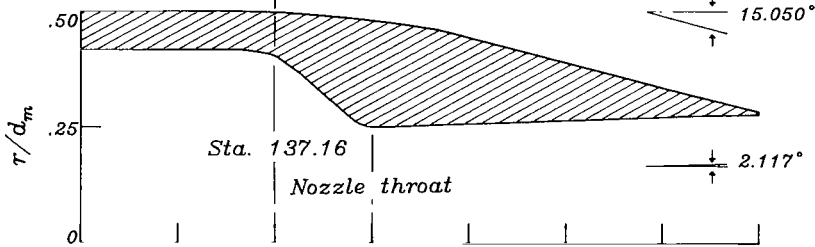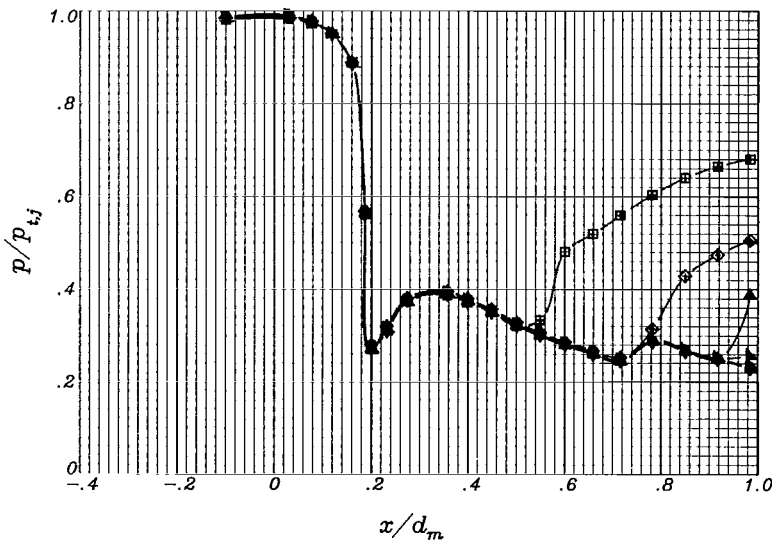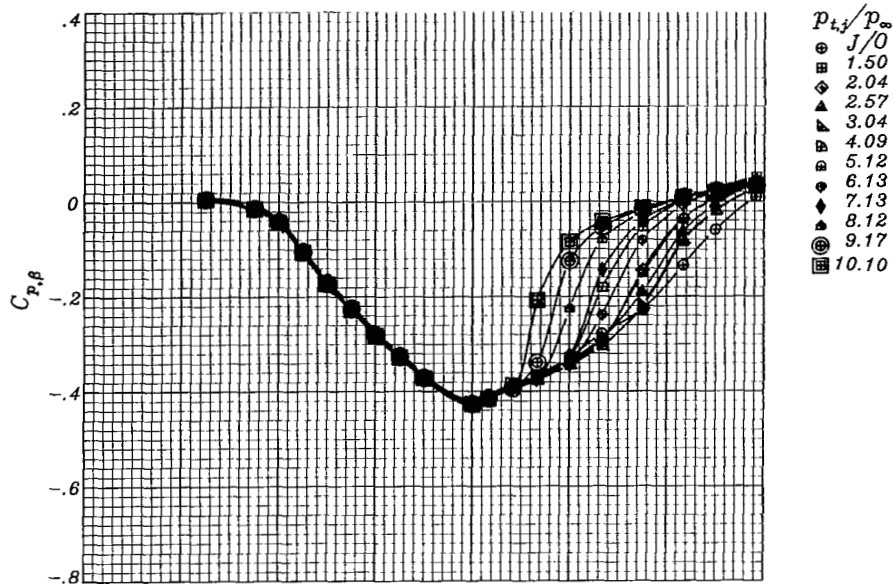
Nozzle internal pressure distribution

(e) $M_\infty = 1.20$.

Figure 5.- Continued.

Nozzle external pressure distribution

$p_{t,j}/p_\infty$
⊕ J/O
⊞ 1.57
◇ 2.04
▲ 2.53
◣ 3.00
◪ 4.05
⌂ 4.98
♡ 5.96
◆ 6.98
▲ 7.98
◉ 8.98
⊞ 10.00

Nozzle cross-sectional contour

Sta. 137.16

Nozzle throat

15.050°

2.117°

Nozzle internal pressure distribution
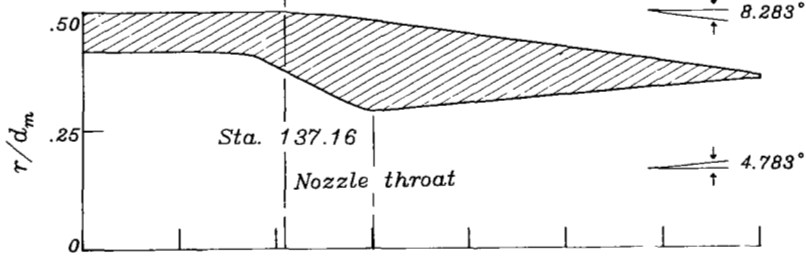
x/d_m
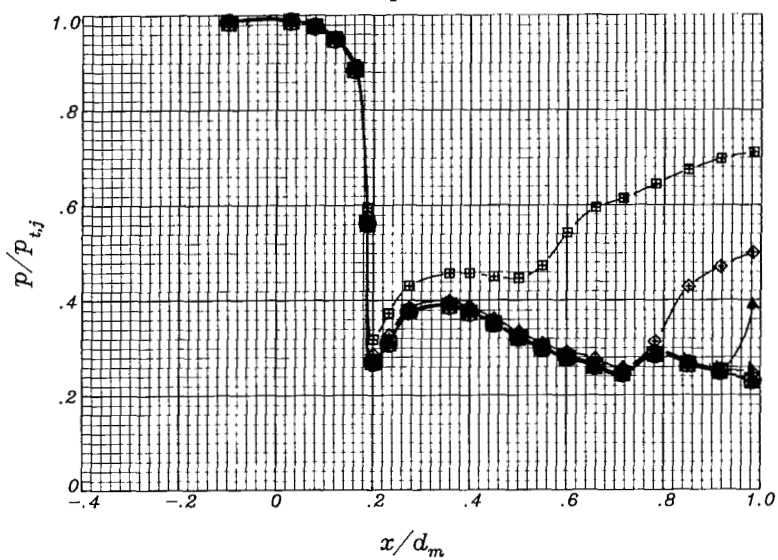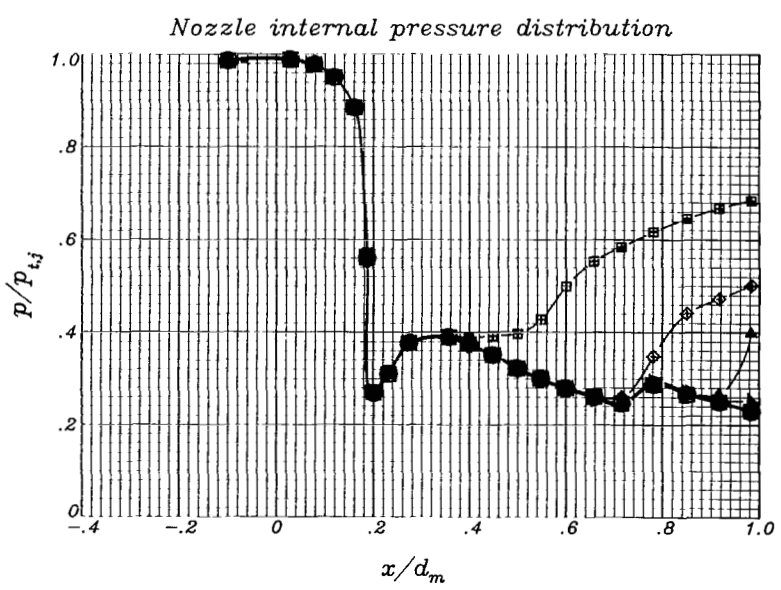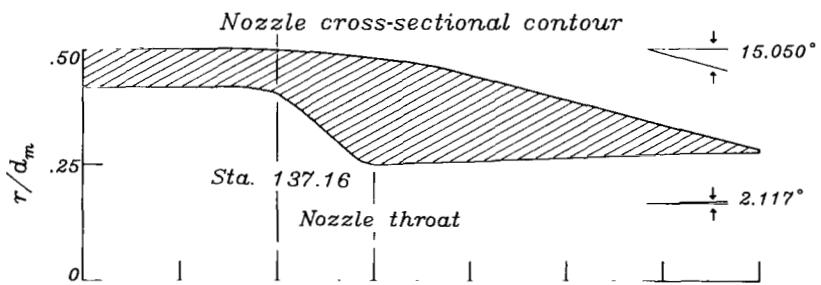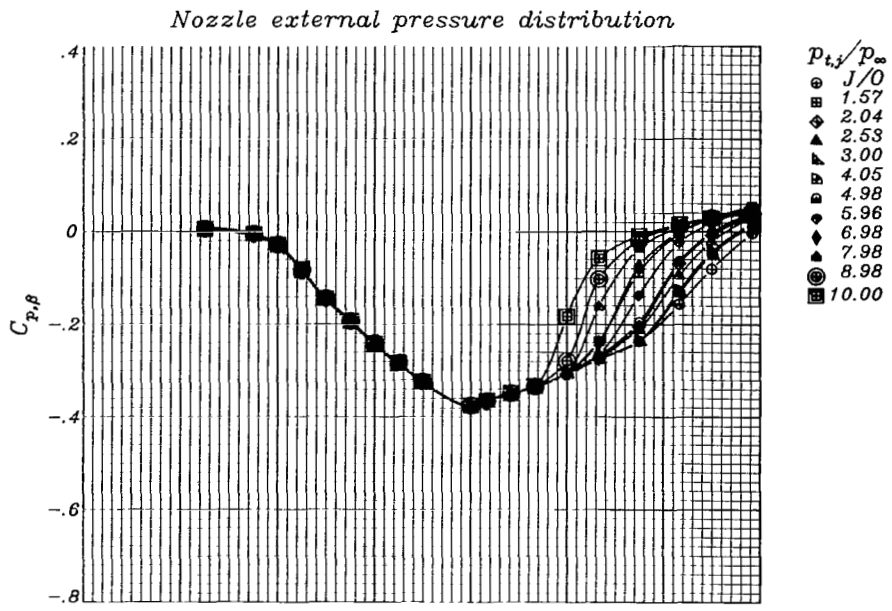
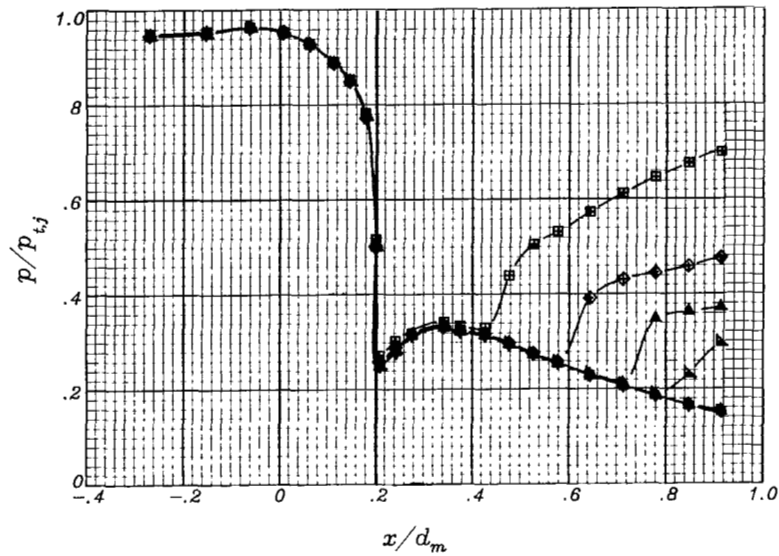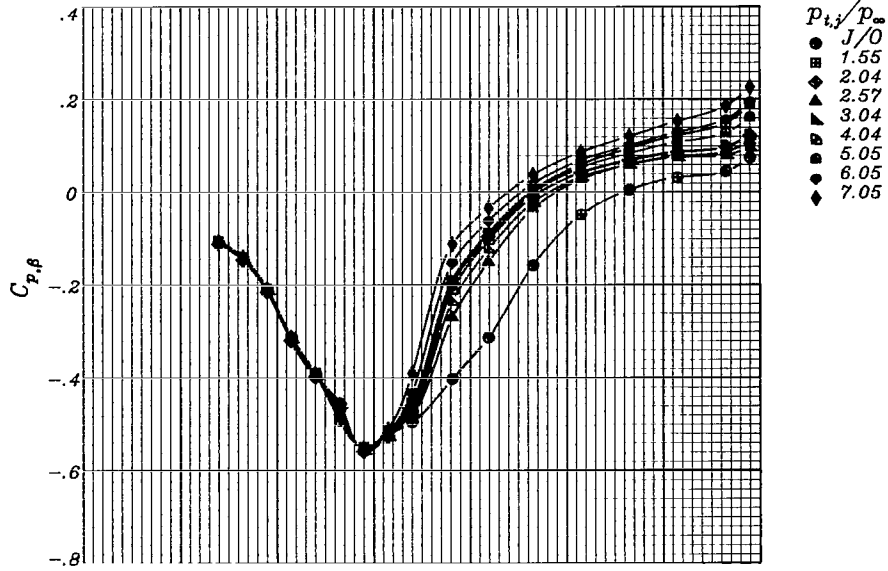(f) $M_\infty = 1.28.$

Figure 5.- Concluded.

Nozzle external pressure distribution

Nozzle cross-sectional contour
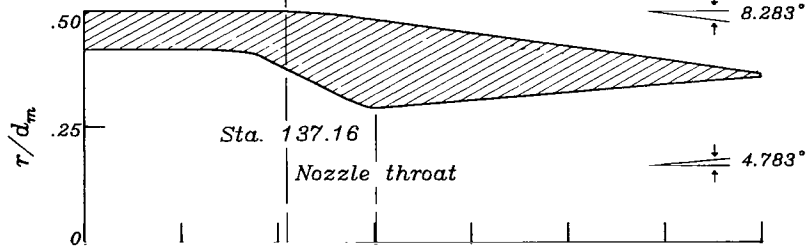

Nozzle internal pressure distribution
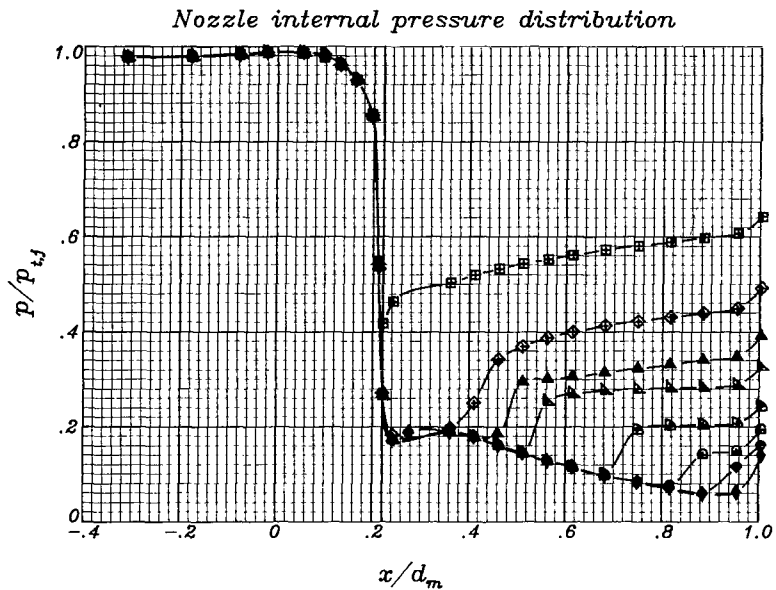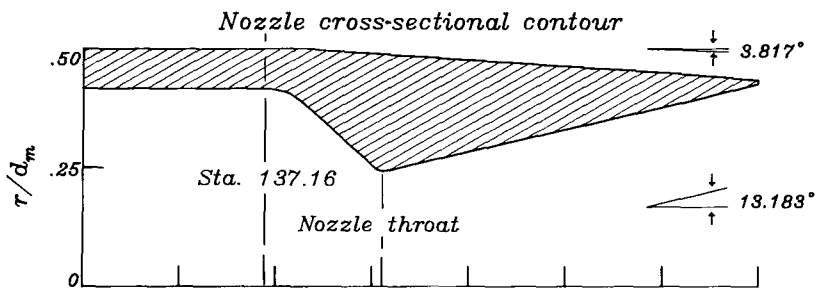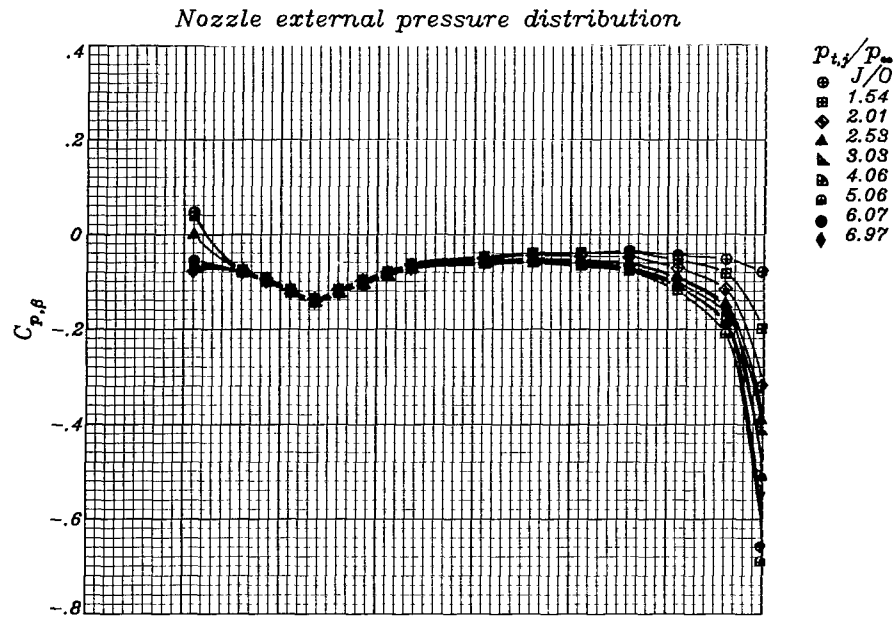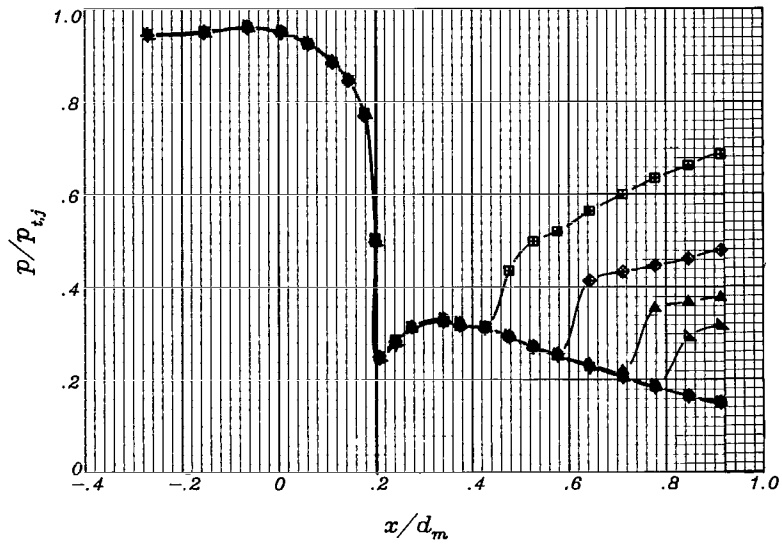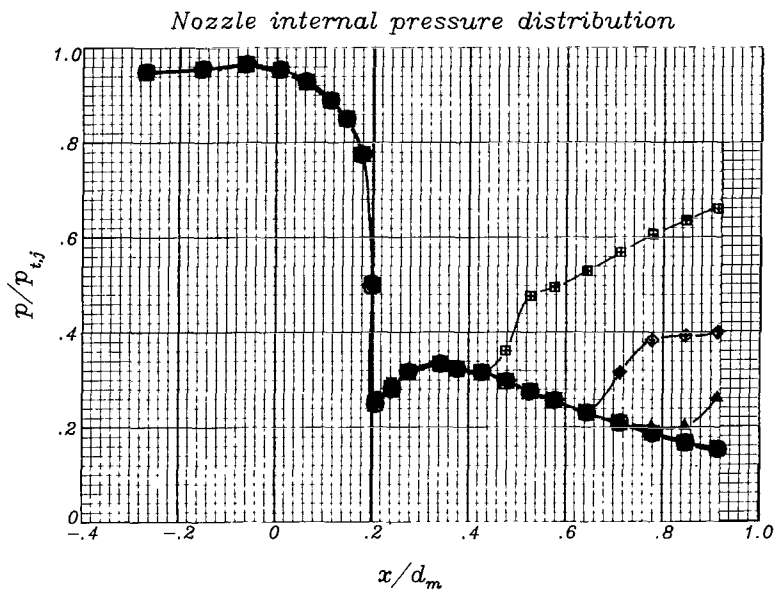

(a) $M_\infty = 0.60$.

Figure 6.- External and internal surface-pressure distributions
of nozzle configuration 2. Origin is at start of boattail;
location of throat is denoted by vertical line in nozzle cross-
section contour; design nozzle pressure ratio is 21.23.

Nozzle external pressure distribution

$p_{t,j}/p_\infty$
- ⊕ $J/0$
- ⊞ 1.55
- ◈ 2.02
- ▲ 2.58
- ◤ 3.02
- ◪ 4.03
- ▣ 5.08
- ● 6.09
- ◆ 7.11

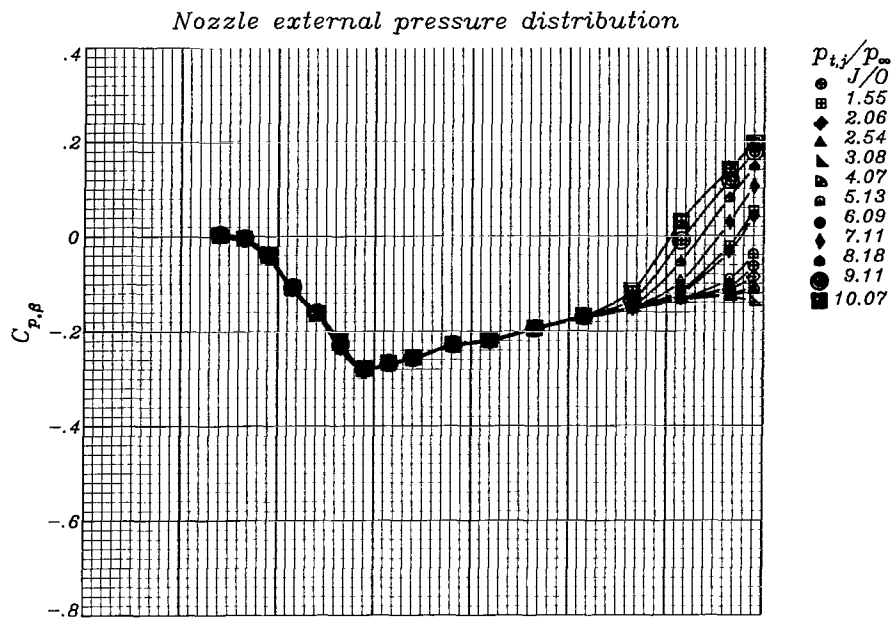Nozzle cross-sectional contour

Sta. 137.16

Nozzle throat

3.817°

13.183°

Nozzle internal pressure distribution

x/d_m

(b) $M_\infty = 0.80.$

Figure 6.- Continued.

31

Nozzle external pressure distribution

$p_{t,j}/p_\infty$

⊕ J/0
⊞ 1.56
◈ 2.03
▲ 2.49
◣ 3.01
▣ 4.07
⊟ 5.09
● 6.08
◆ 7.08

Nozzle cross-sectional contour

3.817°

Sta. 137.16

Nozzle throat

13.183°

Nozzle internal pressure distribution

x/d_m

(c) $M_\infty = 0.90$.

Figure 6.- Continued.

Nozzle external pressure distribution

$p_{t,j}/p_\infty$
⊕ $J/0$
▣ 1.51
◈ 2.12
▲ 2.66
◣ 3.01
◩ 3.99
⬟ 5.09
● 6.10
◆ 7.07

Nozzle cross-sectional contour
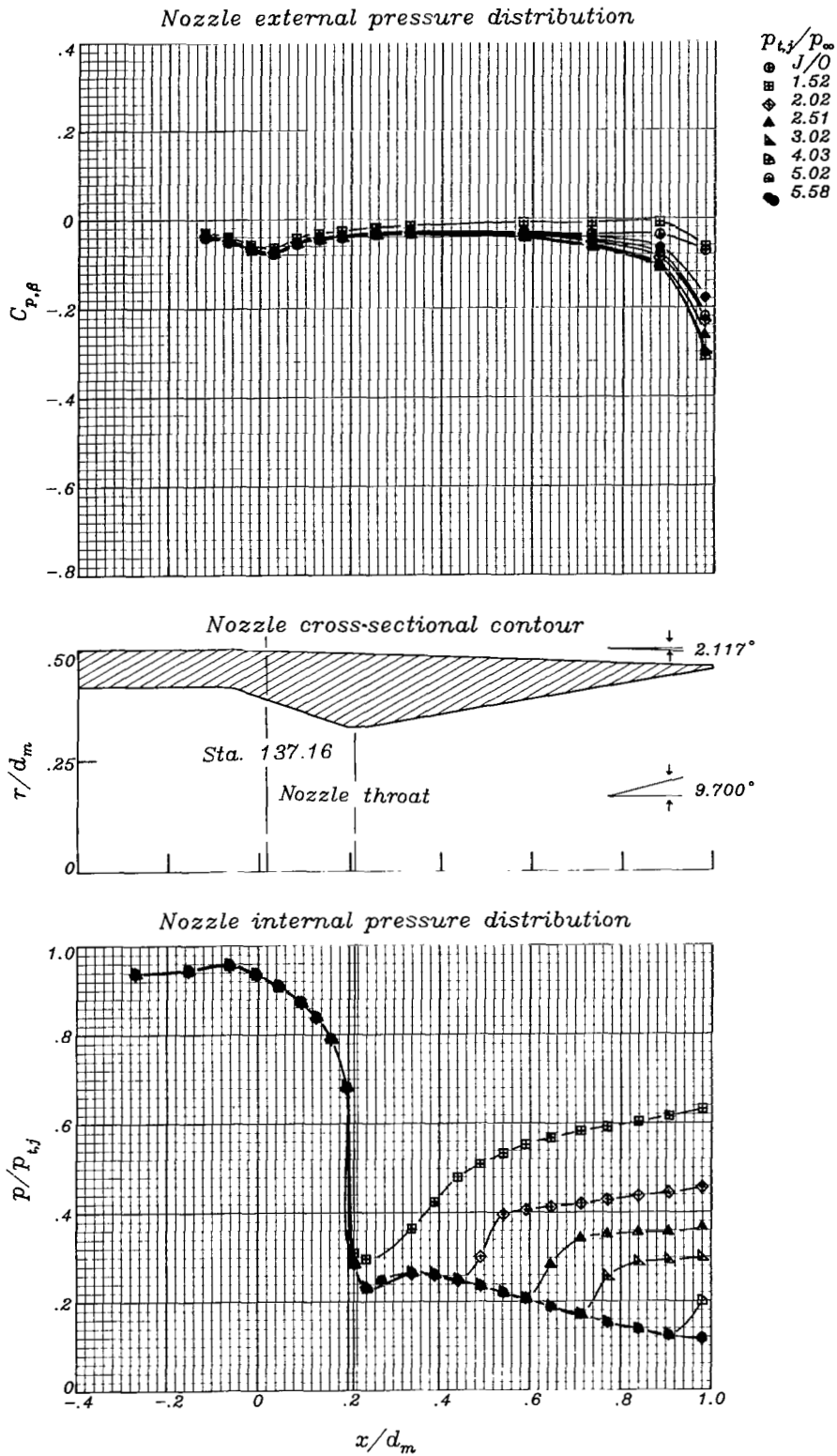

↓ $3.817°$

Sta. 137.16

Nozzle throat

↓ $13.183°$

Nozzle internal pressure distribution

(d) $M_\infty = 0.94$.

Figure 6.- Continued.

Nozzle external pressure distribution

$p_{t,j}/p_\infty$
- ⊕ J/0
- ⊞ 1.51
- ◈ 2.02
- ▲ 2.61
- ◤ 3.03
- ▷ 4.00
- ⬠ 5.21
- ⬟ 6.10
- ◆ 7.13
- ▲ 8.15
- ⊚ 9.09
- ⊡ 10.08

$C_{p,\beta}$

Nozzle cross-sectional contour

r/d_m

3.817°

Sta. 137.16

Nozzle throat

13.183°

Nozzle internal pressure distribution

$p/p_{t,j}$

x/d_m

(e) $M_\infty = 1.20$.

Figure 6.- Continued.

Nozzle external pressure distribution

	$p_{t,j}/p_\infty$
⊕	J/O
⊞	1.69
◈	2.01
▲	2.47
◣	2.99
◙	3.99
◖	4.98
●	6.01
◆	6.96
▲	7.96
⊕	9.01
▦	9.92

Nozzle cross-sectional contour

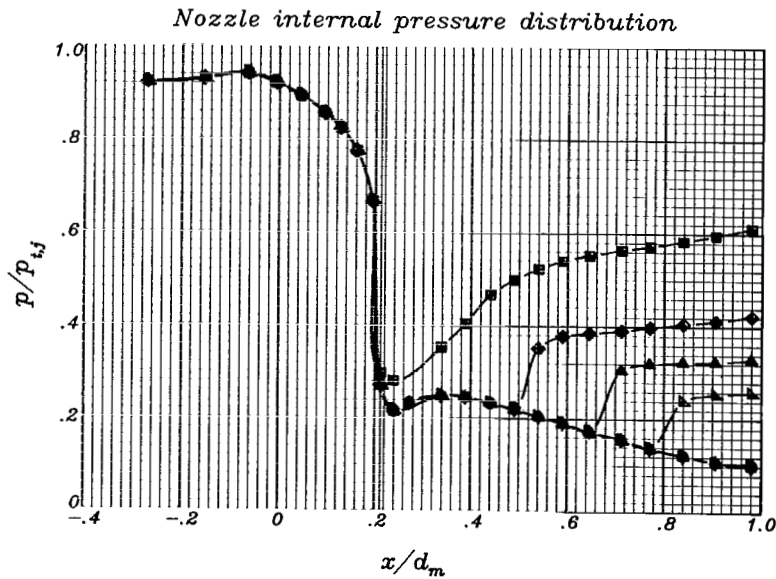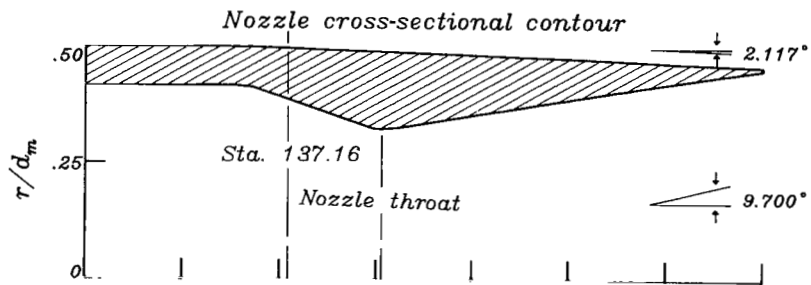Sta. 137.16

Nozzle throat

3.817°

13.183°

Nozzle internal pressure distribution

x/d_m

(f) $M_\infty = 1.28$.

Figure 6.- Concluded.

Nozzle external pressure distribution

$p_{t,j}/p_\infty$

- J/0
- 1.52
- 2.04
- 2.51
- 3.02
- 4.01
- 5.03
- 6.02
- 7.04

$C_{p,\beta}$

Nozzle cross-sectional contour

r/d_m

11.633°

Sta. 137.16

Nozzle throat

3.183°

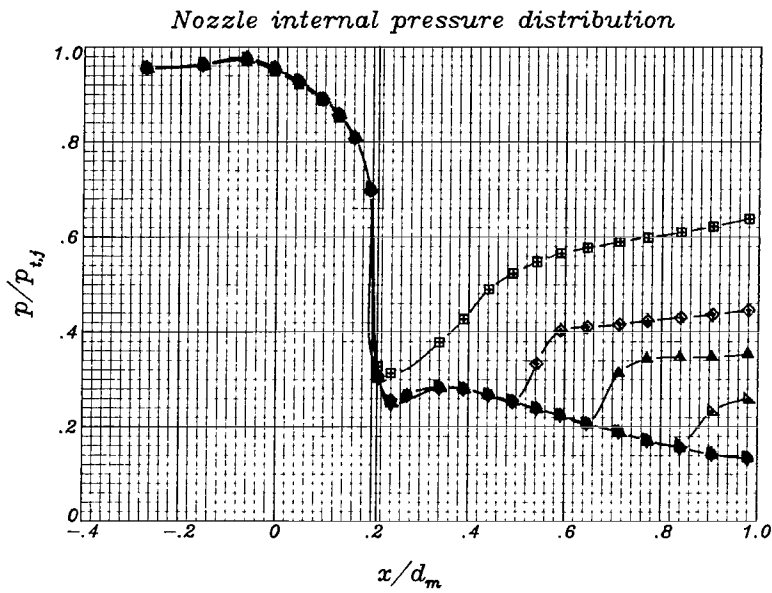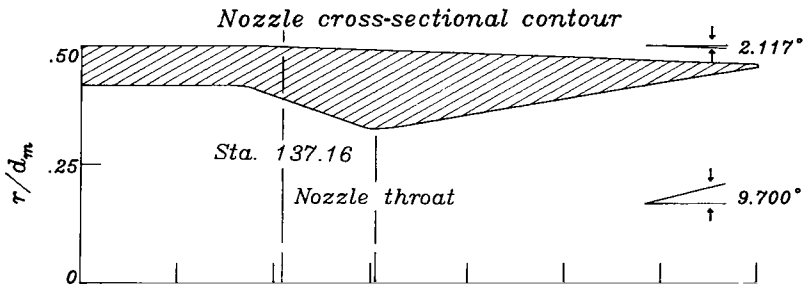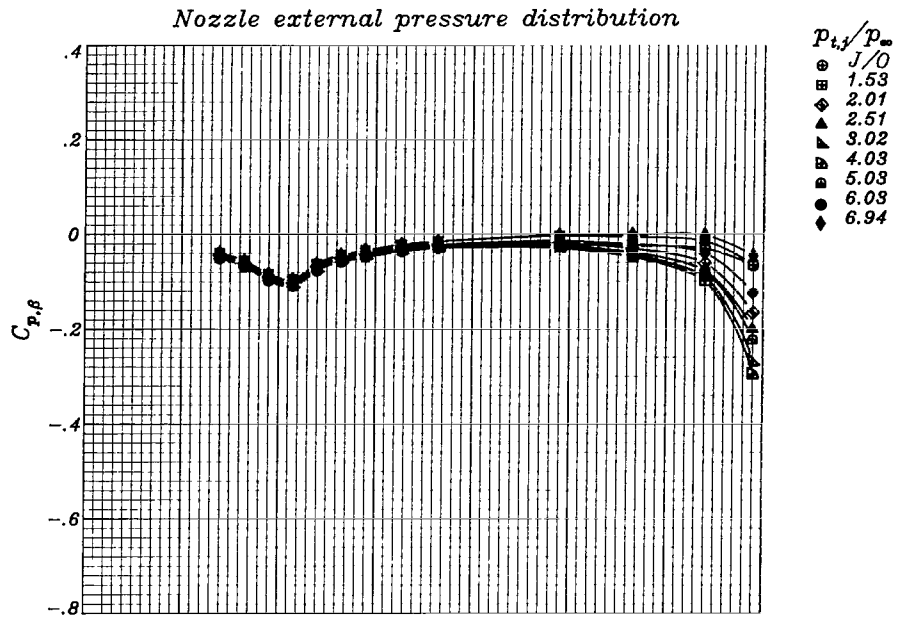## Nozzle internal pressure distribution

$p/p_{t,j}$

x/d_m
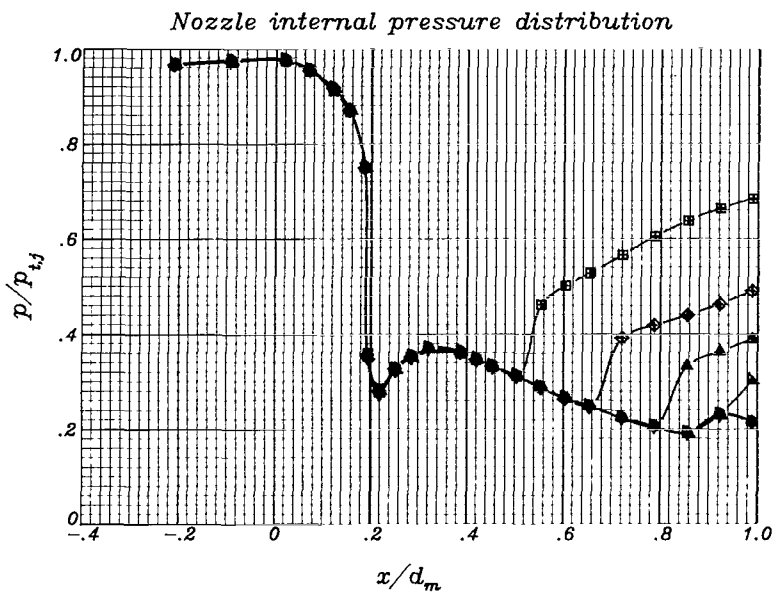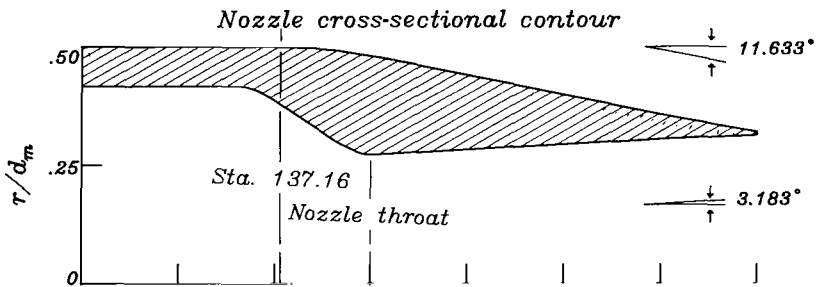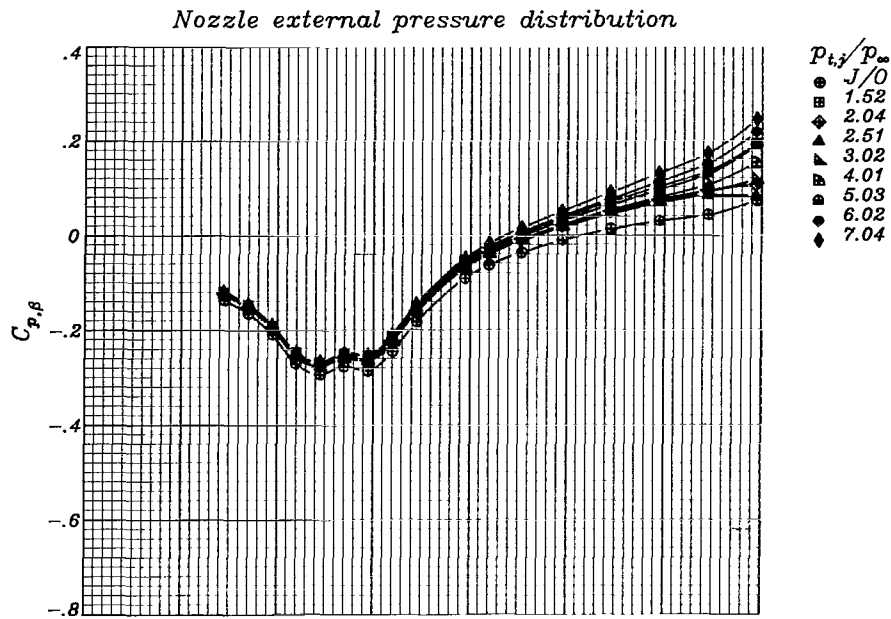
(a) $M_\infty = 0.60$.

Figure 7.- External and internal surface-pressure distributions
of nozzle configuration 3. Origin is at start of boattail;
location of throat is denoted by vertical line in nozzle cross-
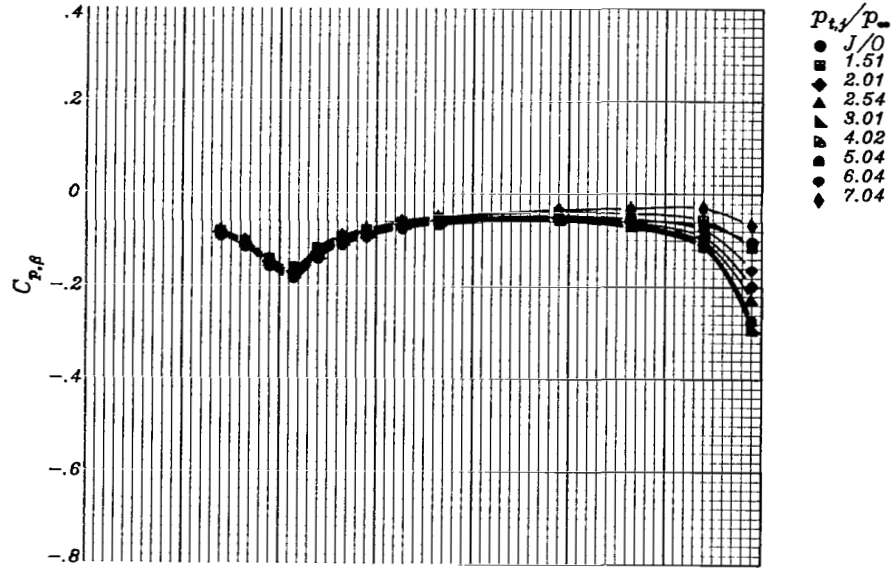section contour; design nozzle pressure ratio is 5.03.

Nozzle external pressure distribution

$p_{t,j}/p_\infty$

- ⊕ J/0
- ⊞ 1.50
- ◇ 2.02
- ▲ 2.53
- ◣ 3.03
- ◪ 4.03
- ⊡ 5.05
- ● 6.03
- ◆ 7.00

Nozzle cross-sectional contour

Sta. 137.16

Nozzle throat

11.633°

3.183°
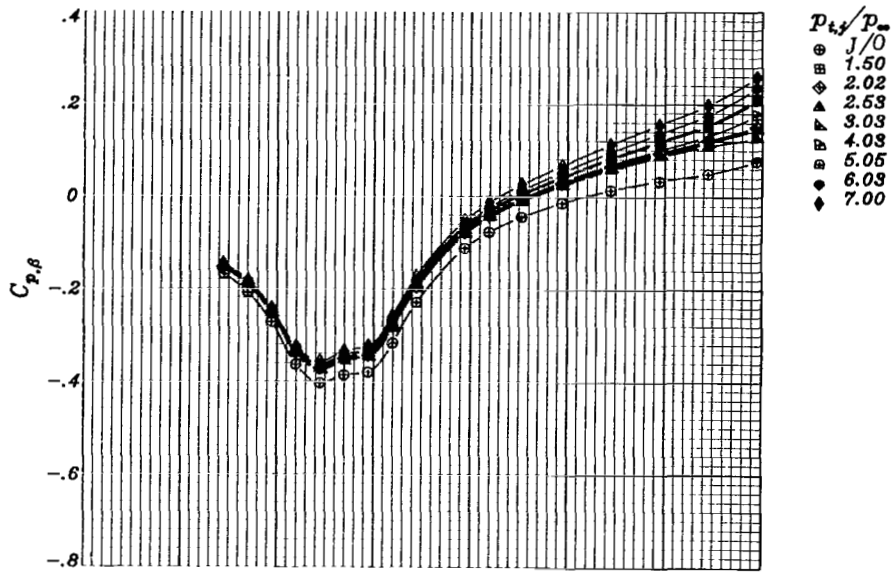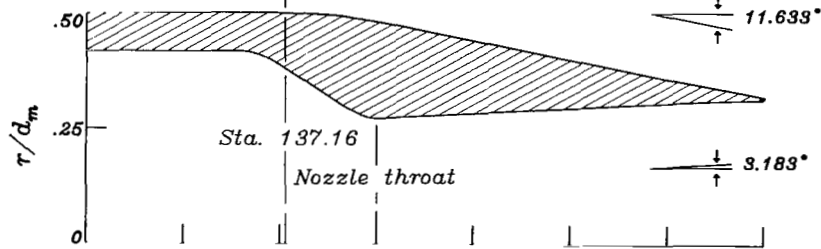
Nozzle internal pressure distribution

(b) $M_\infty = 0.80.$

Figure 7.- Continued.

Nozzle external pressure distribution

$p_{t,j}/p_\infty$
- ⊕ J/0
- ⊞ 1.51
- ◈ 2.02
- ▲ 2.52
- ◣ 3.03
- ⬗ 4.03
- ⊞ 5.04
- ● 6.03
- ◆ 7.03

Nozzle cross-sectional contour

11.633°

Sta. 137.16

Nozzle throat

3.183°

Nozzle internal pressure distribution
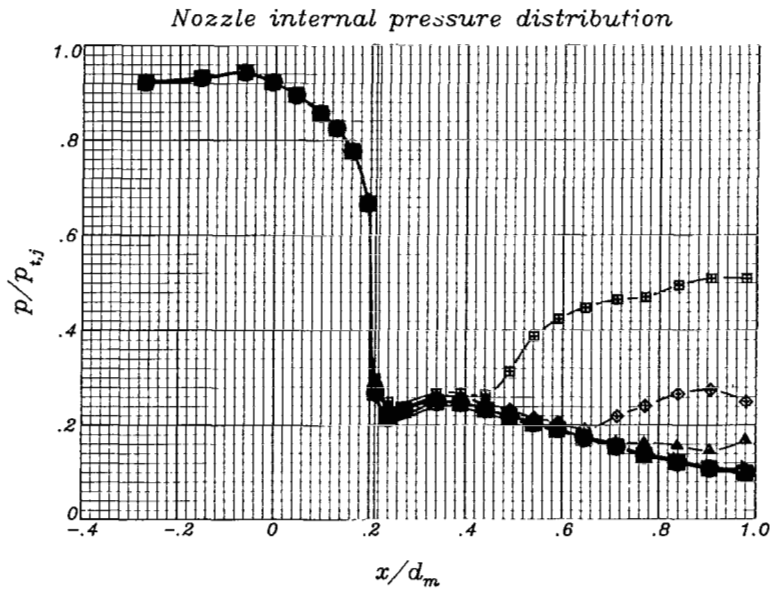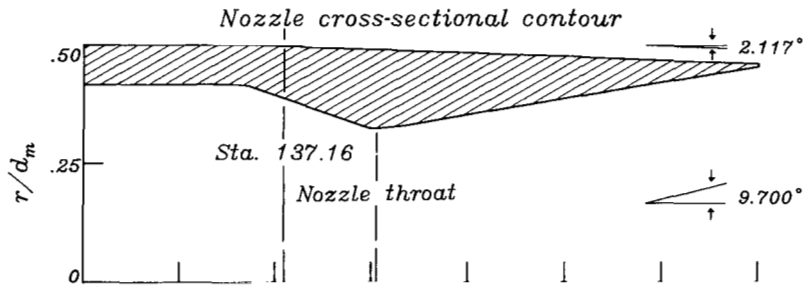

(c) $M_\infty = 0.90$.

Figure 7.- Continued.

Nozzle external pressure distribution

$$p_{t,j}/p_\infty$$

⊕	J/0
◈	2.03
▲	2.59
◤	3.03
◨	4.08
⬢	5.05
●	6.06
◆	7.06

$C_{p,\beta}$

Nozzle cross-sectional contour

r/d_m

11.633°

3.183°

Sta. 137.16

Nozzle throat

Nozzle internal pressure distribution

$p/p_{t,j}$

x/d_m

(d) $M_\infty = 0.94.$

Figure 7.- Continued.

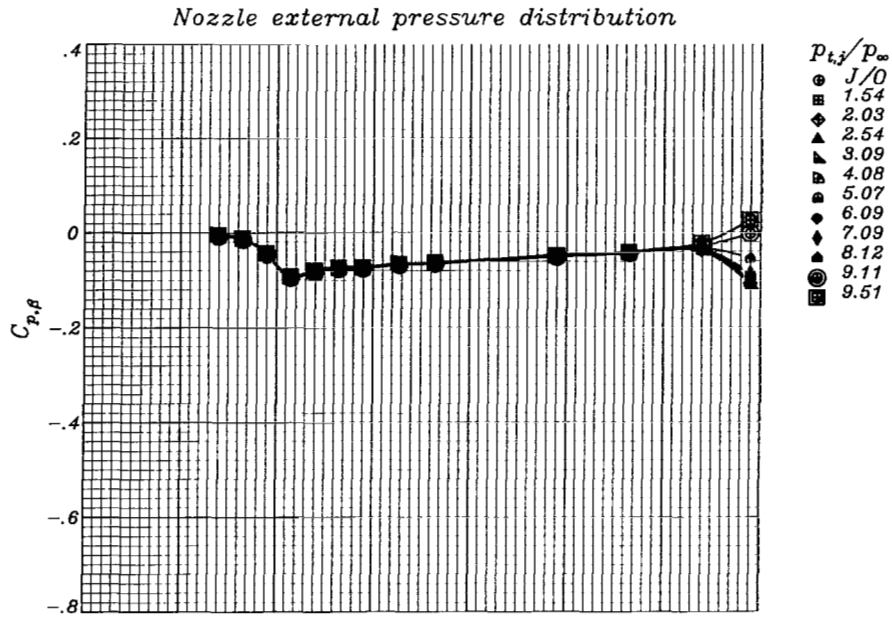Nozzle external pressure distribution

Nozzle cross-sectional contour

Nozzle internal pressure distribution

(e) $M_\infty = 1.20$.
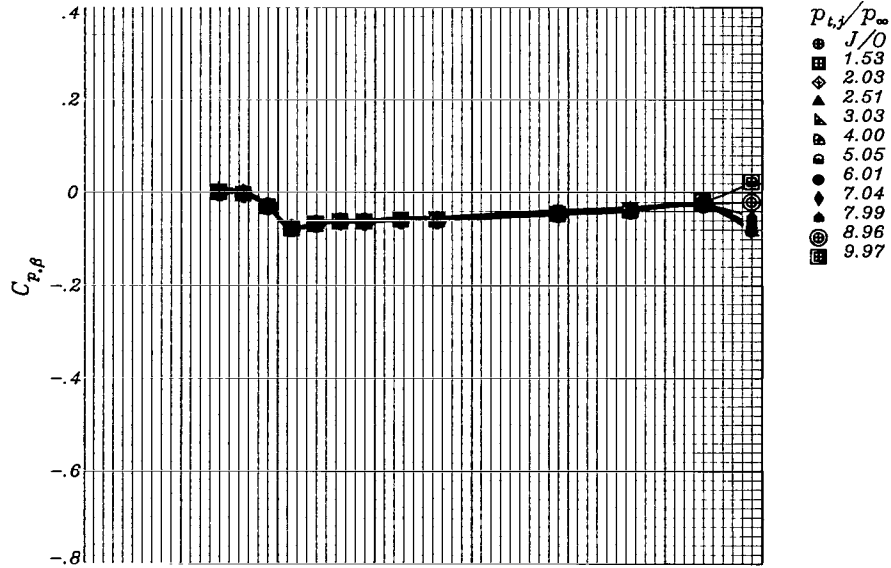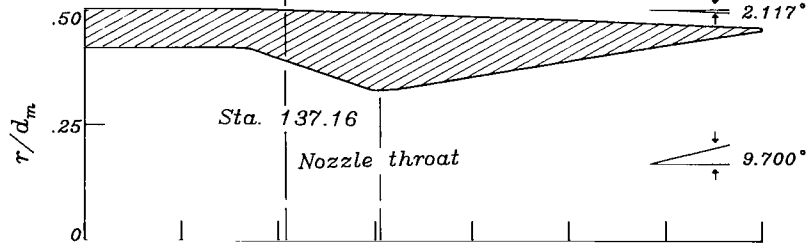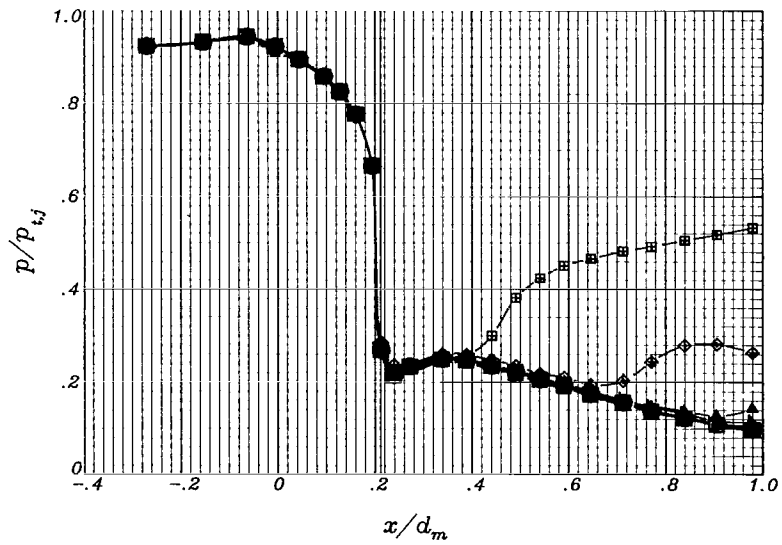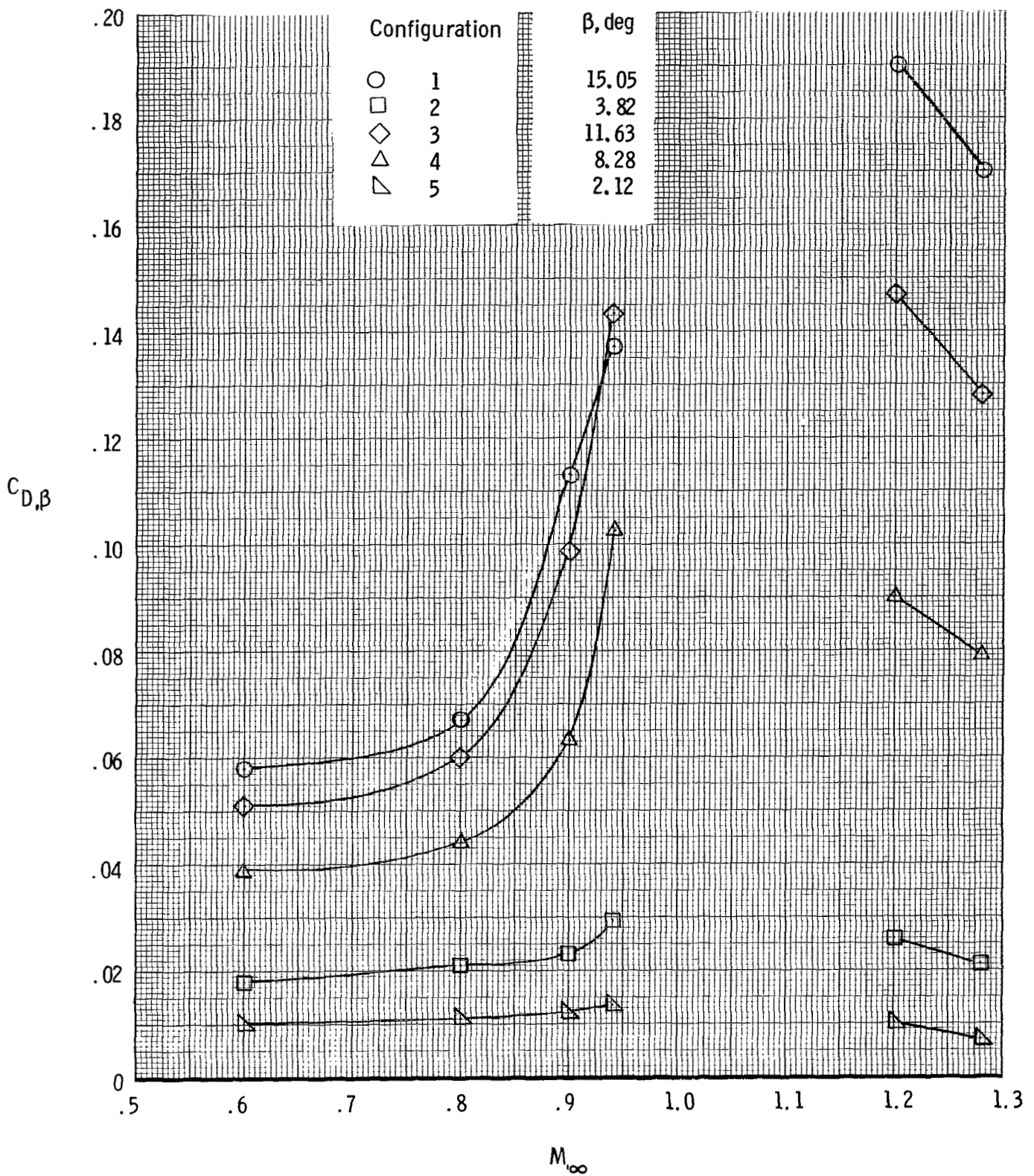
Figure 7.- Continued.

Nozzle external pressure distribution

$p_{t,j}/p_\infty$	
⊕	J/0
⊞	1.51
◈	2.03
▲	2.51
◣	2.95
◩	3.97
◨	4.99
●	6.02
◆	6.97
▲	8.02
◉	8.98
⊞	9.94

Nozzle cross-sectional contour

Sta. 137.16

Nozzle throat

11.633°

3.183°

Nozzle internal pressure distribution

x/d_m
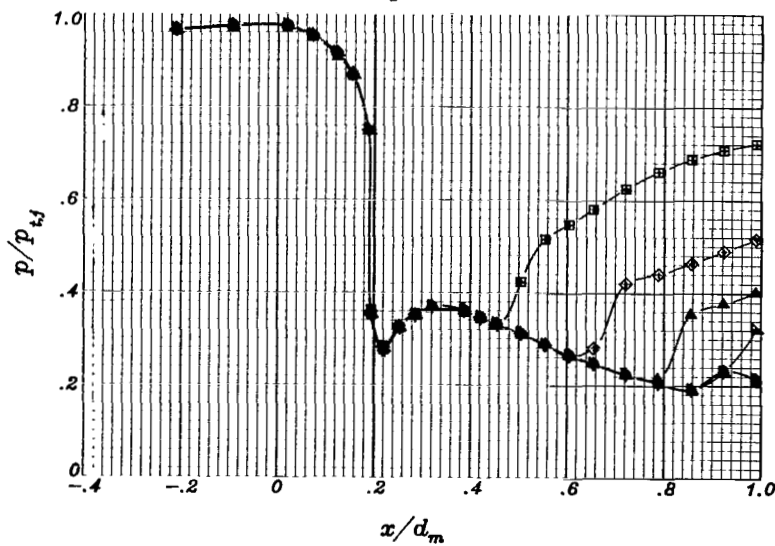
(f) $M_\infty = 1.28$.

Figure 7.- Concluded.

Figure 8.- External and internal surface-pressure distributions
of nozzle configuration 4. Origin is at start of boattail;
location of throat is denoted by vertical line in nozzle cross-
section contour; design nozzle pressure ratio is 6.23.

Nozzle external pressure distribution

$p_{t,j}/p_\infty$
- J/O
- 1.53
- 2.05
- 2.51
- 3.05
- 4.04
- 5.10
- 6.06
- 7.01

Nozzle cross-sectional contour

8.283°

Sta. 137.16

Nozzle throat

4.783°

Nozzle internal pressure distribution
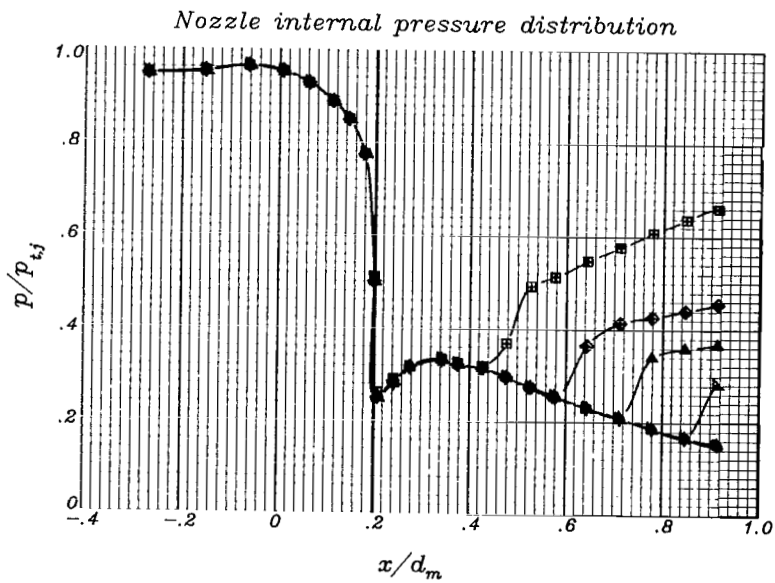
(b) $M_\infty = 0.80.$

Figure 8.- Continued.

Nozzle external pressure distribution

Nozzle cross-sectional contour

Nozzle internal pressure distribution
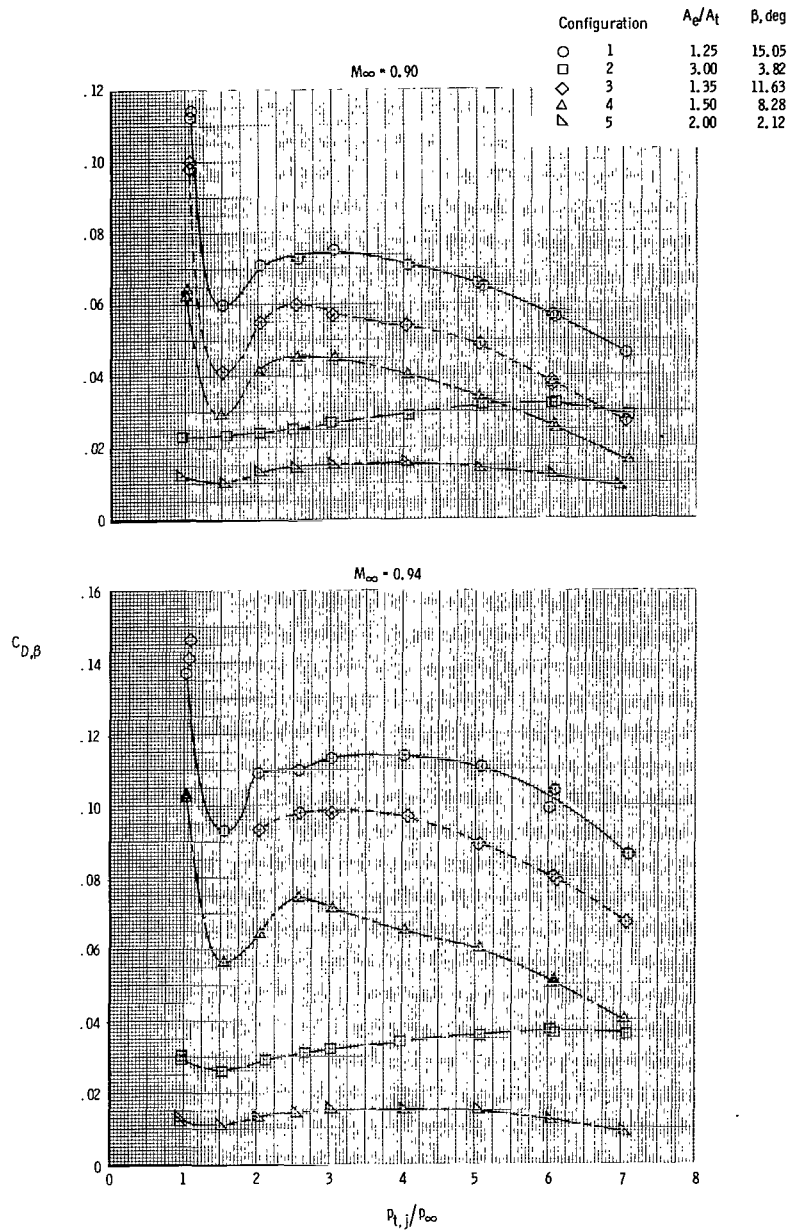
(c) M$_\infty$ = 0.90.

Figure 8.- Continued.

Nozzle external pressure distribution

$$p_{t,j}/p_\infty$$

●	J/0
▦	1.55
◆	2.04
▲	2.57
◣	3.04
◩	4.04
◒	5.05
●	6.05
◆	7.05

Nozzle cross-sectional contour

Sta. 137.16

Nozzle throat

8.283°

4.783°

Nozzle internal pressure distribution

(d) $M_\infty = 0.94$.

Figure 8.- Continued.
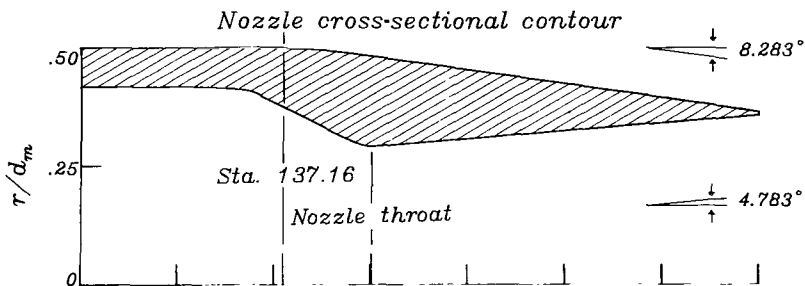
Nozzle external pressure distribution

Nozzle cross-sectional contour

Nozzle internal pressure distribution

$$x/d_m$$

(e) $M_\infty = 1.20$.

Figure 8.- Continued.

Nozzle external pressure distribution

$p_{t,j}/p_\infty$
⊕	J/0
⊞	1.53
◆	1.99
▲	2.52
◣	3.01
◳	3.99
⌂	4.99
●	5.99
◆	7.01
▲	8.01
●	8.93
■	9.95

Nozzle cross-sectional contour

Sta. 137.16

Nozzle throat

8.283°

4.783°
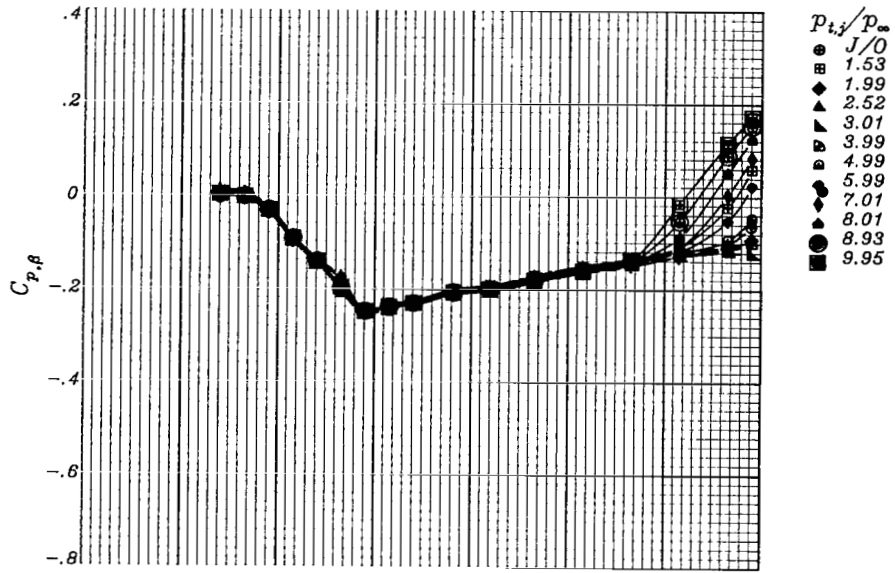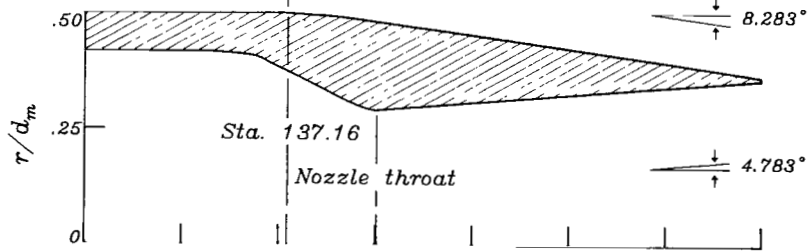
Nozzle internal pressure distribution
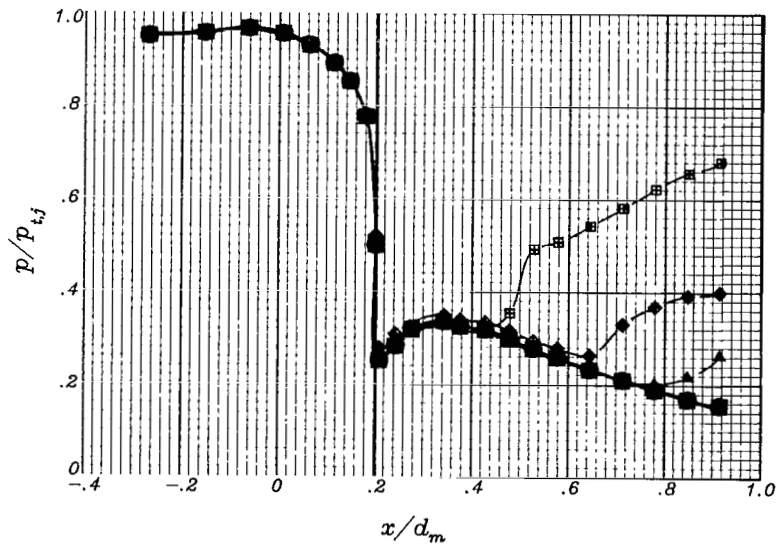
(f) $M_\infty = 1.27.$

Figure 8.- Concluded.

47

Nozzle external pressure distribution

Nozzle cross-sectional contour

Nozzle internal pressure distribution

$$(a) \quad M_\infty = 0.60.$$

Figure 9.- External and internal surface-pressure distributions of nozzle configuration 5. Origin is at start of boattail; location of throat is denoted by vertical line in nozzle cross-section contour; design nozzle pressure ratio is 10.64.

Nozzle external pressure distribution

$p_{t,j}/p_\infty$
- J/0
- 1.51
- 2.02
- 2.51
- 3.02
- 4.02
- 4.53
- 5.04
- 6.04
- 6.41

Nozzle cross-sectional contour

2.117°

Sta. 137.16

Nozzle throat

9.700°

Nozzle internal pressure distribution

x/d_m

(b) $M_\infty = 0.80.$

Figure 9.- Continued.

Nozzle external pressure distribution

$p_{t,j}/p_\infty$
- ⊕ $J/0$
- ⊞ 1.53
- ◈ 2.01
- ▲ 2.51
- ▶ 3.02
- ◣ 4.03
- ⊡ 5.03
- ● 6.03
- ◆ 6.94

Nozzle cross-sectional contour

$2.117°$

Sta. 137.16

Nozzle throat

$9.700°$

Nozzle internal pressure distribution

x/d_m

(c) $M_\infty = 0.90$.

Figure 9.- Continued.

Nozzle external pressure distribution

$p_{t,j}/p_\infty$

- ● J/0
- ▣ 1.51
- ◆ 2.01
- ▲ 2.54
- ◤ 3.01
- ◪ 4.02
- ◓ 5.04
- ● 6.04
- ◆ 7.04

Nozzle cross-sectional contour

2.117°

Sta. 137.16

Nozzle throat

9.700°
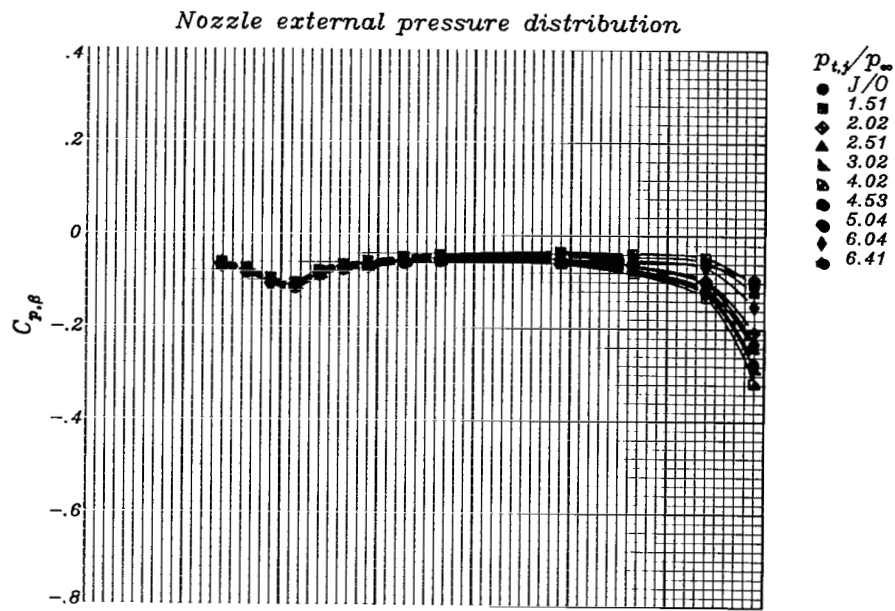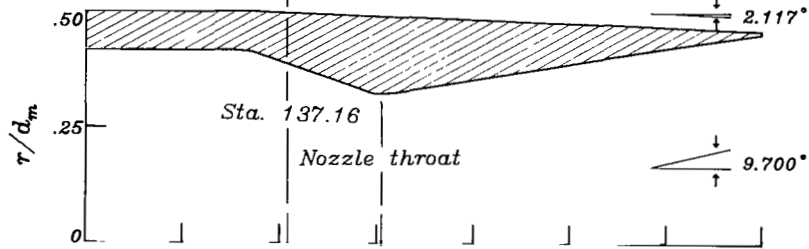
Nozzle internal pressure distribution

(d) $M_\infty = 0.94.$

Figure 9.- Continued.

Nozzle external pressure distribution

$p_{t,j}/p_\infty$	
⊕	$J/0$
⊞	1.54
◆	2.03
▲	2.54
◣	3.09
◪	4.08
⬣	5.07
◆	6.09
◆	7.09
▲	8.12
◉	9.11
▣	9.51

$C_{p,\beta}$

Nozzle cross-sectional contour

r/d_m

2.117°

Sta. 137.16

Nozzle throat

9.700°

Nozzle internal pressure distribution

$p/p_{t,j}$

x/d_m

(e) $M_\infty = 1.20.$

Figure 9.- Continued.

52

Nozzle external pressure distribution

$p_{t,j}/p_\infty$	
⊕	J/0
⊞	1.53
◈	2.03
▲	2.51
◤	3.03
◩	4.00
⌂	5.05
●	6.01
◆	7.04
▲	7.99
◉	8.96
▦	9.97

Nozzle cross-sectional contour

Sta. 137.16

Nozzle throat

2.117°

9.700°

Nozzle internal pressure distribution

x/d_m

(f) M_∞ = 1.27.

Figure 9.- Concluded.

Figure 10.- Variation of jet-off, boattail pressure-drag coefficient with free-stream Mach number.
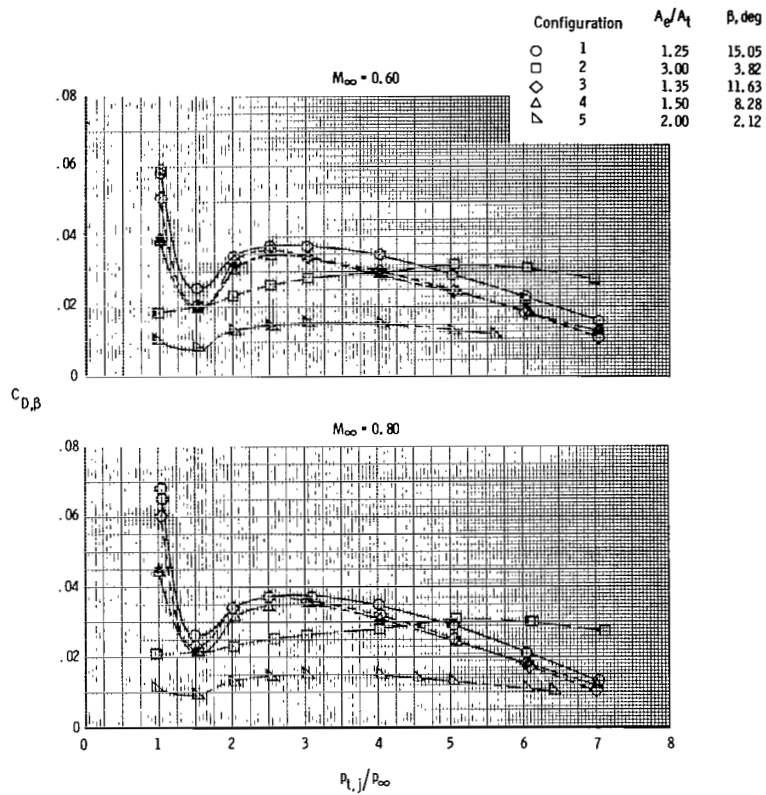
(a) M_∞ = 0.60 and 0.80.

Figure 11.- Influence of nozzle pressure ratio on
boattail pressure-drag coefficient.

Configuration	A_e/A_t	β, deg
○ 1	1.25	15.05
□ 2	3.00	3.82
◇ 3	1.35	11.63
△ 4	1.50	8.28
◁ 5	2.00	2.12

(b) $M_\infty = 0.90$ and 0.94.

Figure 11.- Continued.

Configuration	A_e/A_t	β, deg
○ 1	1.25	15.05
□ 2	3.00	3.82
◇ 3	1.35	11.63
△ 4	1.50	8.28
△ 5	2.00	2.12
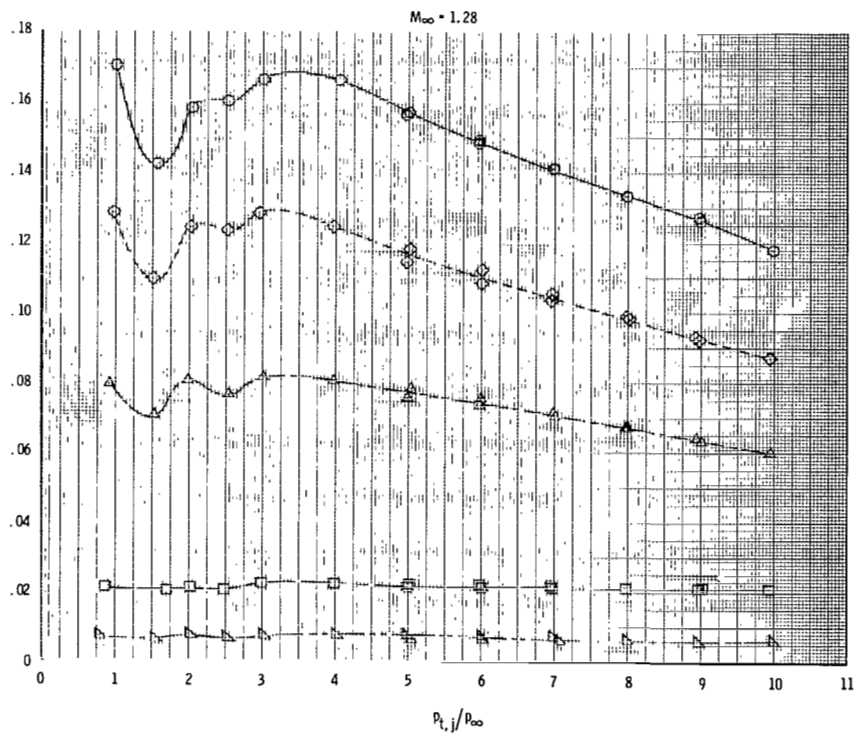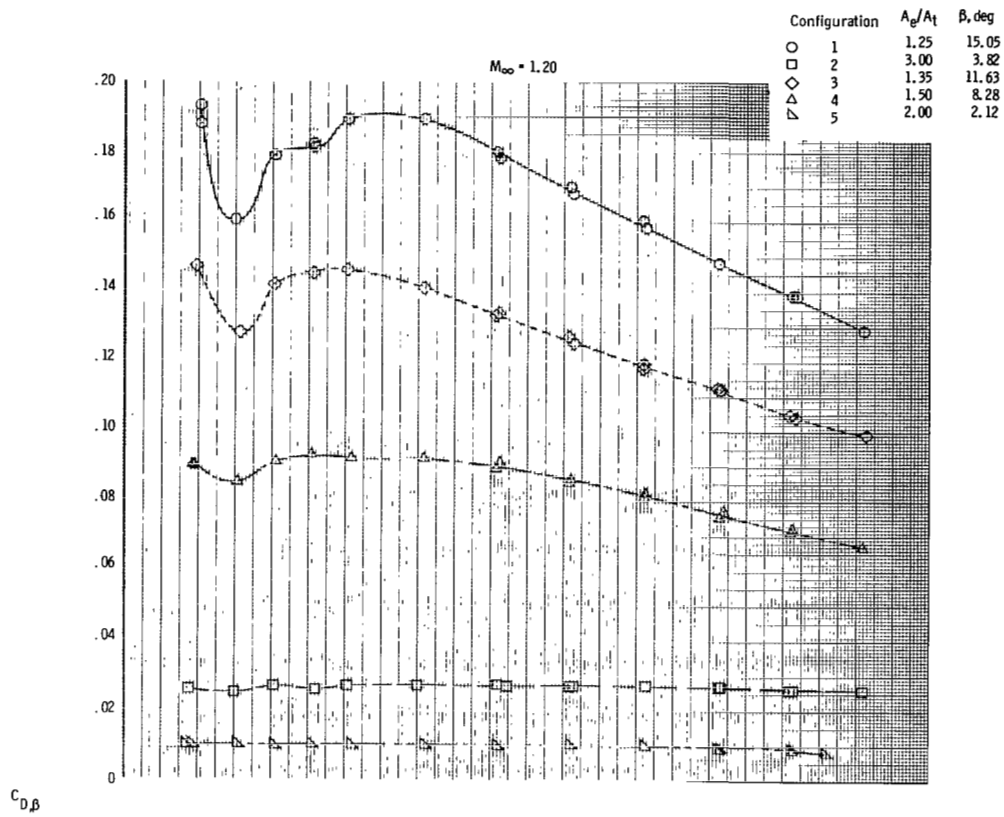
(c) M_∞ = 1.20 and 1.28.

Figure 11.- Concluded.
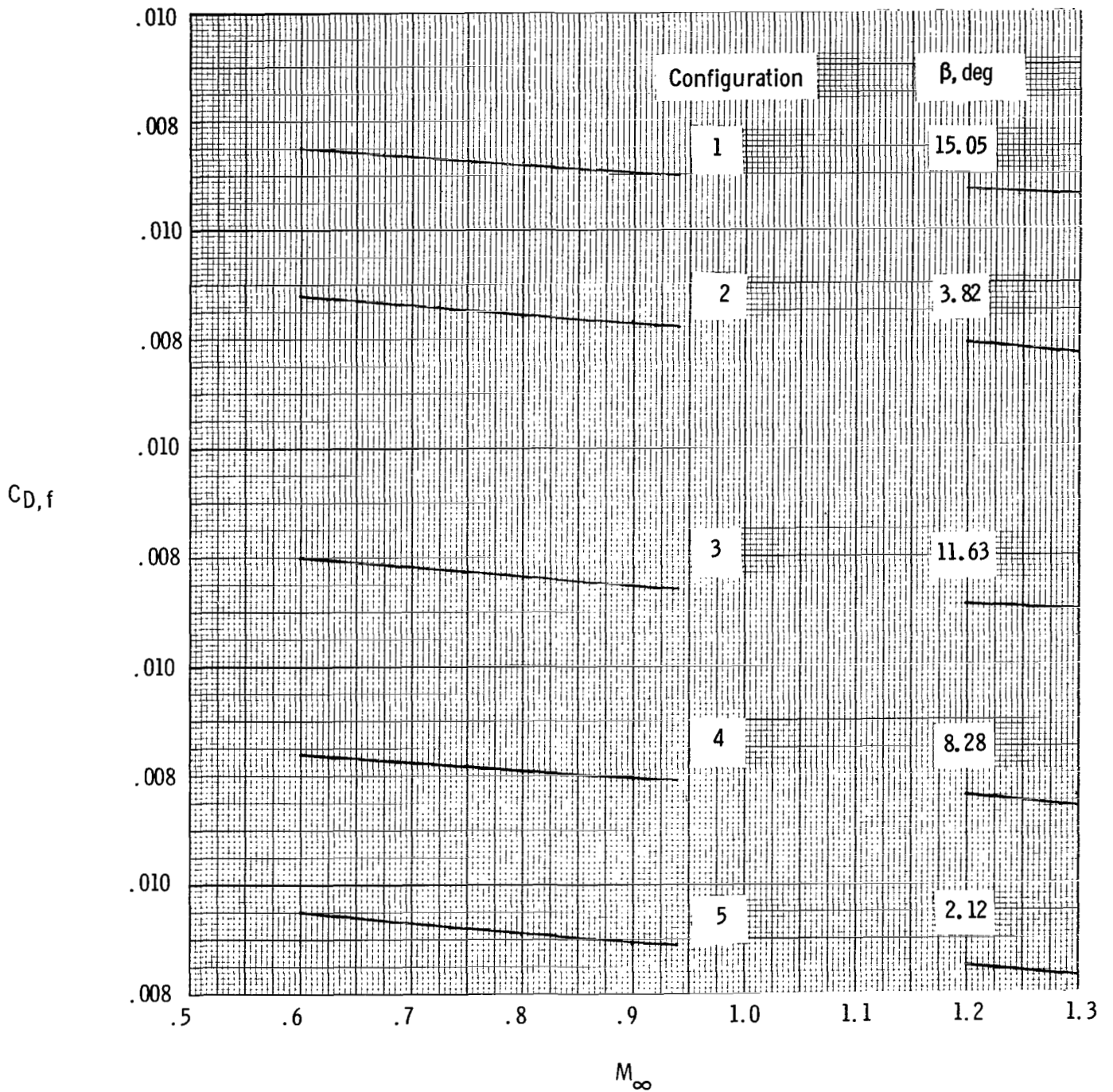
Figure 12.- Calculated skin-friction drag of the various boattails from
station 137.16 cm to the exit.
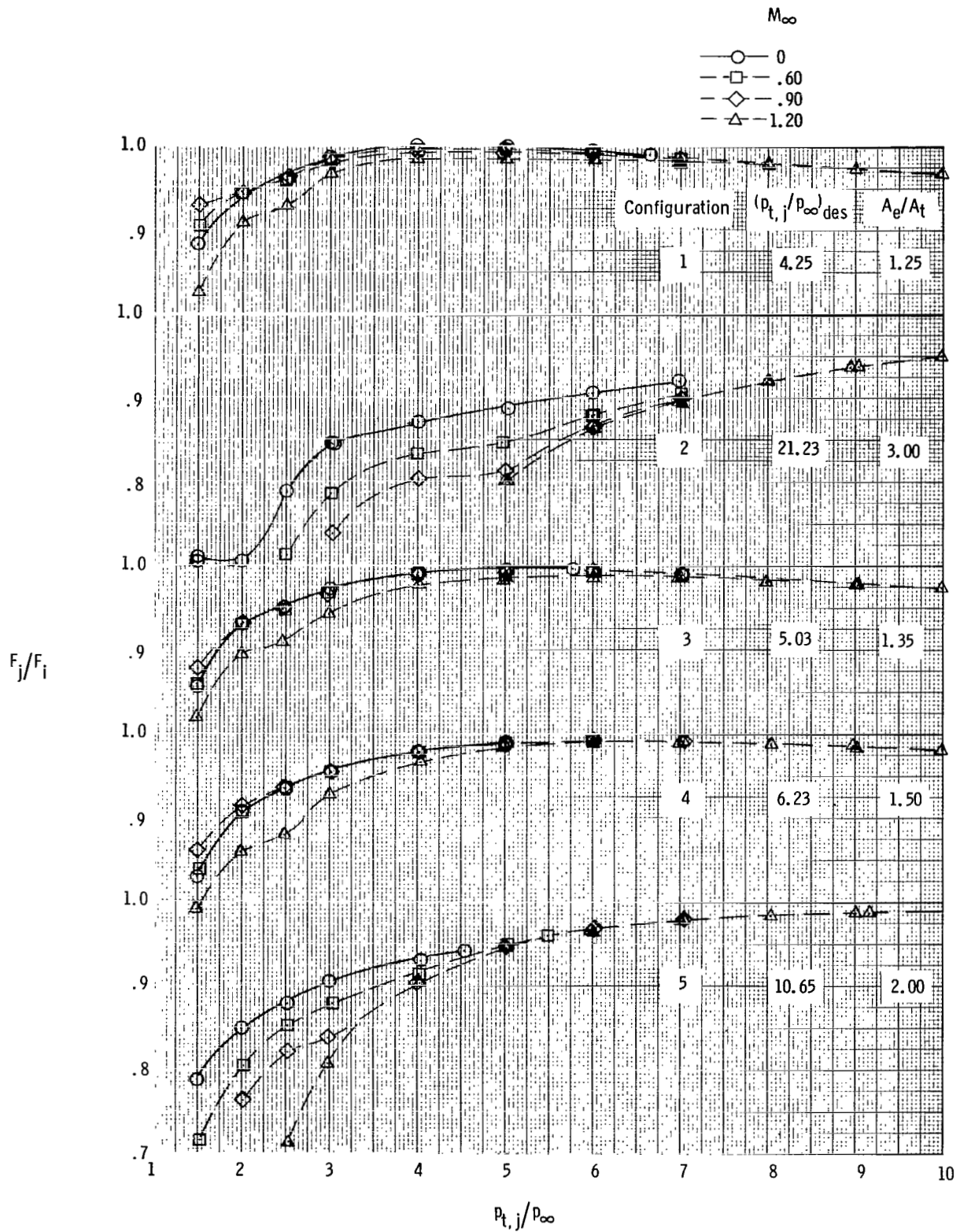
Figure 13.- Nozzle internal performance at static and wind-on conditions.
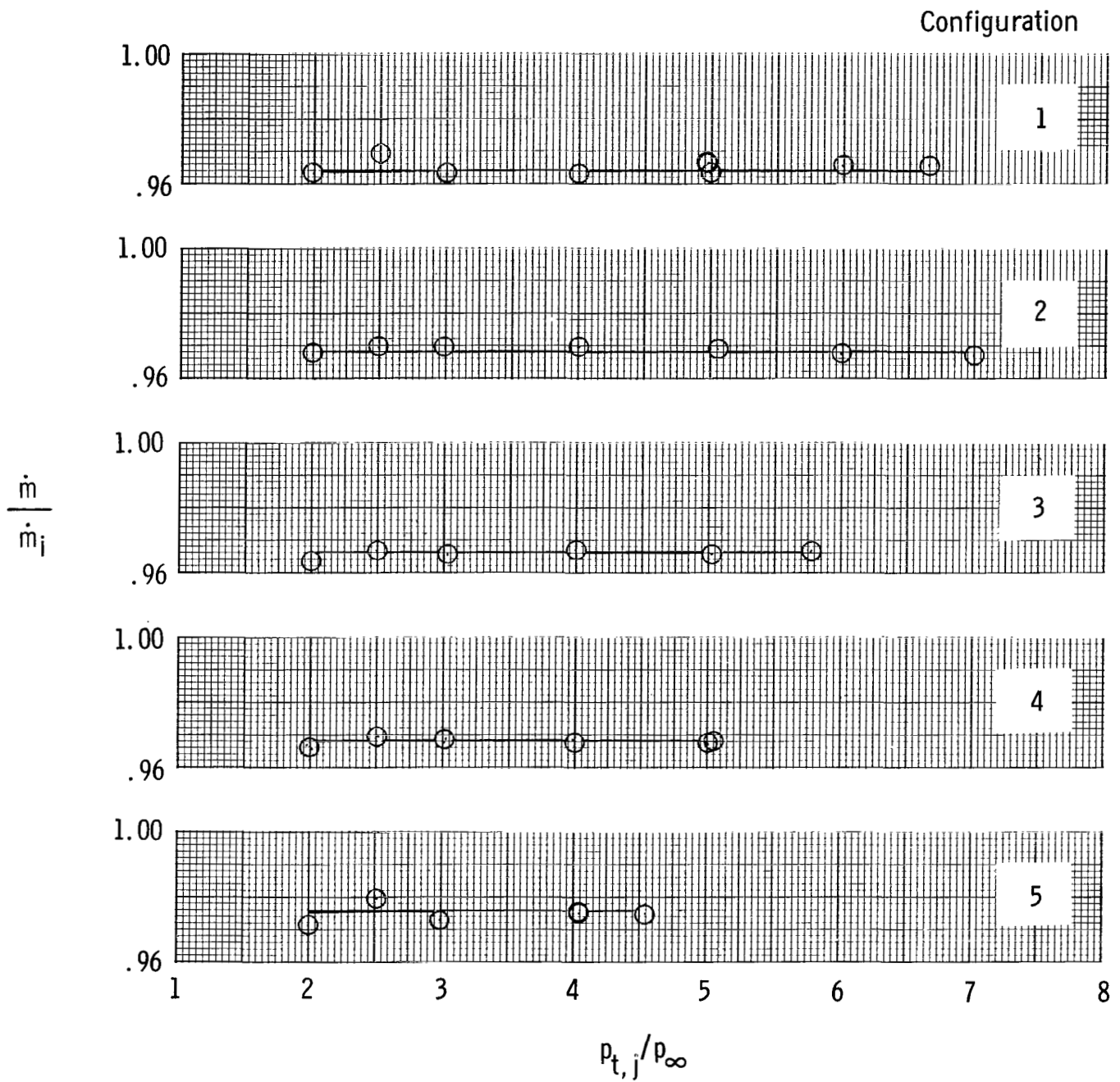
Figure 14.- Static discharge coefficients of the nozzles.

$M_\infty = 0.60$

Configuration	$(p_{t,j}/p_\infty)_{des}$	A_e/A_t	β, deg.
◯ 1	4.25	1.25	15.05
◻ 2	21.23	3.00	3.82
◇ 3	5.03	1.35	11.63
△ 4	6.23	1.50	8.28
◹ 5	10.65	2.00	2.12

$$\frac{F_j - D_n}{F_i}$$

$M_\infty = 0.80$

$$p_{t,j}/p_\infty$$
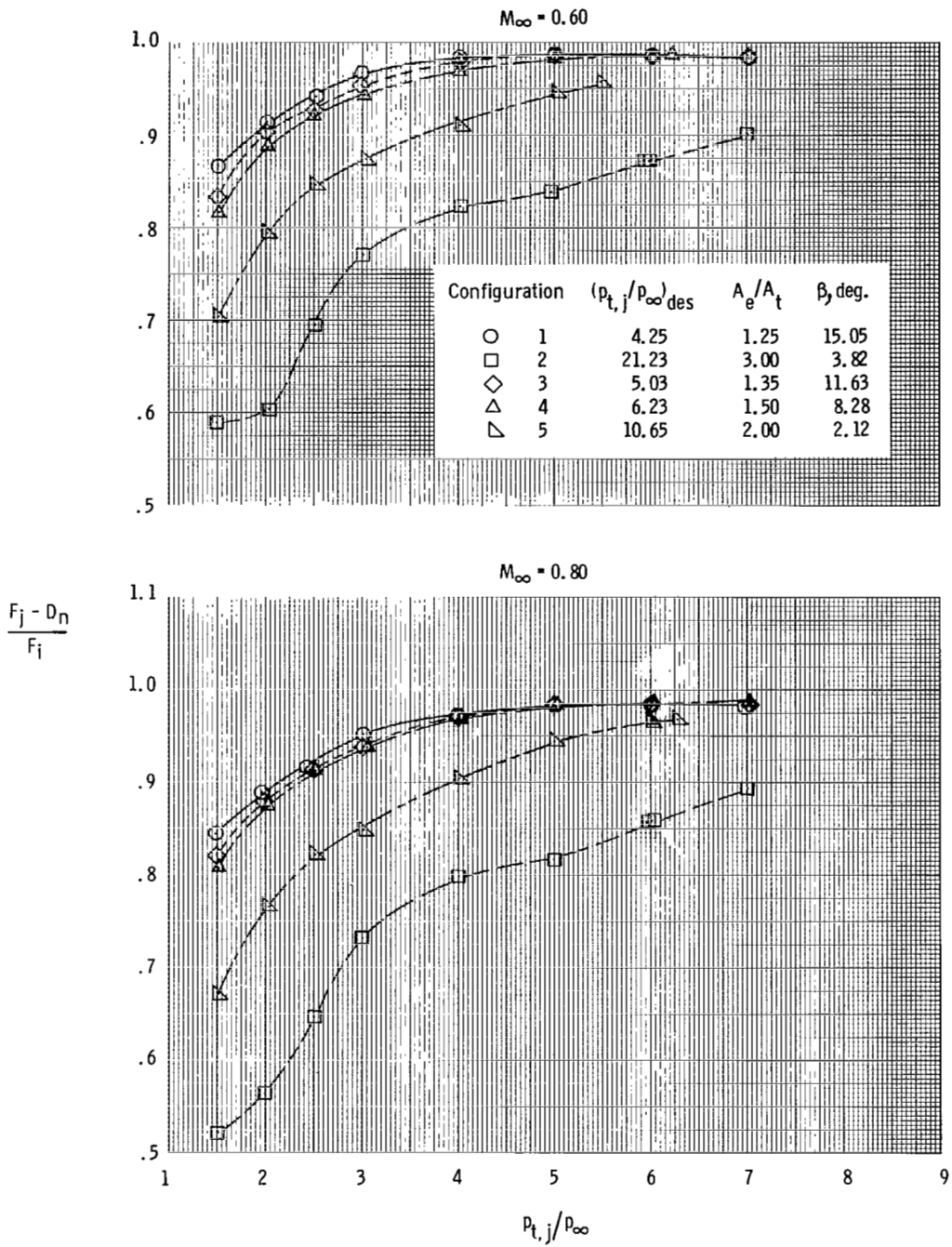
(a) M_∞ = 0.60 and 0.80.

Figure 15.- Measured thrust-minus-drag performance of all
nozzle-boattail combinations.

61

$M_\infty = 0.90$

$M_\infty = 0.94$

$\dfrac{F_j - D_n}{F_i}$

$p_{t,j}/p_\infty$

Configuration	$(p_{t,j}/p_\infty)_{des}$	A_e/A_t	β, deg
○ 1	4.25	1.25	15.05
□ 2	21.23	3.00	3.82
◇ 3	5.03	1.35	11.63
△ 4	6.23	1.50	8.28
◁ 5	10.65	2.00	2.12
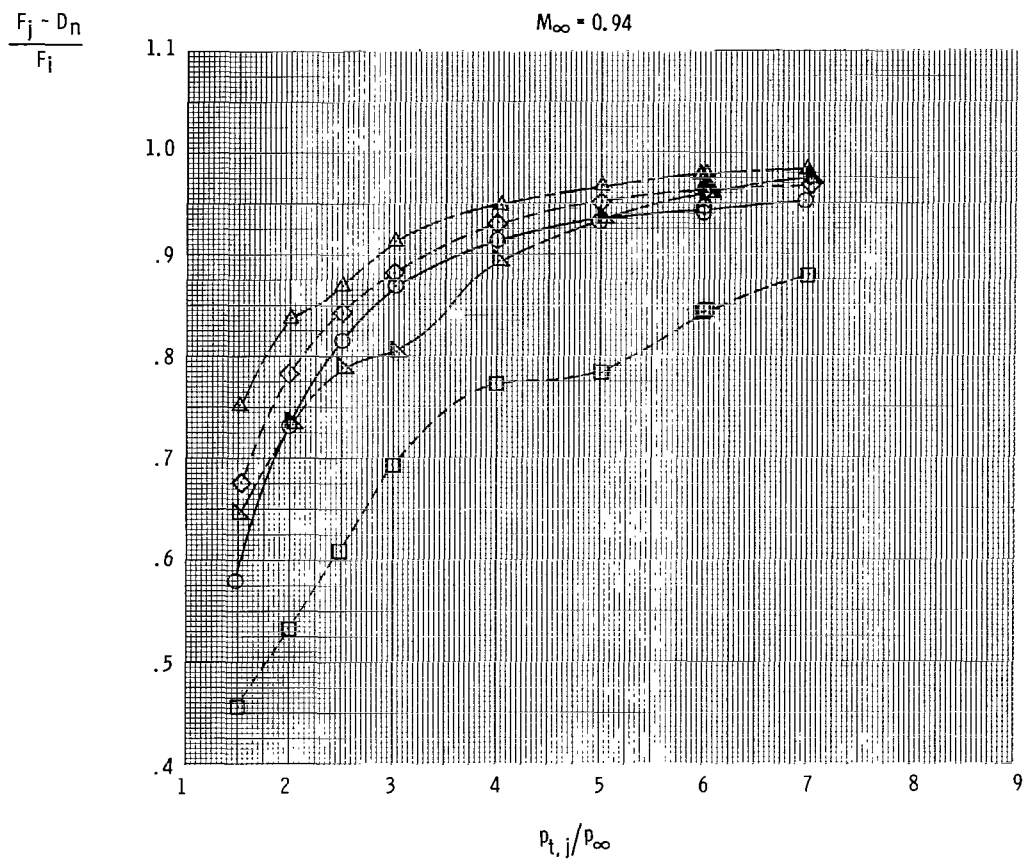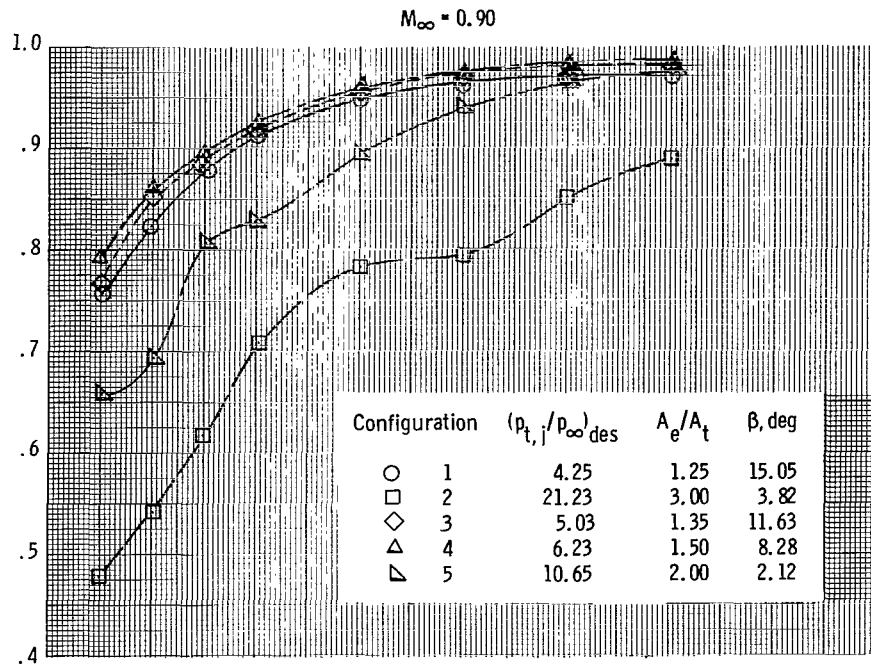
(b) $M_\infty = 0.90$ and 0.94.

Figure 15.- Continued.

Configuration	$(p_{t,j}/p_\infty)_{des}$	A_e/A_t	β, deg
◯ 1	4.25	1.25	15.05
□ 2	21.23	3.00	3.82
◇ 3	5.03	1.35	11.63
△ 4	6.23	1.50	8.28
◁ 5	10.65	2.00	2.12

$\dfrac{F_j - D_n}{F_j}$

$p_{t,j}/p_\infty$

(c) $M_\infty = 1.20$.

Figure 15.- Continued.

$M_\infty = 1.30$

Configuration	$(p_{t,j}/p_\infty)_{des}$	A_e/A_t	β, deg
○ 1	4.25	1.25	15.05
□ 2	21.23	3.00	3.82
◇ 3	5.03	1.35	11.63
△ 4	6.23	1.50	8.28
◁ 5	10.65	2.00	2.12
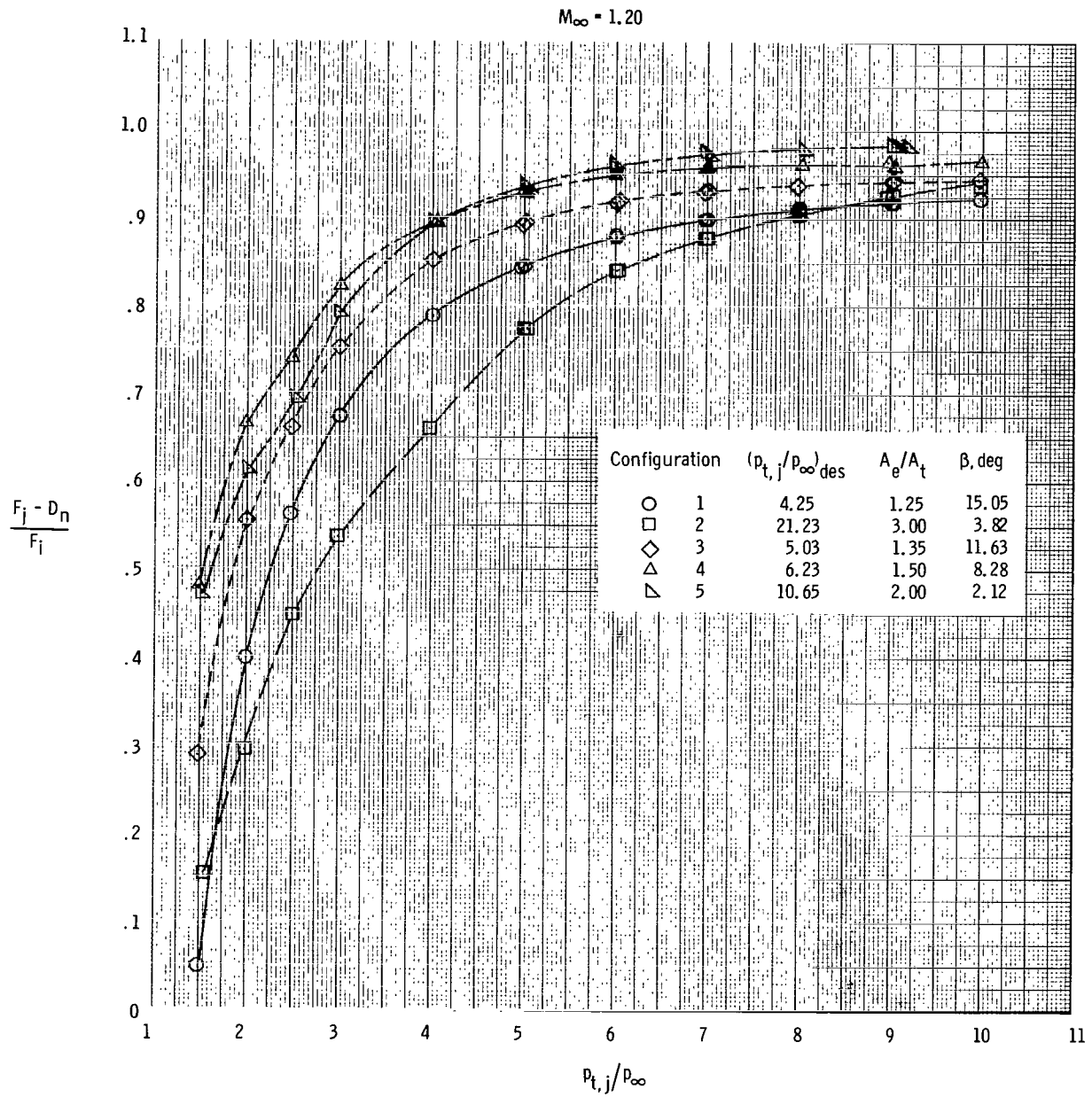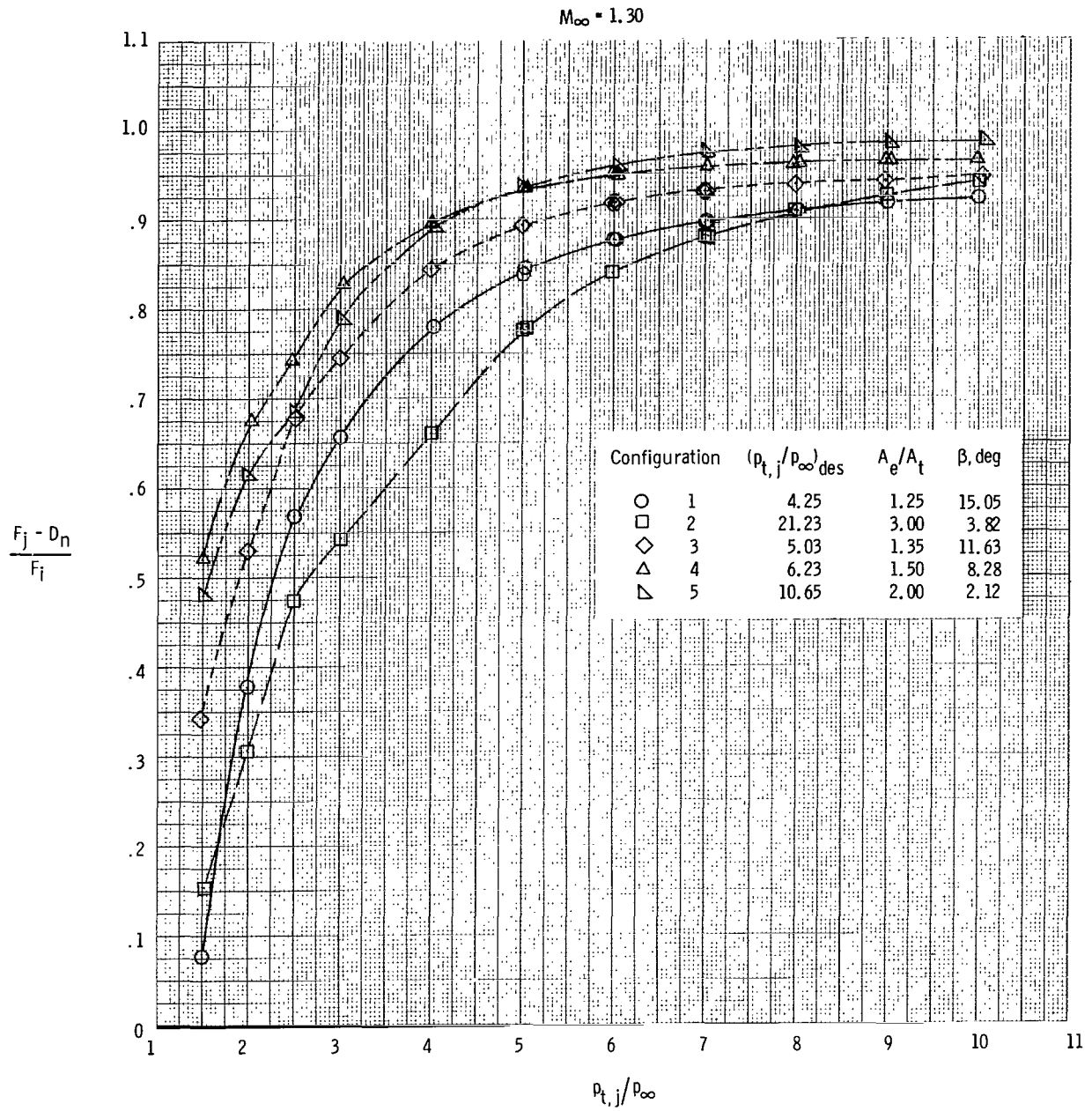
(d) $M_\infty = 1.30$.

Figure 15.- Concluded.
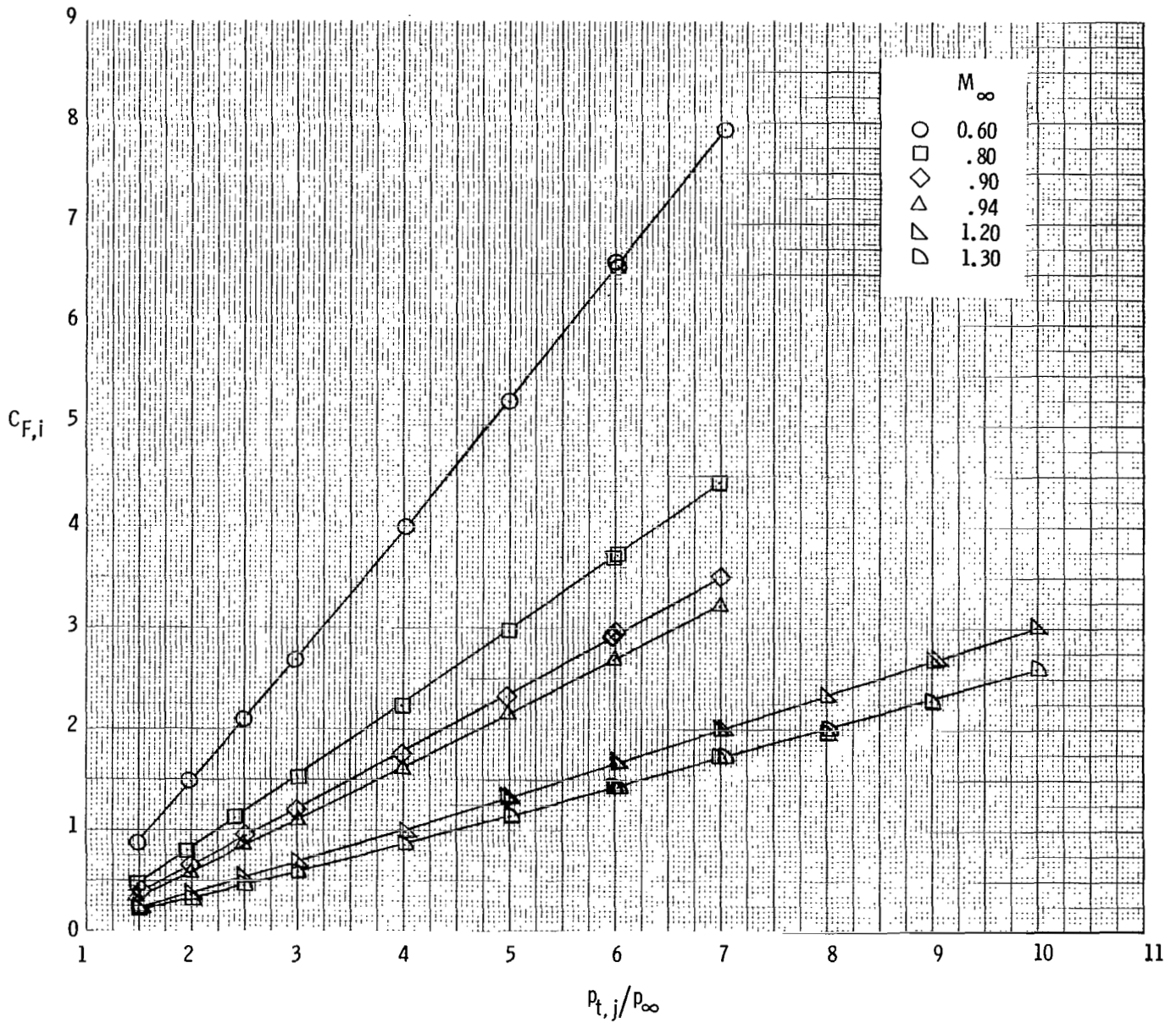
(a) Configurations 1 and 2. $A_t/A_m = 0.25$.

Figure 16.- Aerodynamic ideal thrust coefficient as a function of jet total-pressure ratio.
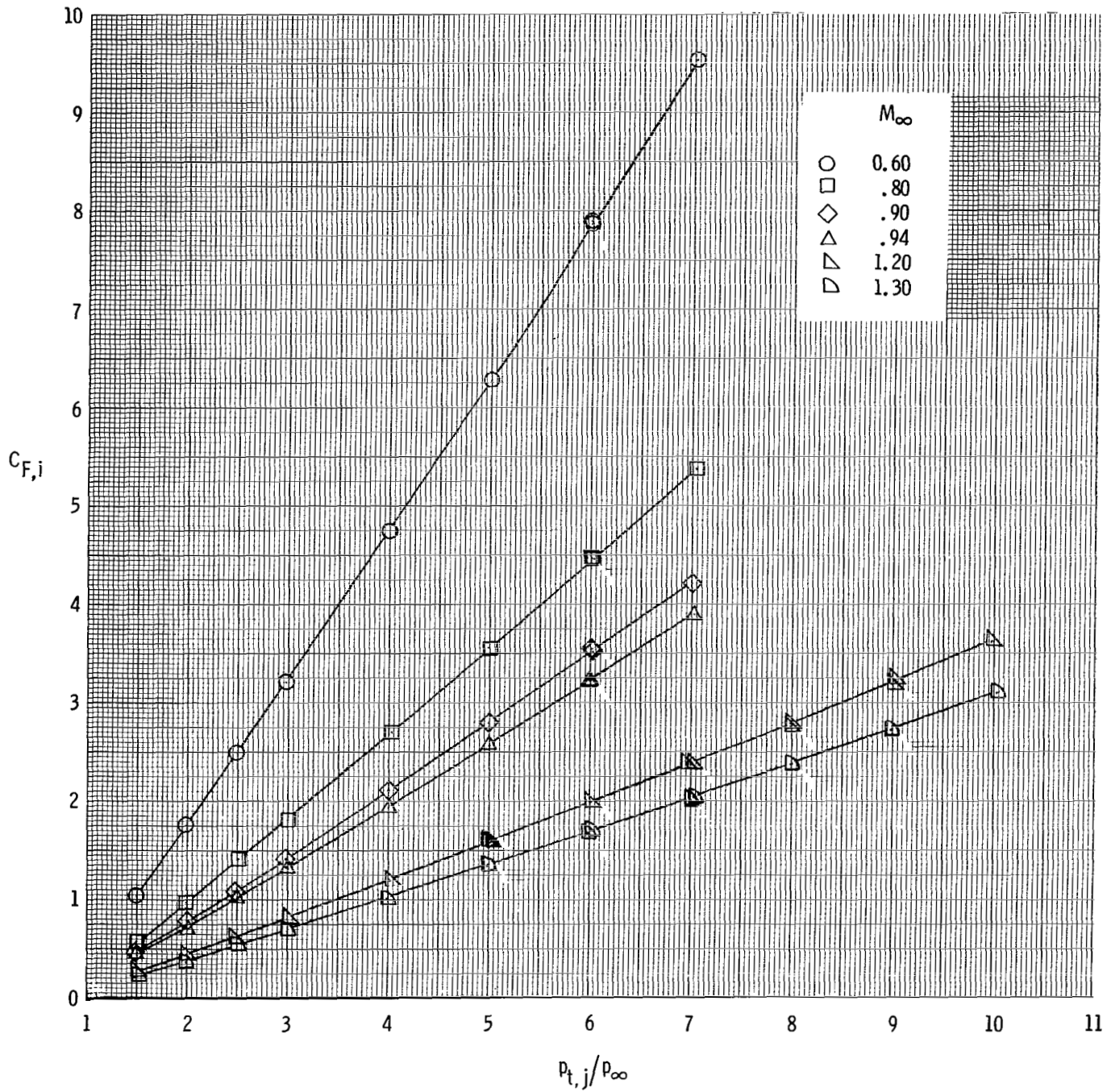
(b) Configuration 3. $A_t/A_m = 0.30$.

Figure 16.- Continued.
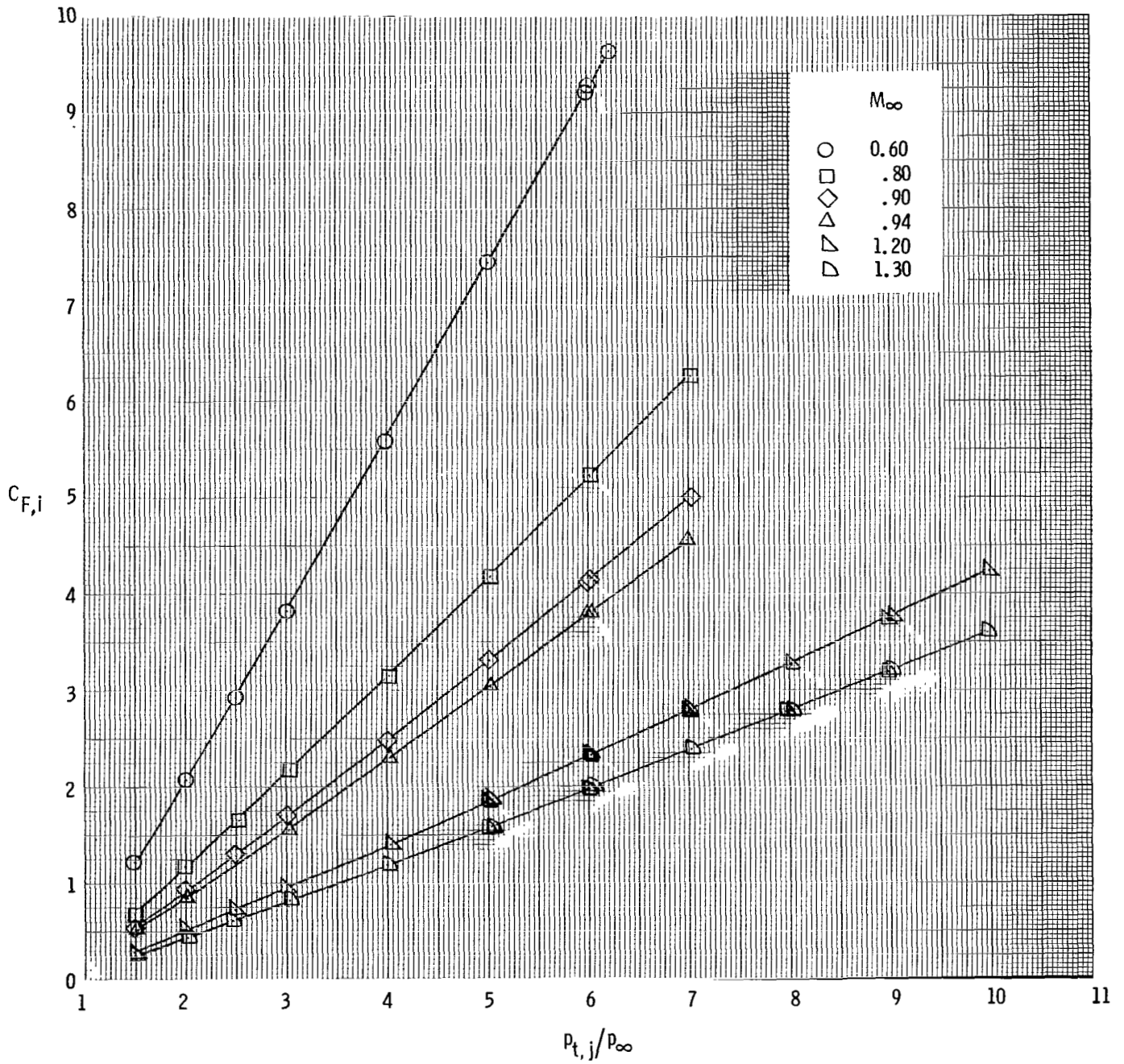
(c) Configuration 4. $A_t/A_m = 0.35$.

Figure 16.- Continued.
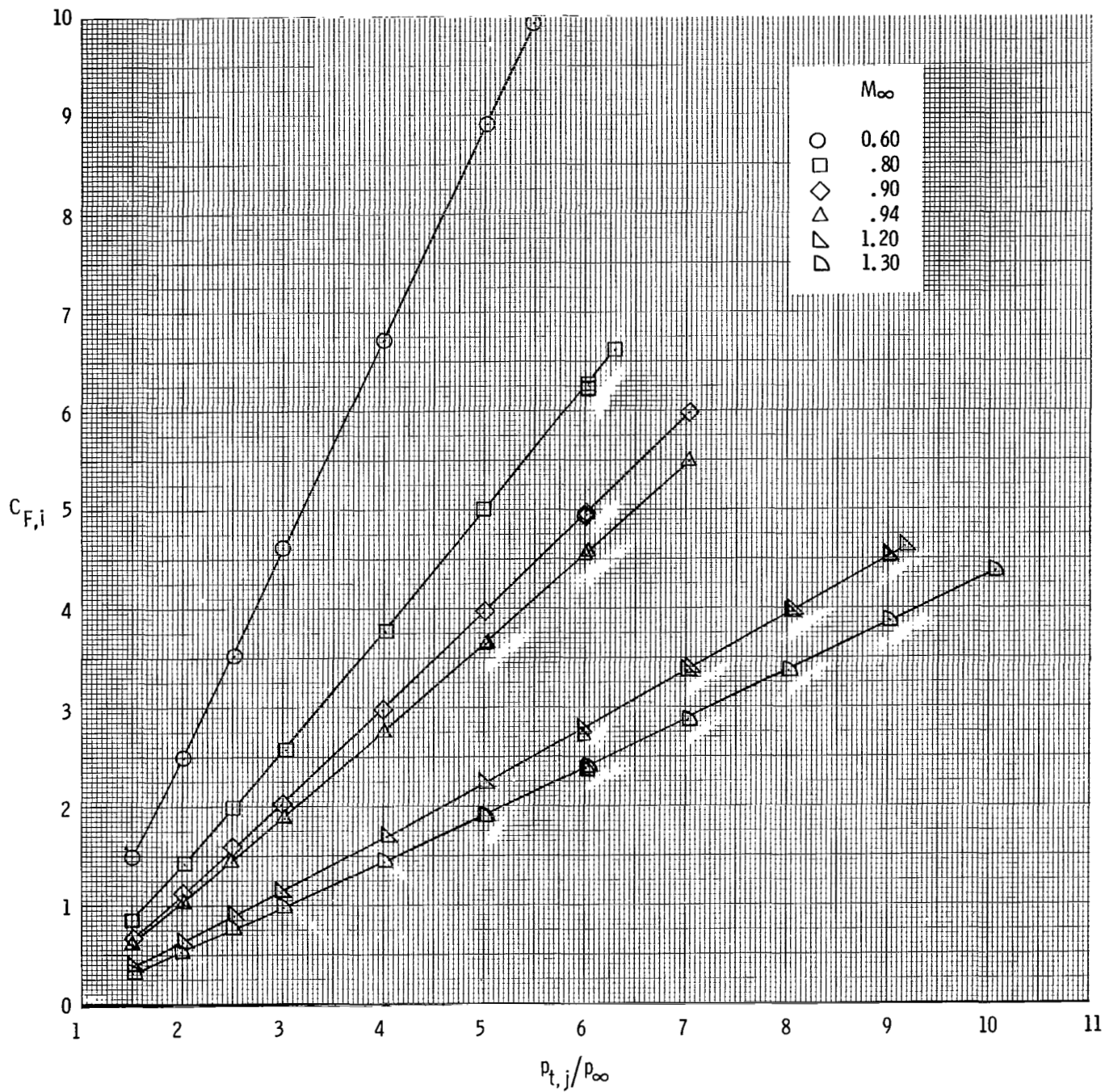
(d) Configuration 5. $A_t/A_m = 0.42$.

Figure 16.- Concluded.
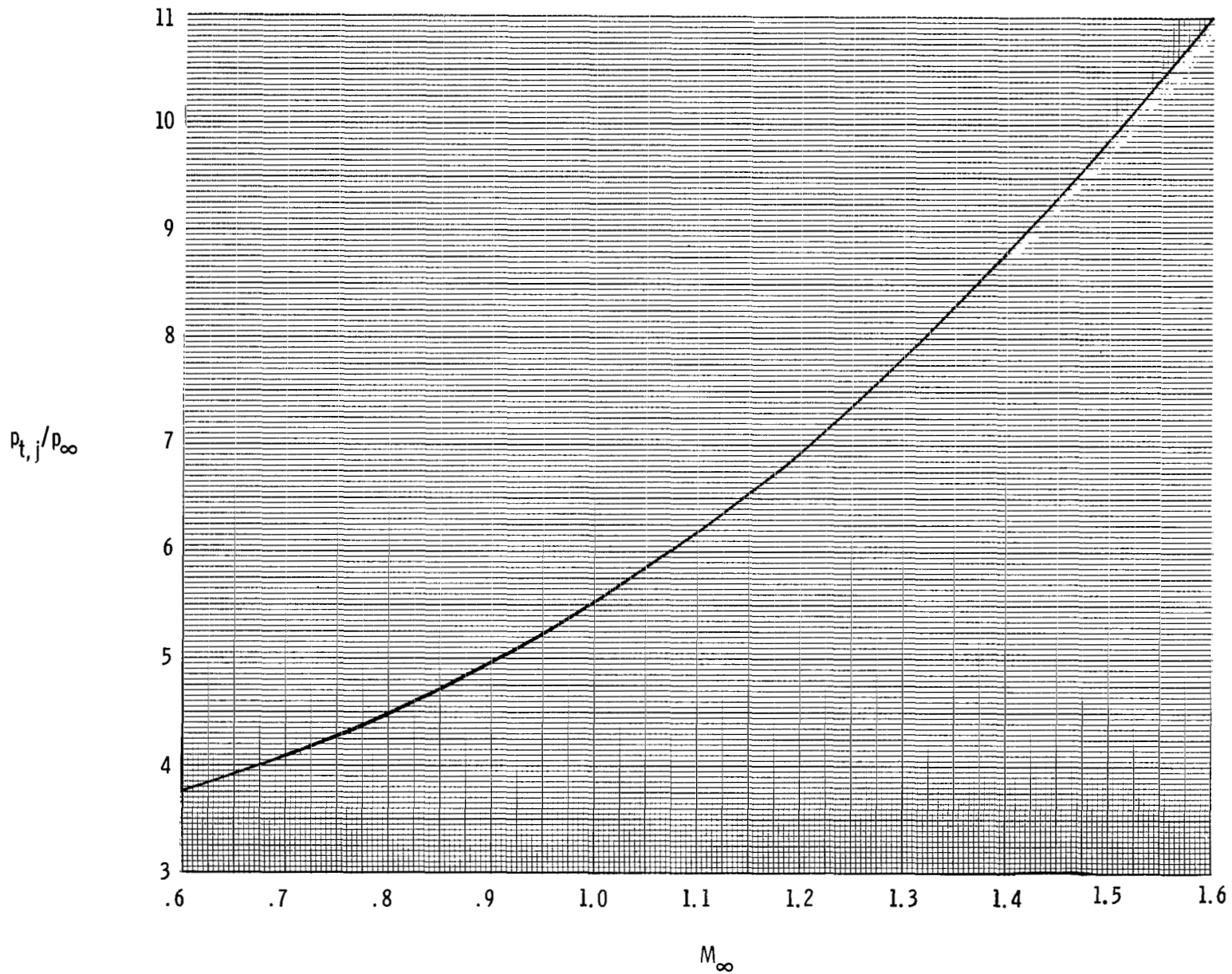
Figure 17.- Representative schedule of nozzle pressure ratio with Mach number for an advanced low-bypass-ratio turbofan engine at maximum rotational speed.

Configuration	Power setting	$(p_{t,j}/p_\infty)_{des}$	A_e/A_t	A_t/A_m	β, deg
1	Dry	4.25	1.25	0.25	15.05
3	Maximum Dry	5.03	1.35	.30	11.63
4	Partial A/B	6.23	1.50	.35	8.28
5	Maximum A/B	10.64	2.00	.42	2.12
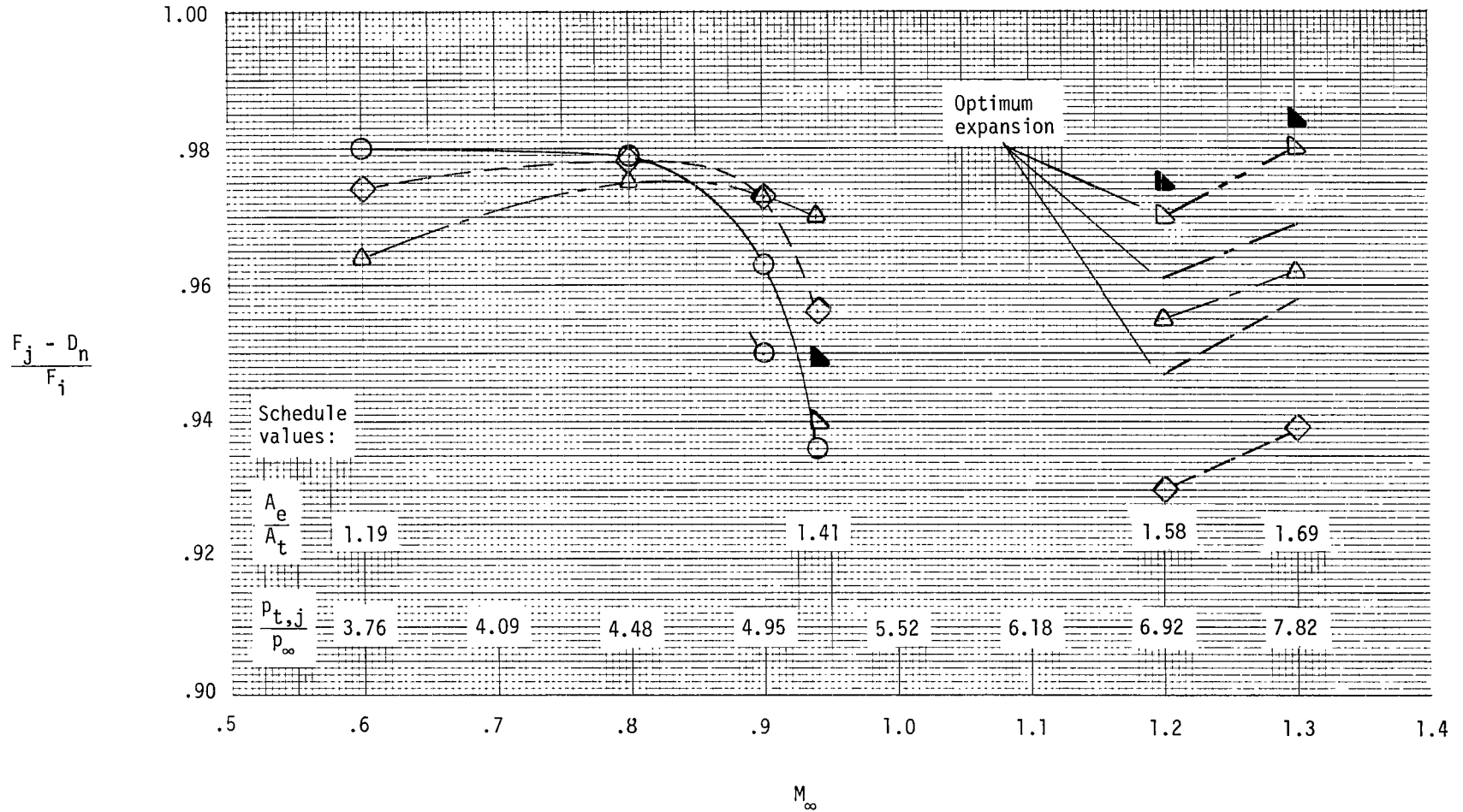
Figure 18.- Summary of nozzle-boattail overall performance for the pressure-ratio schedule of figure 17. Solid symbols indicate internal gross-to-ideal thrust ratios; flagged symbol denotes assumed subsonic cruise point at $M_\infty = 0.90$; $p_{t,j}/p_\infty = 4.0$.
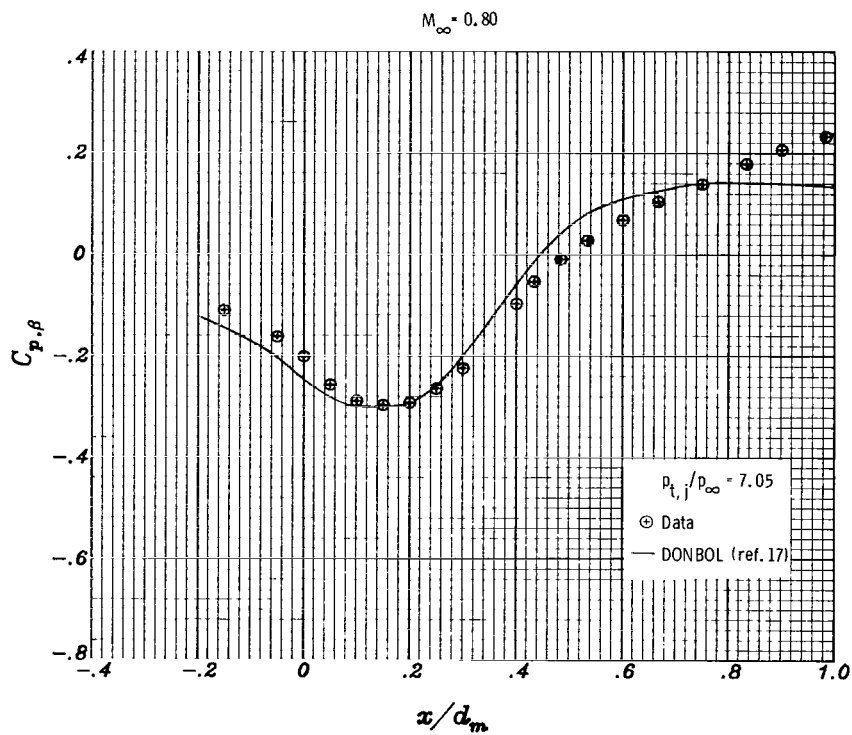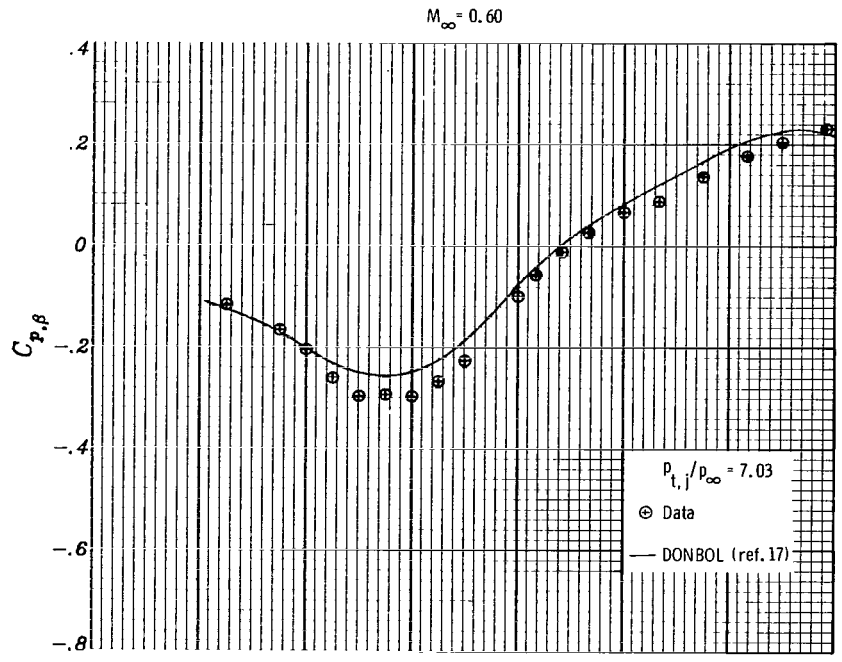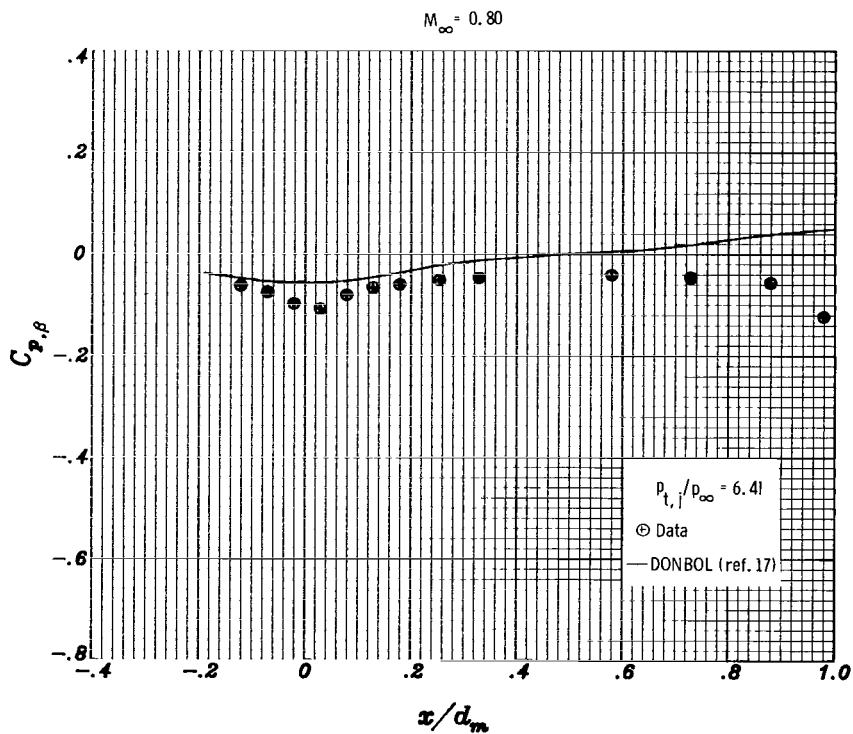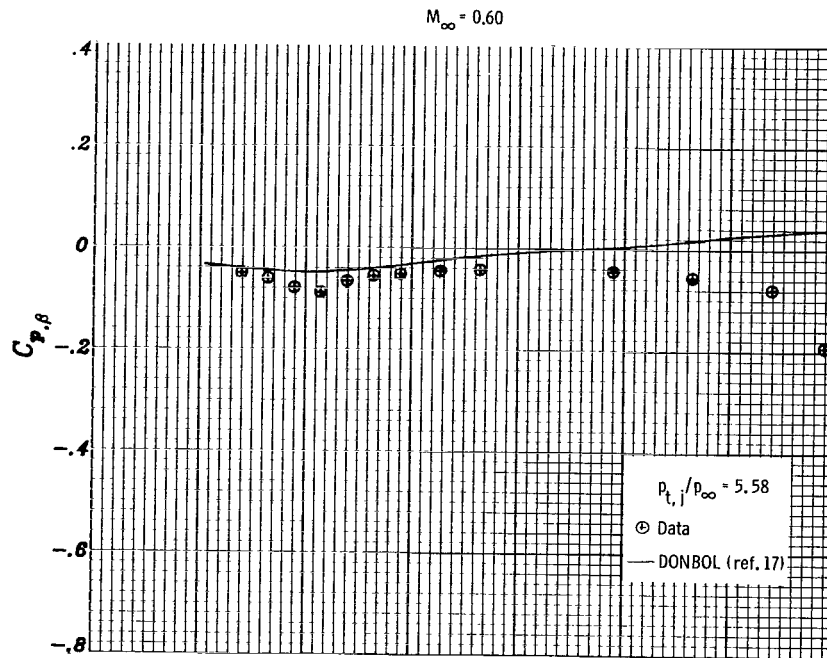
(a) M_∞ = 0.60 and 0.80.

Figure 19.- Comparison of experimentally and analytically
determined external pressure distributions for nozzle
configuration 1. Boattail angle is 15.05°; design nozzle
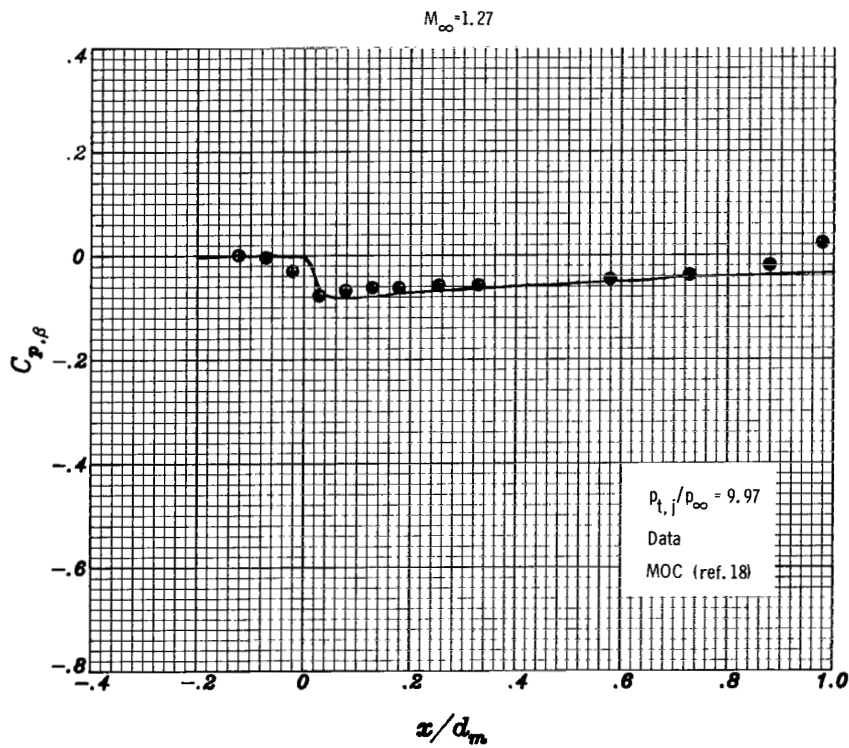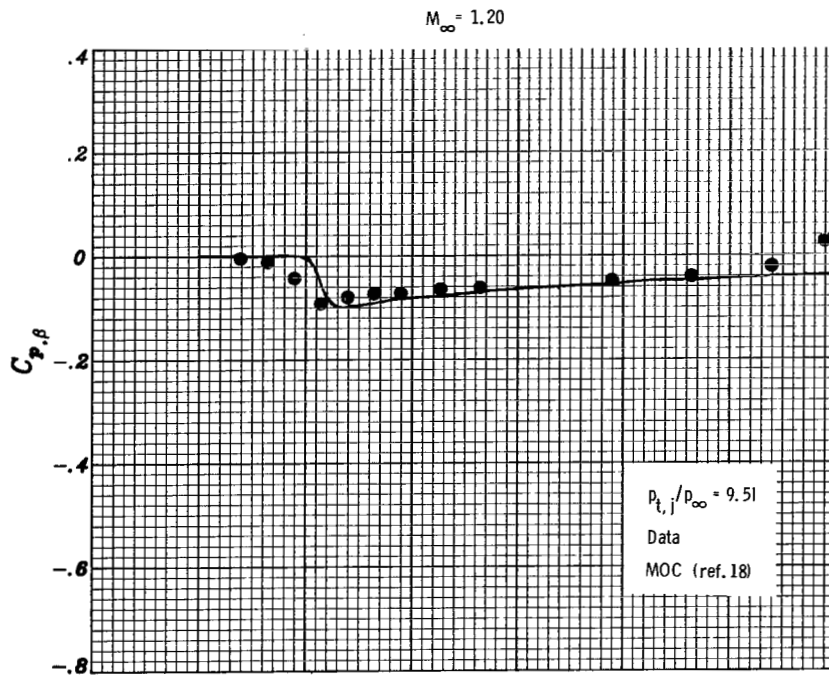pressure ratio is 4.25.
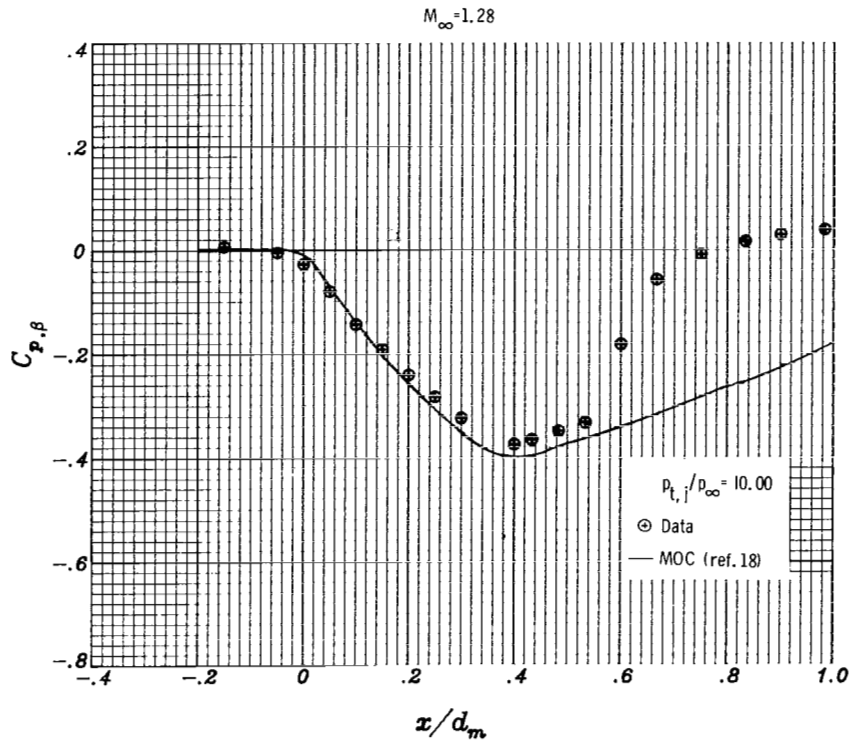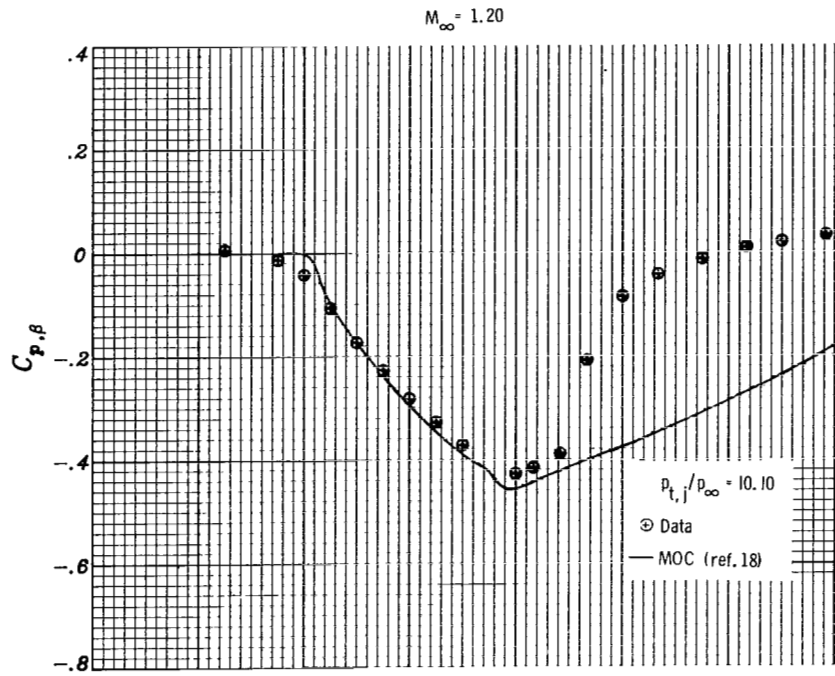
(b) $M_\infty = 1.20$ and 1.28.
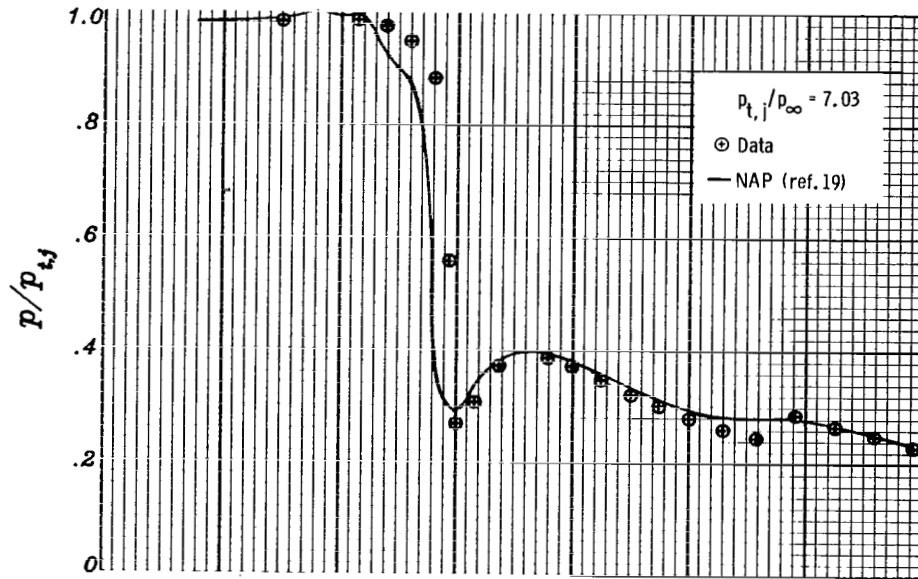
Figure 19.- Concluded.
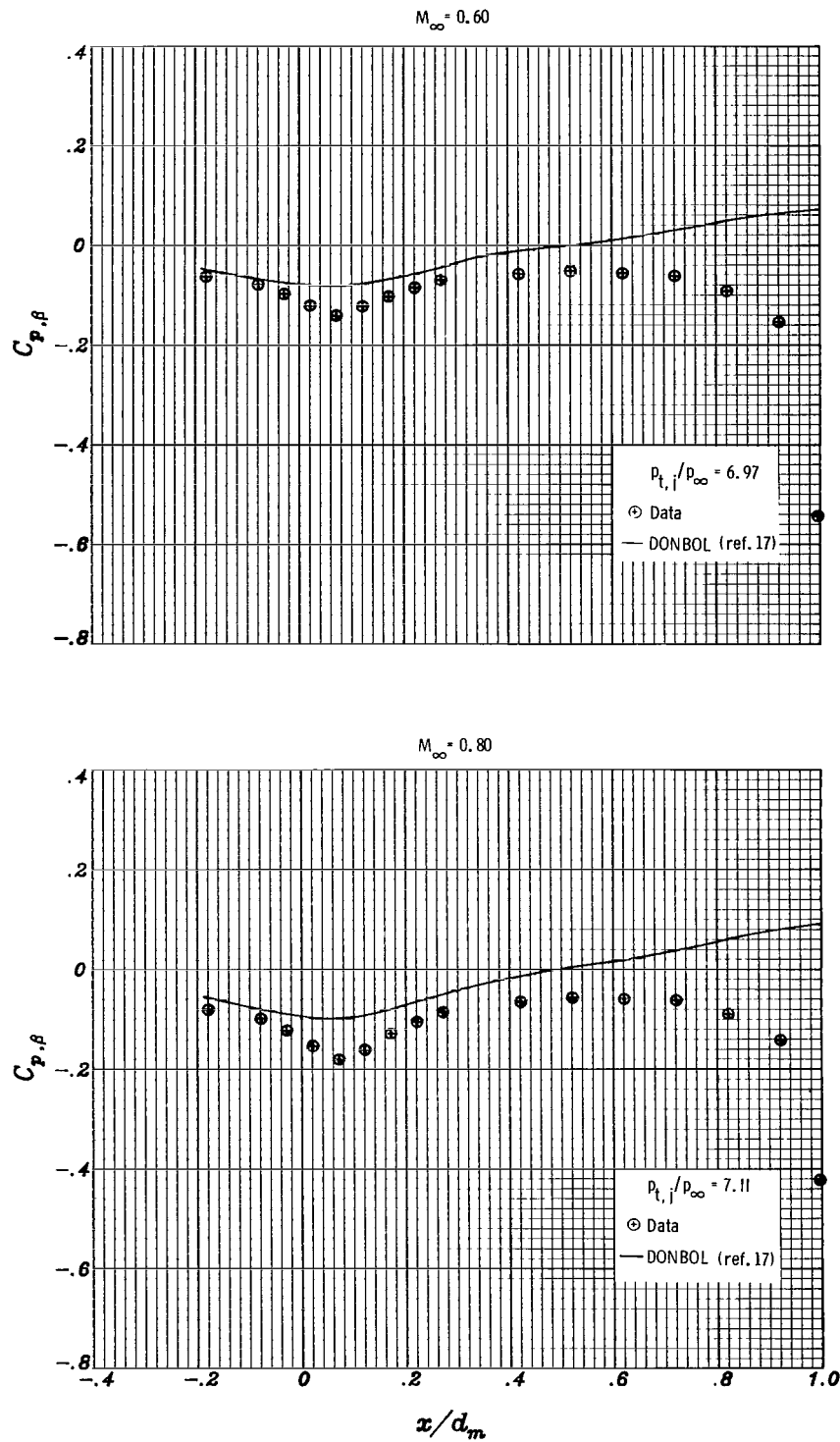
(a) M_∞ = 0.60 and 0.80.

Figure 20.- Comparison of experimentally and analytically
determined external pressure distributions for nozzle
configuration 2. Boattail angle is 3.82°; design nozzle
pressure ratio is 21.23.
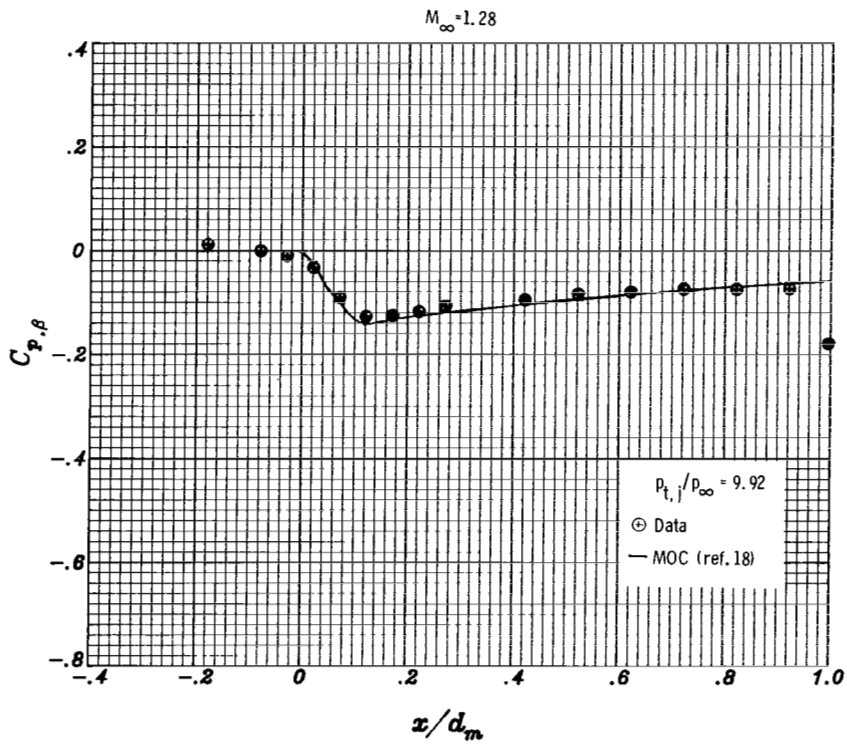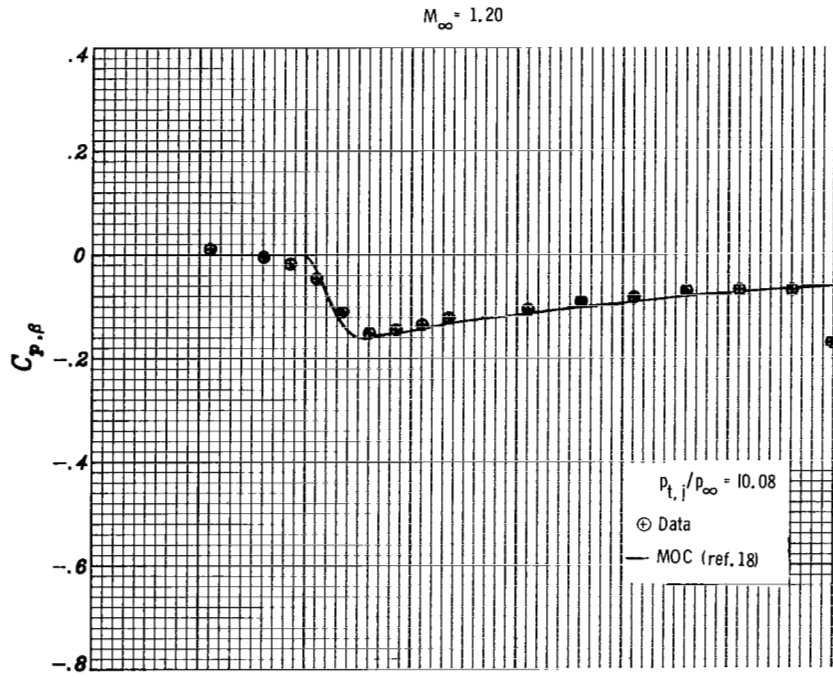
(b) $M_\infty = 1.20$ and 1.28.

Figure 20.- Concluded.
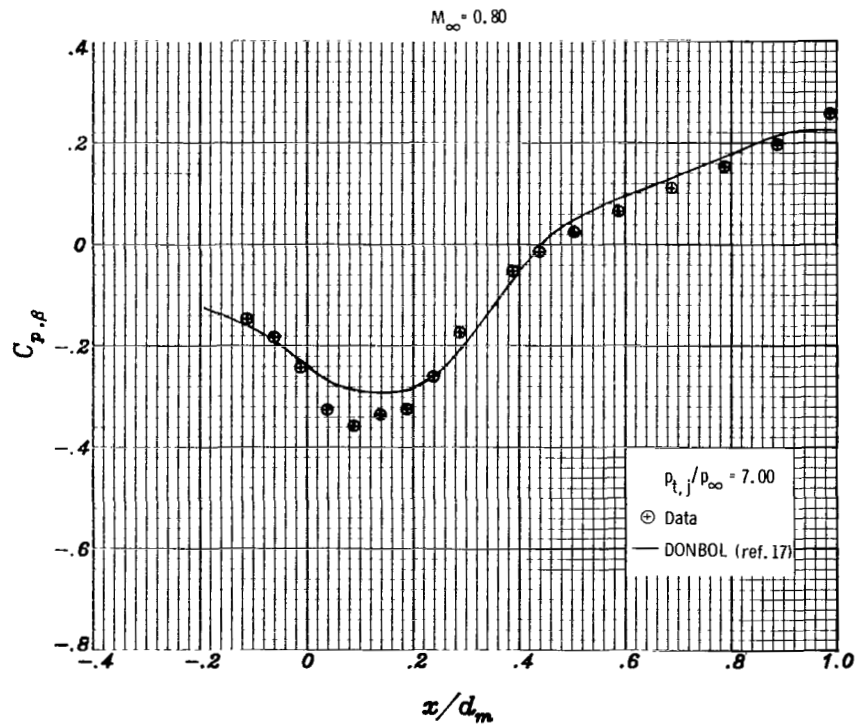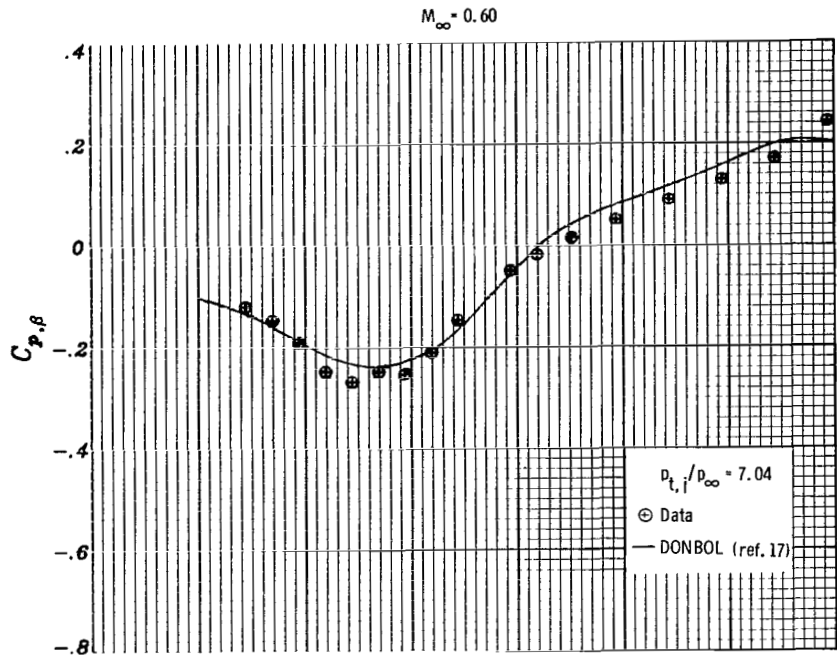
(a) $M_\infty = 0.60$ and 0.80.

Figure 21.- Comparison of experimentally and analytically
determined external pressure distributions for nozzle
configuration 3.   Boattail angle is 11.83°; design
nozzle pressure ratio is 5.03.
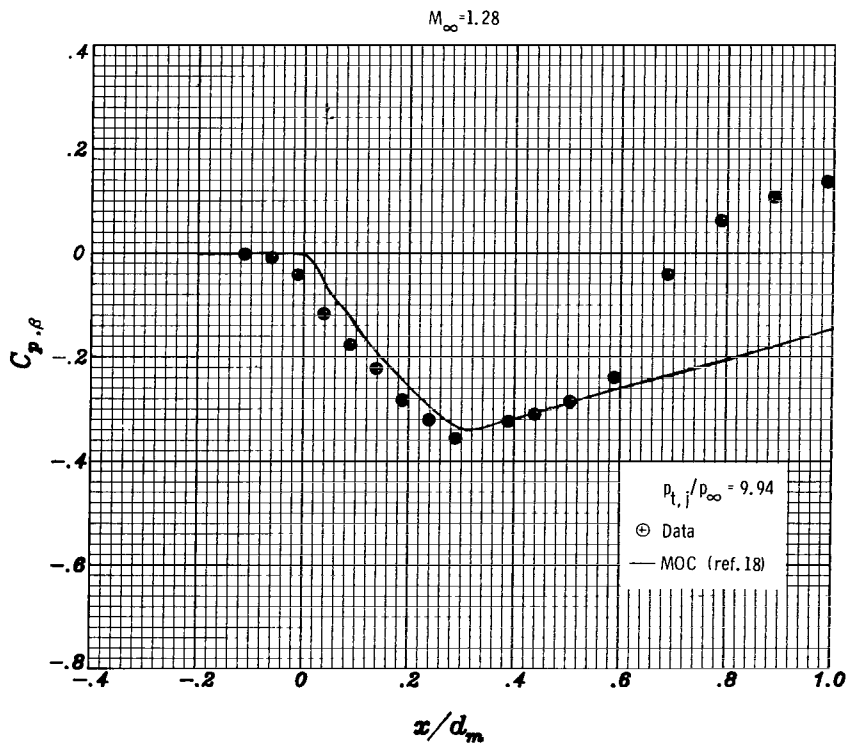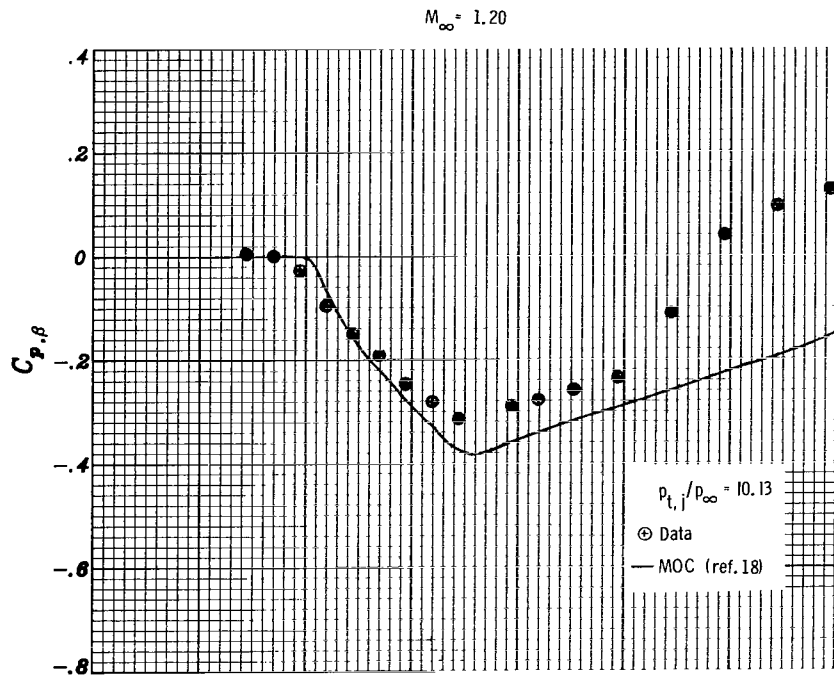
(b) M_∞ = 1.20 and 1.28.

Figure 21.- Concluded.
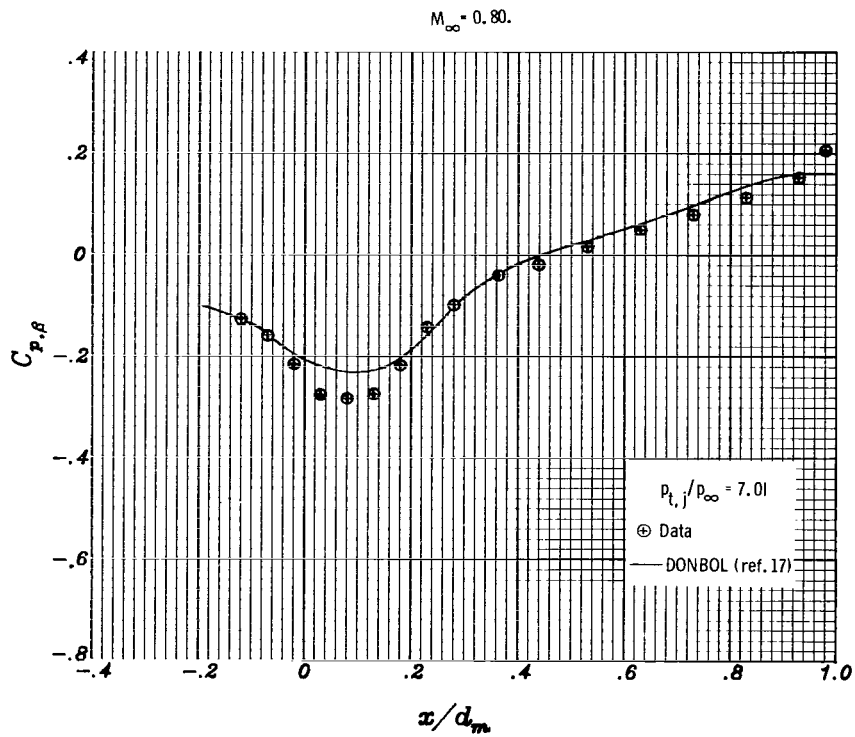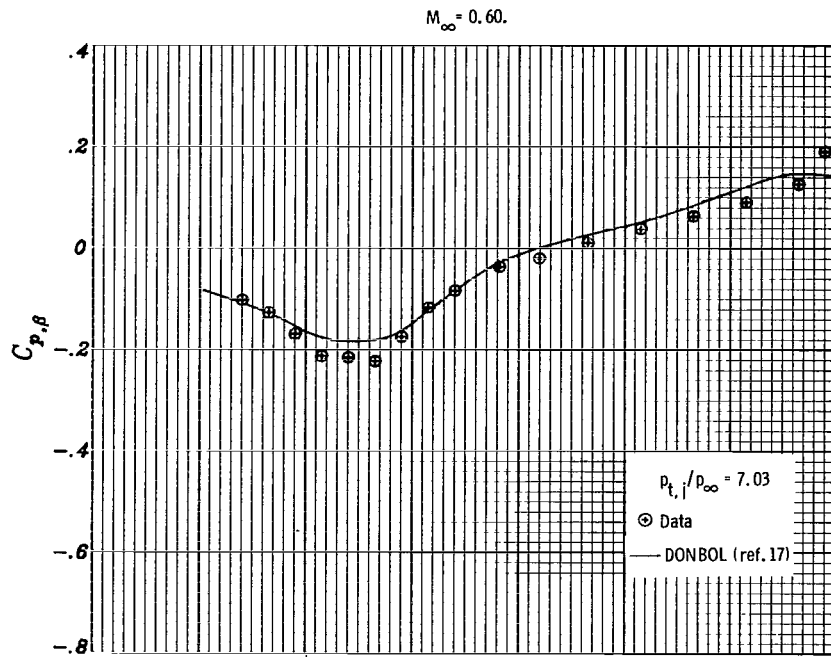
(a) M_∞ = 0.60 and 0.80.

Figure 22.- Comparison of experimentally and analytically
determined external pressure distributions for nozzle
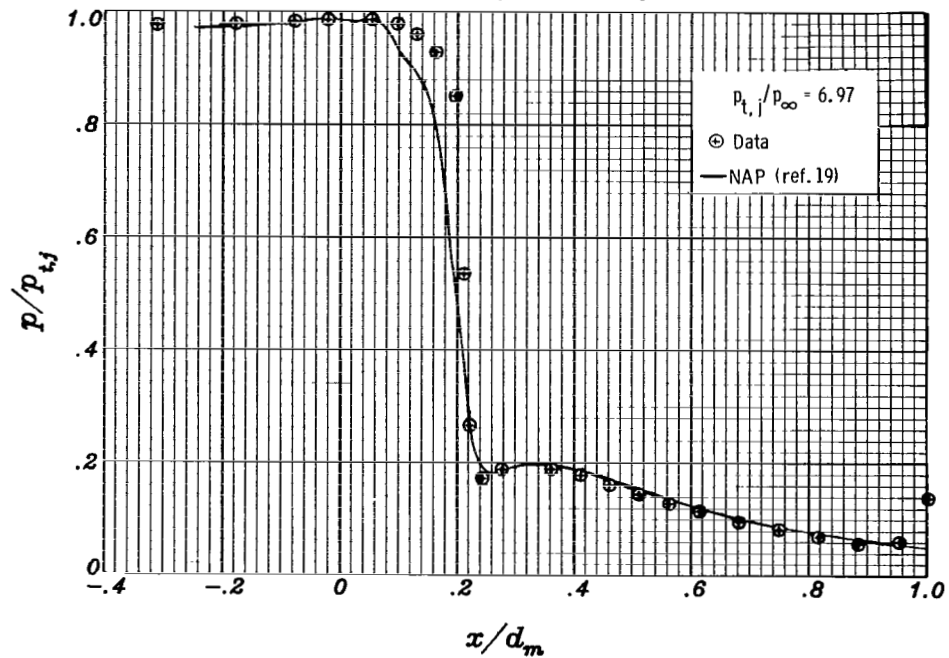configuration 4. Boattail angle is 8.28°; design nozzle
pressure ratio is 6.23.
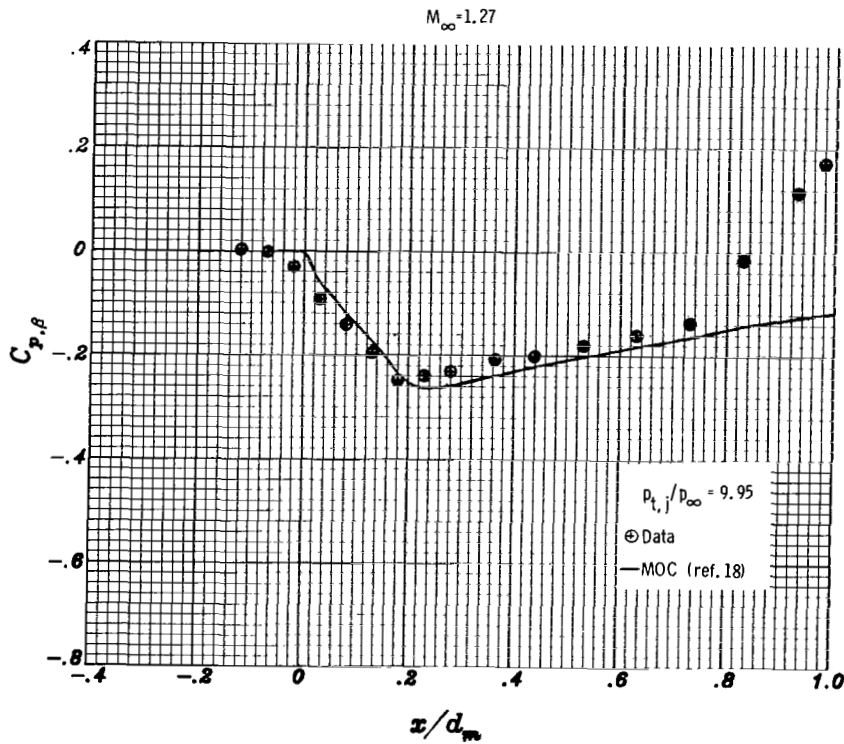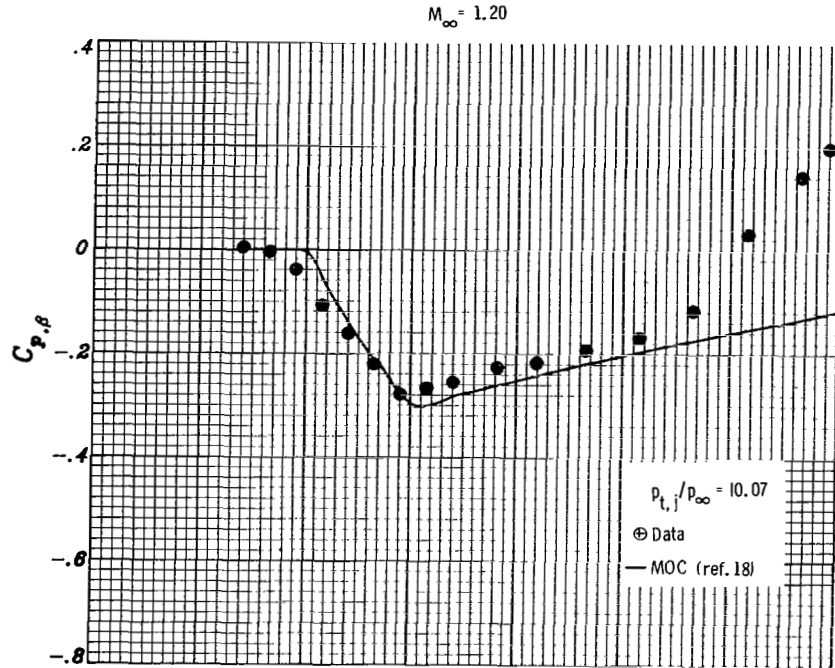
(b) M_∞ = 1.20 and 1.27.

Figure 22.- Concluded.

$M_\infty = 0.60$

$M_\infty = 0.80$

$p_{t,j}/p_\infty = 5.58$
⊕ Data
—— DONBOL (ref. 17)

$p_{t,j}/p_\infty = 6.41$
⊕ Data
—— DONBOL (ref. 17)

(a) $M_\infty = 0.60$ and 0.80.

Figure 23.- Comparison of experimentally and analytically
determined external pressure distributions for nozzle
configuration 5. Boattail angle is 2.12°; design nozzle
pressure ratio is 10.64.

$M_\infty = 1.20$

$p_{t,j}/p_\infty = 9.51$

Data

MOC (ref. 18)

$M_\infty = 1.27$

$p_{t,j}/p_\infty = 9.97$

Data

MOC (ref. 18)

(b) $M_\infty = 1.20$ and 1.27.

Figure 23.- Concluded.

Configuration I.   Design nozzle pressure ratio is 4.25.

$p_{t,j}/p_{\infty} = 7.03$

⊕ Data

— NAP (ref. 19)

Configuration 2. Design nozzle pressure ratio is 21.23.

$p_{t,j}/p_{\infty} = 6.97$

⊕ Data

— NAP (ref. 19)

x/d_m

(a) Configurations 1 and 2.

Figure 24.- Comparison of experimentally and analytically
    determined internal pressure distributions at a free-stream
    Mach number of 0.60.

81

Configuration 3. Design nozzle pressure ratio is 5.03.
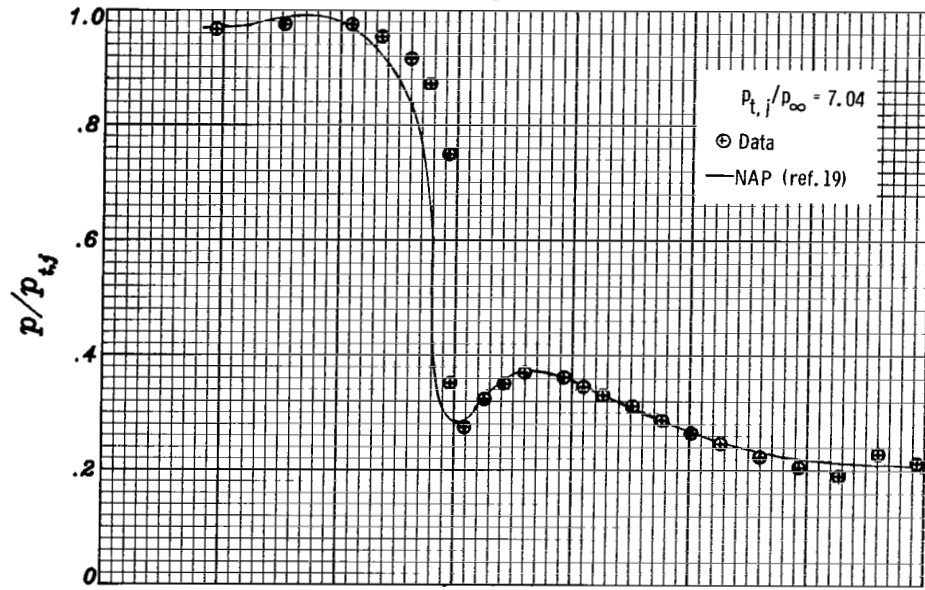
Configuration 4. Design nozzle pressure ratio is 6.23.
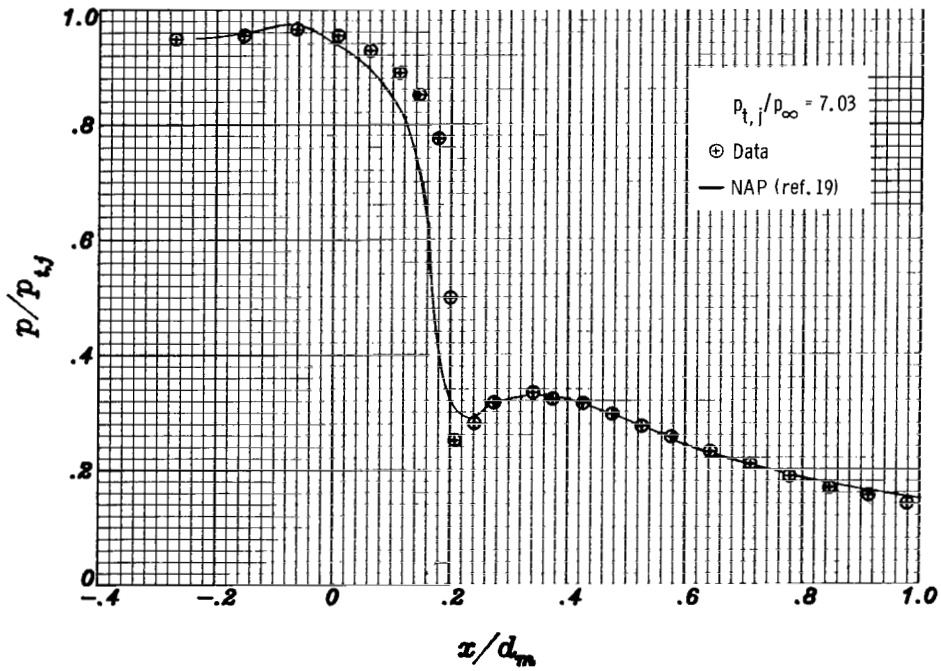
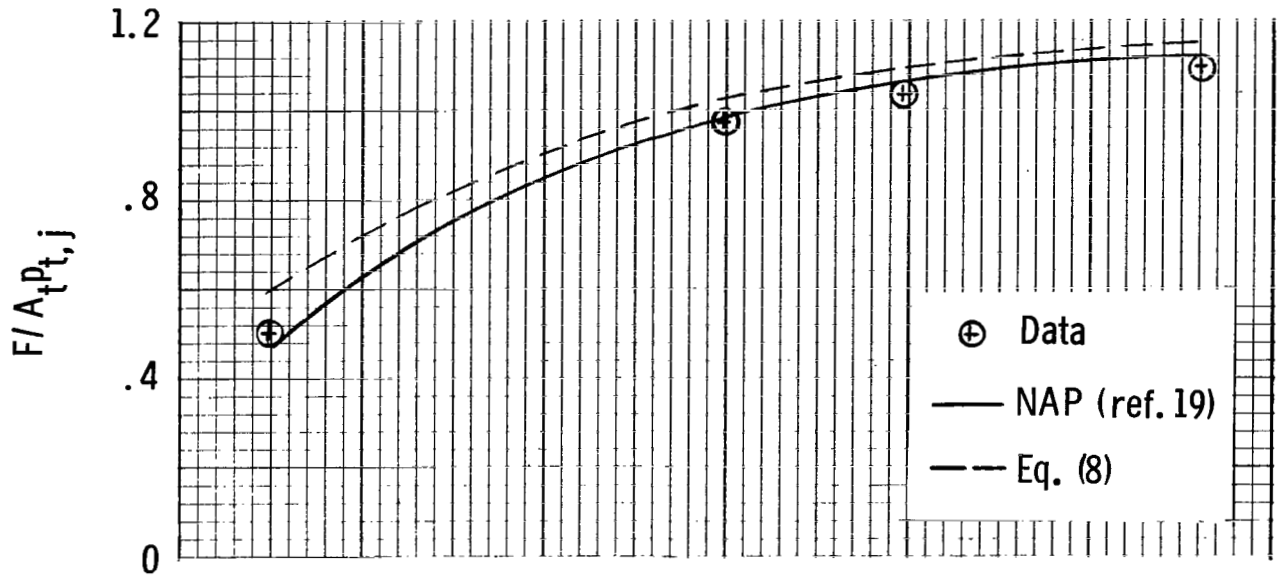(b) Configurations 3 and 4.

Figure 24.- Continued.

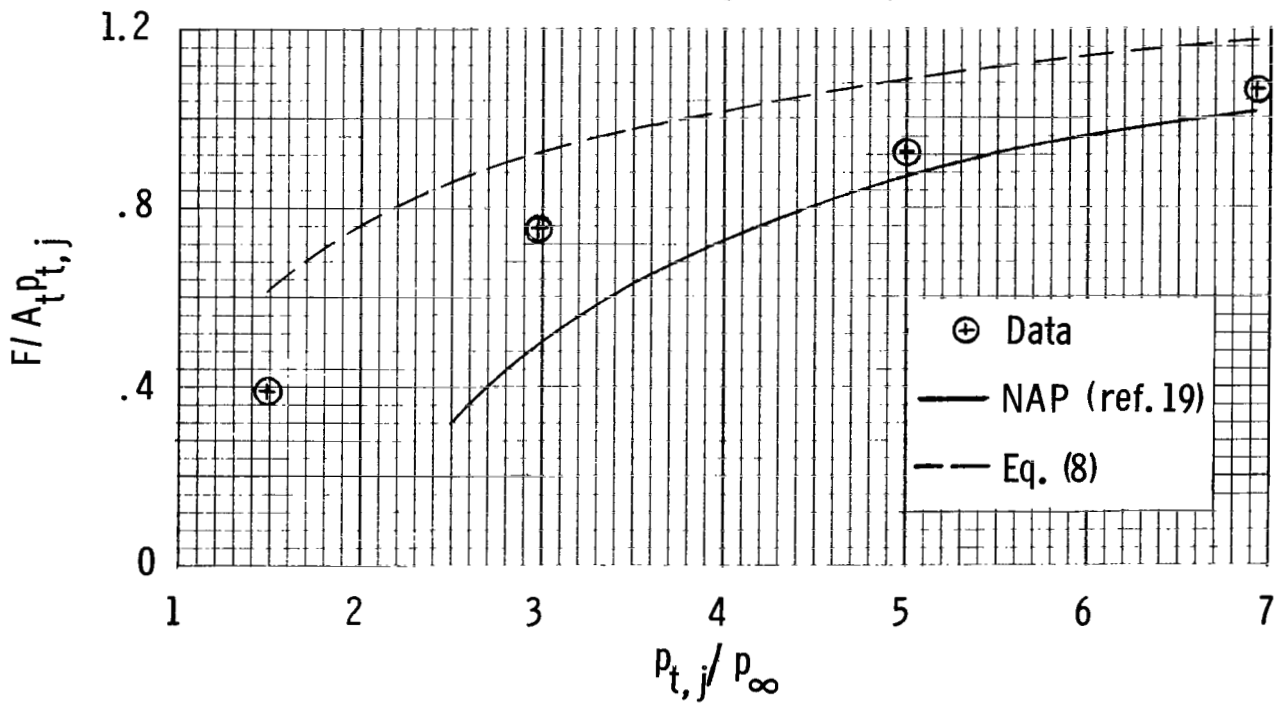Configuration 5. Design nozzle pressure ratio is 10.64.
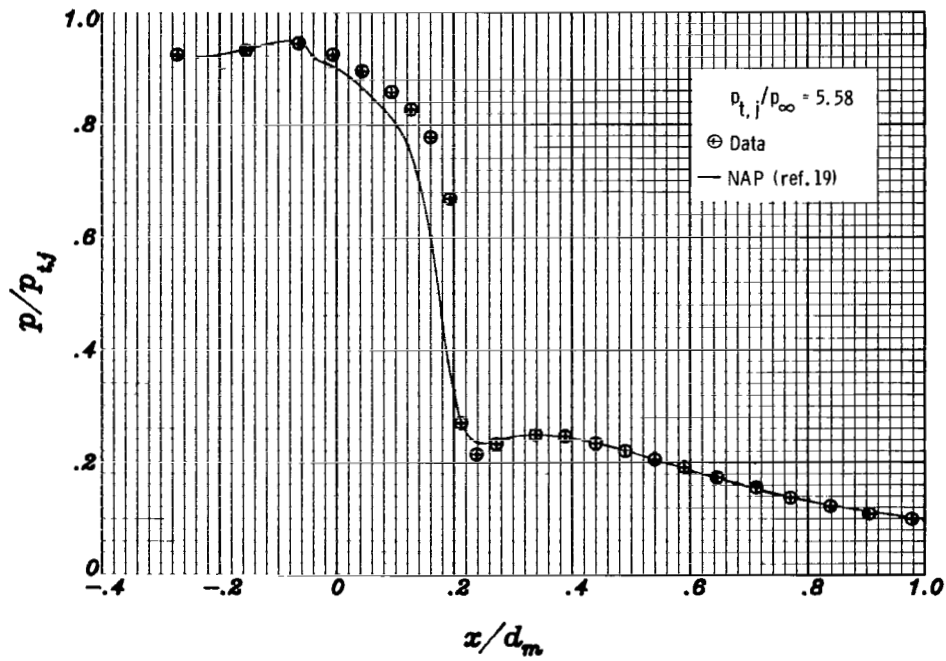
(c) Configuration 5.

Figure 24.- Concluded.

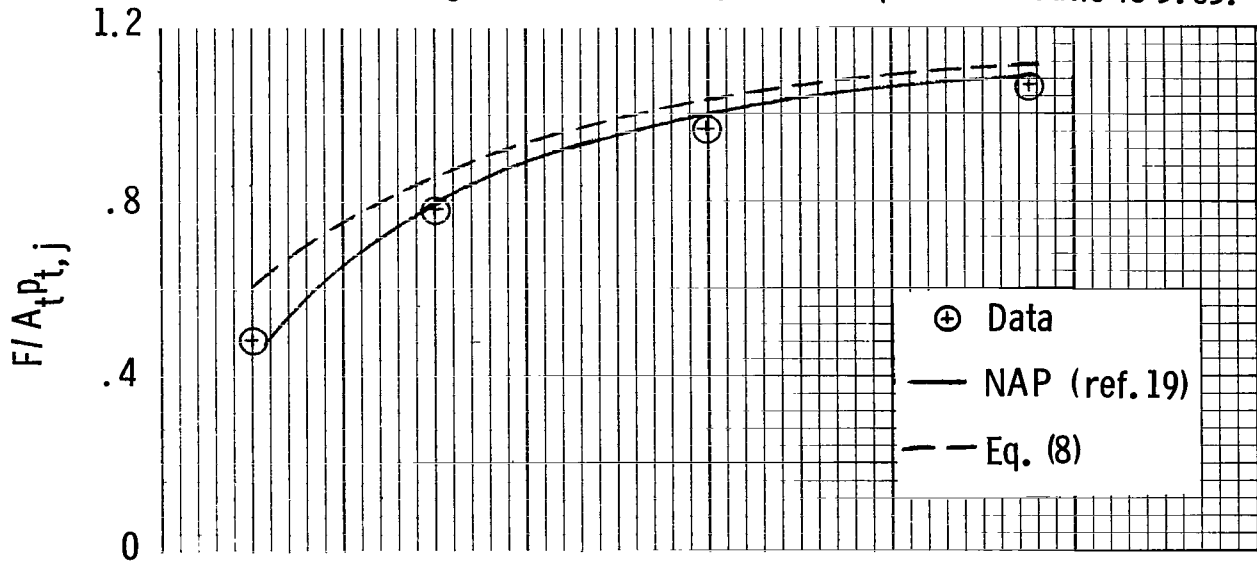**Configuration 1. Design nozzle pressure ratio is 4.25.**

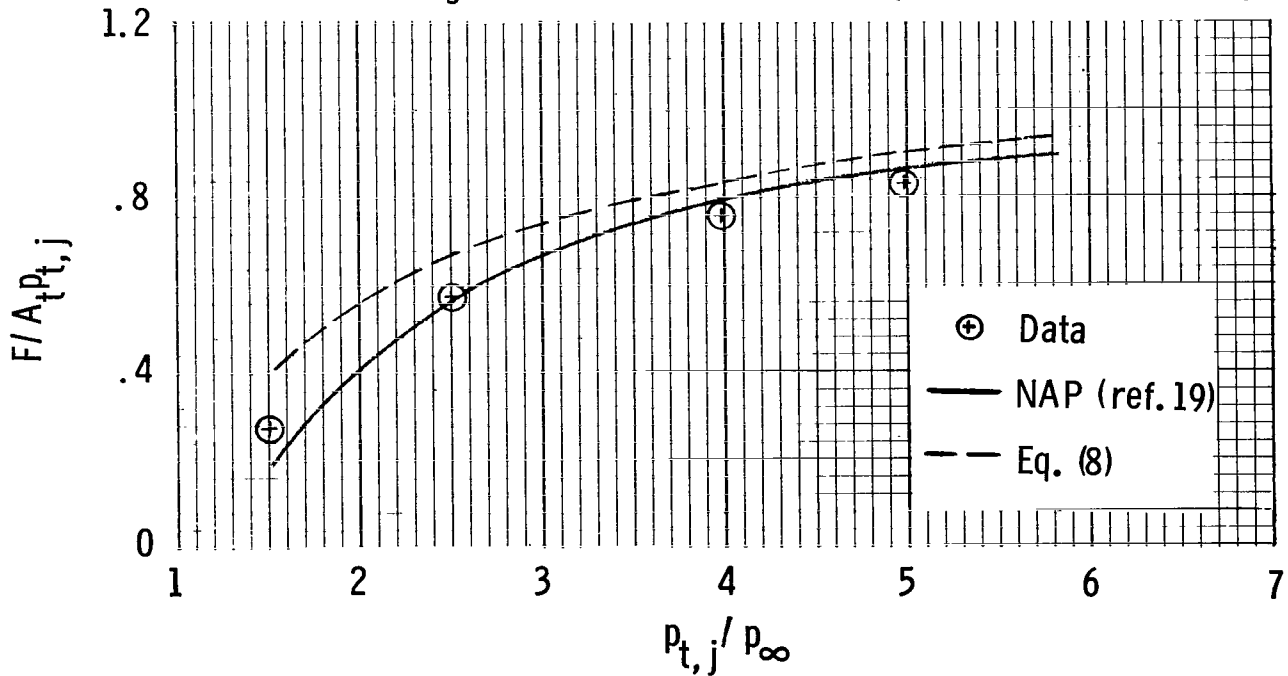**Configuration 2. Design nozzle pressure ratio is 21.23.**

(a) Configurations 1 and 2.

Figure 25.- Comparison of experimentally and analytically determined variation of static thrust coefficient with nozzle pressure ratio.

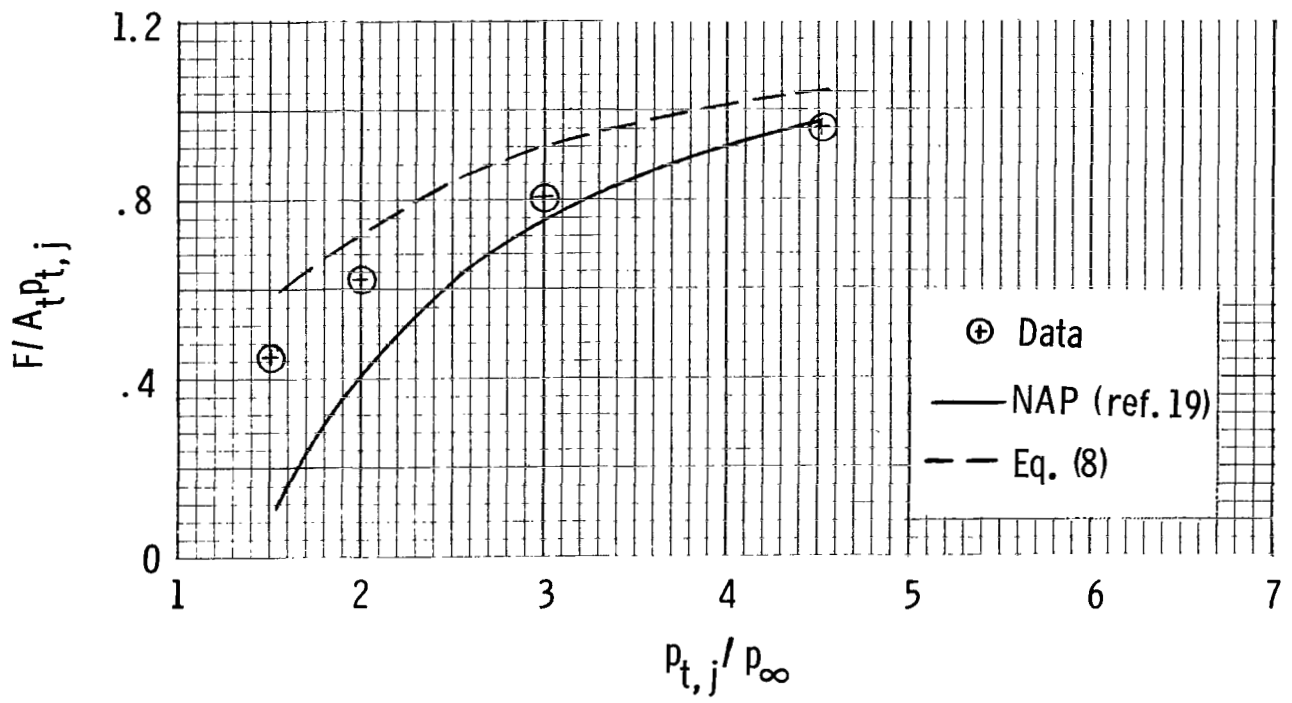Configuration 3. Design nozzle pressure ratio is 5.03.

Configuration 4. Design nozzle pressure ratio is 6.23.

(b) Configurations 3 and 4.

Figure 25.- Continued.

Configuration 5. Design nozzle pressure ratio is 10.64.

(c) Configuration 5.

Figure 25.- Concluded.

1. Report No. NASA TP-1953	2. Government Accession No.	3. Recipient's Catalog No.
4. Title and Subtitle EXPERIMENTAL AND ANALYTICAL INVESTIGATION OF AXISYMMETRIC SUPERSONIC CRUISE NOZZLE GEOMETRY AT MACH NUMBERS FROM 0.60 TO 1.30		5. Report Date December 1981
		6. Performing Organization Code 505-32-13-01
7. Author(s) George T. Carson, Jr., and Edwin E. Lee, Jr.		8. Performing Organization Report No. L-14661
		10. Work Unit No.
9. Performing Organization Name and Address NASA Langley Research Center Hampton, VA 23665		11. Contract or Grant No.
		13. Type of Report and Period Covered Technical Paper
12. Sponsoring Agency Name and Address National Aeronautics and Space Administration Washington, DC 20546		14. Sponsoring Agency Code

15. Supplementary Notes

16. Abstract

An experimental investigation has been conducted which provides quantitative pressure and force data for five axisymmetric boattail nozzle configurations. These configurations simulate the variable-geometry feature of a single nozzle design operating over a range of engine operating conditions. This investigation was performed in the Langley 16-Foot Transonic Tunnel at Mach numbers from 0.60 to 1.30. The experimental data were also compared with theoretical predictions.

17. Key Words (Suggested by Author(s)) Variable-geometry nozzle Variable-cycle engine Axisymmetric boattail nozzle Supersonic cruise aircraft	18. Distribution Statement Unclassified - Unlimited Subject Category 02
19. Security Classif. (of this report) Unclassified	20. Security Classif. (of this page) Unclassified	21. No. of Pages 87	22. Price A04

NASA